TISSUE OPTICS MODELING IN HIGH RESOLUTION MICROSCOPY

GONG WEI

NATIONAL UNIVERSITY OF SINGAPORE

2010

TISSUE OPTICS MODELING IN HIGH RESOLUTION MICROSCOPY

GONG WEI

A THESIS SUBMITTED

FOR THE DEGREE OF DOCTOR OF PHILOSIPHY

DIVISION OF BIOENGINEERING

NATIONAL UNIVERSITY OF SINGAPORE

2010

Acknowledgements

The work presented in this thesis was primarily conducted in Optical Bioimaging Laboratory in the Division of Bioengineering at National University of Singapore from August 2006 to August 2010. There are many people who have helped me during my study towards this thesis:

Special thanks go to my supervisor Prof. Colin J. R. Sheppard for his supervision and guidance throughout my postgraduate study. Without his invaluable suggestions and patient discussions, this thesis could not be completed. It is also Prof. Sheppard who made me understand that profound knowledge comes from precise attitude, rigorous style and hardworking. I believe and appreciate that Prof. Sheppard has an extraordinary impact on my future research career.

I greatly appreciate the generous support and guidance from Assistant Professor Chen Nanguang, who gave me a lot of useful discussion, especially on the experiments. Great appreciation and respect to Assistant Professor Huang Zhiwei and Prof. Hanry Yu and their group members, who taught me useful knowledge on optics and biology research.

I would like to thank for the enthusiastic discussions and suggestions given by my coworkers and team members: Waiteng, Shakil, Elijiah, Shanshan, Shalin and Naveen. I also would like to thank the support and understanding of all the other students and staff in Optical Bioimaging Laboratory, especially Dr. Zheng Wei, Teh Seng Knoon, Liu Linbo, Shao Xiaozhuo, Lu Fake, Mo Jianhua, Zhang Qiang, Chen Ling, and Lin Kan.

My special thanks also to my parents, it is their love that makes me become the happiest person in the world. Despite how hard the reverse and difficulty are, they always believe in me and offer me support and encouragement.

I am also willing to express my most special thanks to my husband Dr Si Ke for his support and understanding. Because I am walking with you hand in hand, my life is now full of sunshine and splendidness.

Last but not least, I would like to acknowledge the financial support from the Ministry of Education of Singapore for my research at NUS.

Table of Contents

Summary

The optical properties of tissue and cells are of key significance in optical biomedical technology, such as in optical imaging and spectroscopy. In this thesis, scattering by randomly shaped particles has been investigated, to understand better optical properties of biological tissue and cell suspensions. After proposing generation functions for the randomly shaped particles, the *T*-matrix method and appropriate effective size distribution were applied to rigorously compute phase functions, depending on the physical and geometrical characteristics of the scatterers. The derived phase functions show good agreement with experimental results. To obtain the high quality optical imaging, advanced microscopy with high resolution, high optical sectioning ability and deep penetration depth is required. In this thesis, we analyzed the confocal microscopy with divided apertures with diffraction theory. In addition, the optimization of axial resolution with respect to the width of the divider between the two divided apertures was presented. To suppress the out-of-focus central bright spot in the confocal microscopy with divided apertures, an improvement with serrated divided apertures was reported. The results show an increasing efficiency of the rejection of scattered light. Diffraction analysis also shows that the serrated apertures maintain the optical sectioning strength while attenuating the background coming from far from the focal plane. In addition, the signal to background ratio is also improved. Finally, the focal modulation microscopy (FMM) was introduced to increase the imaging depth into tissue and rejection of background from a thick scattering object. FMM can simultaneously acquire conventional confocal images and FMM images. The application to saturable fluorescence was also discussed. The study on edge enhancement for FMM shows that compared with confocal microscopy, using FMM can result in a sharper image of the edge and the edge gradient can be increased up to 75.4% and 58.9% for thick edge and thin edge, respectively. A further improvement with FMM using annular apertures (AFMM) was also reported. Compared with confocal microscopy, AFMM can simultaneously enhance the axial and transverse resolution. By adjusting the width of the annular objective aperture, AFMM can be adjusted from best spatial resolution performance to highest signal level. In addition, AFMM has the potential to further increase the imaging penetration depth. This research indicates the great potential of FMM in biological and biomedical systems.

List of Publications

Journal papers

1. W. Gong, K. Si, X. Q. Ye, and W. K. Gu, “A highly robust real-time image enhancement,” Chinese Journal of Sensors and Actuators, **9**, 58-62 (2007)
2. W. Gong, K. Si, and C. J. R. Sheppard, “Light scattering by random non-spherical particles with rough surface in biological tissue and cells,” J. Biomechanical Science and Engineering, **2**, S171 (2007)
3. K. Si, W. Gong, C. C. Kong, and T. S. Hin, “Visualization of bone material map with novel material sensitive transfer functions,” J. Biomechanical Science and Engineering, **2**, S211 (2007)
4. W. Gong, K. Si, and C. J. R. Sheppard. “Modeling phase functions in biological tissue**,”** Opt. Lett. **33**, 1599-1601. (2008)
5. C. J. R. Sheppard, W. Gong, and K. Si, “The divided aperture technique for microscopy through scattering media,” Opt. Express, **16**, 17031–17038 (2008)
6. K. Si, W. Gong, and C. J. R. Sheppard, “ Three-dimensional coherent transfer function for a confocal microscope with two D-shaped pupils,” Appl. Opt. **48**, 810-817 (2009)
7. K. Si, W. Gong, and C. J. R. Sheppard, "Model for light scattering in biological tissue and cells based on random rough nonspherical particles", Appl. Opt. **48**, 1153-1157 (2009).
8. W. Gong, K. Si, and C. J. R. Sheppard, “Optimization of axial resolution in confocal microscope with D-shaped apertures,” Appl. Opt. **48**, 3998-4002 (2009).
9. W. Gong, K. Si, and C. J. R. Sheppard, “Improvements in confocal microscopy imaging using serrated divided apertures,” Opt. Commun. **282**, 3846-3849 (2009).
10. K. Si, W. Gong, N. Chen, and C. J. R. Sheppard, “Edge enhancement for in-phase focal modulation microscope”, Appl. Opt. **48**, 6290-6295 (2009).
11. W. Gong, K. Si, N. Chen, and C. J. R. Sheppard, “Improved spatial resolution in fluorescence focal modulation microscopy”, Opt. Lett. **34**, 3508-3510 (2009).
12. W. Gong, K. Si, and C. J. R. Sheppard, “Divided-aperture technique for fluorescence confocal microscopy through scattering media,” Appl. Opt. **49**, 752-757 (2010).
13. W. Gong, K. Si, N. Chen, and C. J. R. Sheppard, “Focal modulation microscopy with annular apertures: A numerical study,” J. Biophoton. **3**, 476-484 (2010).
14. C. J. R. Sheppard, W. Gong, and K. Si, “Polarization effects in 4Pi Microscopy,” Micron, doi:10.1016/j.micron.2010.07.013 (2010).

15. K. Si, W. Gong, N. Chen, and C. J. R. Sheppard, "Enhanced background rejection in thick tissue using focal modulation microscopy with quadrant apertures," Opt. Commun. **284**, 1475-1480 (2011).
16. K. Si, W. Gong, and C. J. R. Sheppard, "Penetration depth in two-photon focal modulation microscopy," Opt. Lett., (submitted).

Conference presentations

1. W. Gong, K. Si, and C. J. R. Sheppard, "Light Scattering by Random Non-spherical Particles with Rough Surfaces in Biological Tissue and Cells," The 4th Scientific Meeting of the Biomedical Engineering Society of Singapore (2007).
2. K. Si, W. Gong, C. C. Kong, and T. S. Hin, "Application of Novel Material Sensitive Transfer Function in Characterizing Bone Material Properties," The 4th Scientific Meeting of the Biomedical Engineering Society of Singapore (2007).
3. W. Gong, K. Si, and C. J. R. Sheppard, "Light Scattering by Random Non-spherical Particles with Rough Surface in Biological Tissue and Cells," Third Asian Pacific Conference on Biomechanics, (2007)
4. K. Si, W. Gong, C. C. Kong, and T. S. Hin, "Visualization of Bone Material with Novel Material Sensitive Transfer Functions," Third Asian Pacific Conference on Biomechanics, (2007).
5. K. Si, W. Gong, and C. J. R. Sheppard, "3D Fractal Model for Scattering in Biological Tissue and Cells," 5th International Symposium on Nanomanufacturing, (2008)
6. K. Si, W. Gong, and C. J. R. Sheppard, "Application of Random Rough Nonspherical Particles Mode in Light Scattering in Biological Cells," GPBE/NUS-TOHOKU Graduate Student Conference in Bioengineering, (2008).
7. K. Si, W. Gong, and C. J. R. Sheppard, "Fractal Characterization of Biological Tissue with Structure Function", the Seventh Asian-Pacific Conference on Medical and Biological Engineering (APCMBE 2008)
8. K. Si, W. Gong, and C. J. R. Sheppard, "Modulation Confocal Microscope with Large Penetration Depth", SPIE Photonics West, (2009).
9. K. Si, W. Gong, and C. J. R. Sheppard, "Better Background Rejection in Focal Modulation Microscopy", OSA Frontiers in Optics (FiO)/Laser Science XXV (LS) Conference, (2009)
10. K. Si, W. Gong, N. Chen, and C. J. R. Sheppard, "Focal Modulation Microscopy with Annular Apertures," 2nd NGS Student symposium, (2010).
11. W. Gong, K. Si, N. Chen, and C. J. R. Sheppard, "Two photon focal modulation microscopy," Focus on Microscopy, (2010).

12. K. Si, W. Gong, N. Chen, and C. J. R. Sheppard, “Annular pupil focal modulation microscopy,” Focus on Microscopy, (2010).
13. W. Gong, K. Si, N. Chen, and C. J. R. Sheppard, “Two-photon microscopy with simultaneous standard and enhanced imaging performance using focal modulation technique,” SPIE Photonics Europe, (2010).
14. K. Si, W. Gong, N. Chen, and C. J. R. Sheppard, “Imaging Formation of Scattering Media by Focal Modulation Microscopy with Annular Apertures,” SPIE Photonics Europe, (2010).

List of Tables

List of Figures

List of Abbreviations

3D	=	Three-dimensional
AFMM	=	FMM with annular apertures
APSF	=	Amplitude point spread functions
CM	=	Confocal microscopy
CP	=	Display window
CTF	=	Coherent transfer function
DCM	=	Confocal microscopy with divided D-shaped apertures
DFMM	=	FMM with divided D-shaped apertures
D/L	=	Diameter-to-length ratio
FMM	=	Focal modulation microscopy
FOCSM	=	Fiber optic confocal scanning microscope
HWHM	=	Half-widths at half-maximum
IPFMM	=	In-phase focal modulation microscopy
IPSF	=	Intensity point spread function
MPM	=	Multi-photon microscopy
NA	=	Numerical aperture
OCT	=	Optical coherence tomography
OPFOS	=	Orthogonal-plane fluorescence optical sectioning
OTF	=	Optical transfer function
PSF	=	Point spread function
SAX	=	Saturated excitation microscopy
S/B	=	Signal to background ratio
SPIM	=	Selected plane illumination microscopy

Chapter 1 Introduction

1. 1 Background

Noninvasive visualization of structures, microenvironments and drug responses at cellular and sub-cellular level are of importance in biological research [1-3]. Optical microscopy is one of the techniques for noninvasive visualization and is an icon of the sciences because of its history, versatility and universality. Modern optical microscopy such as confocal microscopy, multiphoton microscopy and optical coherence microscopy provides subcellular resolution imaging in biological systems. Among these techniques, confocal microscopy, with submicron spatial resolution and optical sectioning property, has become a well-established tool in various fields of biological research and medical diagnoses [4-5]. However, it is also well accepted that confocal microscopy suffers from a limited imaging depth penetration in thick tissue due to multiple scattering [6]. To maintain a near-diffraction-limited resolution in a deep region of the sample, it is essential to develop a mechanism effectively to reject the scattered light. Preliminary studies have included the substitution of the circular aperture by an annular aperture. When combined with a finite-sized detector the axial resolution is improved [7]. Another promising technique is based on angular gating, in which the illumination and collection beams are separated by either divided apertures

(also called D-shaped apertures) [8-13] or a dual-axes configuration [14-15]. Only the light scattered in the focal region can be detected; the light scattered outside the focal region and multiply-scattered light cannot pass through both the collection pupil and confocal pinhole. More recently, a modified confocal microscopy technique called focal modulation microscopy (FMM) [16], was developed to effectively reject the multiply scattered photons.

The optical imaging properties do not only affect the performance of microscopy and spectroscopy in medicine, but also allow the measurement of the elastic scattering properties of biological tissue and cells to detect underlying pathology [17-18]. Although it is recognized that the optical properties of tissue and cells are related to its microstructure and refractive index, the nature of the relationship is still poorly understood. Previous investigations have focused on various aspects of this relationship, including the contribution of mitochondria to the scattering properties of the living organism [19], the spatial variations in the refractive index of cells and tissue sections [20], and the diffraction properties of single cells [21]. Still lacking, however, is a quantitative model that is related to the microscopic properties of cells and other tissue elements to the scattering coefficients of bulk tissue. Ideally, such a model should be able to predict the absolute magnitudes of the optical scattering coefficients as well as their wavelength and angle dependencies. Therefore, a discrete particle model with random non-spherical particles with rough surface has been proposed to satisfy at least a few of these

requirements. Tissue optics is also useful in predicting the performance of different microscopy techniques in imaging through a scattering medium.

The subsequent sections provide an overview of different models in tissue optics and high resolution microscopy.

1. 2 Challenges in tissue optics modeling

Propagation of light in a turbid medium can be described by the radiative transport theory [22]. The resulting Boltzmann transport equation gives the radiance in terms of the absorption coefficient μ_a, the scattering coefficient μ_s, the extinction coefficient $\mu_t = \mu_s + \mu_a$, and the phase function (scattering function) $P(\theta)$, (the normalized angular distribution of scattering). The albedo is defined as $W_0 = \mu_s / \mu_t$. When absorption is small compared with scattering ($W_0 \approx 1$), and scattering is not very anisotropic, the transport equation reduces to the diffusion equation [23]. The diffusion coefficient is $D = \{3[\mu_a + (1-g)\mu_s]\}^{-1}$, where g is the anisotropy factor, the mean cosine of the phase function. The transport coefficient is $\mu_{tr} = \mu_a + (1-g)\mu_s$, and the diffusion length is $L = \sqrt{D/\mu_a}$.

Another approach for modeling propagation through a turbid medium is based on a discrete particle model. In the discrete particle model, researchers identify the major elements in soft tissue responsible for the microscopic variations in its refractive index and, to facilitate numerical

computations, treat the variations as discrete particles with statistically equivalent refractive index [24-25]. Scattering of light by spherical objects is described by Mie theory, which was developed as an analytical solution of Maxwell's equations for the scattering of electromagnetic radiation [26-28]. However, this approach is based on the assumption that the medium is homogeneous and isotropic, and the scattering particles are spheres. Moreover, the surfaces of the scatterers are assumed smooth. Unfortunately, these assumptions are far from real [29]. The scattering properties, which are seriously affected by the shape, size and components of the scatterers, of nonspherical particles can differ dramatically from those of "equivalent" spheres. Therefore, the ability to accurately measure or model light scattering by nonspherical particles in order to clearly understand the effects of particle nonsphericity on scattering pattern is very practical and significant.

To develop a better optics model for scattering by non-spherical particles, some researchers have conducted field studies and experiments based on various methods. Waterman introduced the *T*-matrix method as a technique for computing electromagnetic scattering by single, homogeneous, arbitrarily shaped particles based on Huygens' principle [30]. After ten years of development, the *T*-matrix approach has become one of the most powerful and widely used tools for rigorously computing electromagnetic scattering by single and compounded particles. In many applications it surpasses other frequently used techniques in terms of efficiency and size parameter range and

is the only method that has been used in systematic surveys of nonspherical scattering based on calculations for thousands of particles in random orientation [31]. Recently, Mishchenko applied the *T*-matrix method to multiple scattering by random distributed dust-like aerosols in aerospace [32]. However, there is still a lack of such rigorous computed model for biological science and medical diagnosis. Therefore, it is highly imperative to develop a comprehensive discrete model based on *T*-matrix method, which is suitable for biological tissue and cells.

1. 3 Challenges in high resolution microscopy

1.3.1 Angular gating technique

Confocal microscopy (CM) has wide applications in biological research and medical diagnosis, as a consequence of its ability to exclude out-of-focus information from the image data, thus improving the fidelity of focal sectioning and increasing the contrast of fine image details. The optical sectioning ability of confocal microscopy results from the pinhole before the detector, used to reject out-of-focus light scattered by the tissue. However, when the focal point moves deep into tissue, the selective mechanism of the pinhole is not sufficiently effective to suppress the out-of-focus light since the multiple scattering becomes to dominate. One of the methods to enhance the background rejection utilizes an angular gating mechanism, in which the

illumination and detection beams overlap only in the focal region, thus resulting in angular gating and improving the optical sectioning and rejection of scattered light.

Angular gating had its beginning with the ultramicroscope, in which the sample is illuminated perpendicular to the imaging optical axis [33]. The specular microscope, or divided aperture technique, combines different beam paths for illumination and detection with confocal imaging, so that light scattered other than in the focal region is rejected [8-9, 34-35]. The ultramicroscope was also the fore-runner of confocal theta microscopy [36-37], laser scattering tomography [38-39] and orthogonal-plane fluorescence optical sectioning (OPFOS) [40], also known as selected plane illumination microscopy (SPIM) [41], both of which are usually implemented in a fluorescence mode. All these techniques have in common that the illuminating and detection pupils do not overlap, so that the illumination and detection beams overlap only in the focal region.

Koester also compared theoretically the optical sectioning performance of his system with that of a confocal system with a circular detector aperture, based on geometrical optics [8-9]. Other applications based on the D-shaped pupils were given by Török *et al* [42-43]. They modified a commercial confocal microscope with a D-shaped aperture stop to realize dark-field imaging. Although their system also employed the D-shaped aperture, it was fundamentally different with Koester's bright-field confocal microscope. They

derived the one-dimensional transfer function in the direction perpendicular to the edge of the beam-stop, and later on they extended their study to the dark-field and differential phase contrast imaging with two D-shaped pupils. More recently, Dwyer *et al.* have used a similar system to investigate *in vivo* human skin [10-11]. They called their system the confocal reflectance theta line-scanning microscope, to stress that their system combines confocal line-scanning with off-axis geometry, but actually their system is very similar to that of Koester [8]. In the analysis of Dwyer *et al*., they derived the lateral resolution and sectioning strength based on two equivalent offset non-overlapping circular pupils, as an approximation to the two D-shaped pupils. Therefore, it is of practical significance to investigate the optical properties of confocal microscope with two D-shaped pupils based on diffraction optics.

1.3.2 Focal modulation microscopy

When the focal point moves deep into the tissue, the point spread function of confocal microscopy broadens dramatically because of the effect of multi-scattering, which significantly degrades the spatial resolution [6]. In order to remain high resolution in deep region of the tissue, numerous techniques have emerged recently. Multi-photon microscopy (MPM) utilizes an ultra-short-pulsed laser to further concentrate the illumination spot. By employing such nonlinear processes as two-photon excited fluorescence or

second-harmonic generation, MPM can obtain high resolution image when the imaging depth is less than 1 mm [6, 44]. However, MPM is an expensive technique, and its applications are limited by its complex probes. Optical coherence tomography (OCT) is another approach to get an imaging depth up to 3 mm by utilizing coherent gating [45]. However, the technique is not compatible with fluorescence.

Another promising technique, saturated excitation microscopy, utilizes the saturation phenomenon to achieve spatial resolution beyond the diffraction limit, since this technique imposes strong nonlinearity in the relation between excitation rate and fluorescence emission [46-47]. However, this technique require strong excitation intensity, which may exhibit not only photobleaching but also other undesirable effects in observation of living biological samples, such as defunctionalization of proteins by a large temperature rise. Therefore, it is of high significance to develop a comprehensive microscope technique, which not only maintains the optical sectioning ability, but also obtains a deep penetration depth as well.

1. 4 Objectives and Significance of the research

In view of the above review, there is an urgent need for a tissue optics model in biological science and medical diagnosis. Since it is nearly impossible to take into account all the factors when calculating optical feature

parameters directly based on Maxwell's equations, different models and approximations have been proposed. The imaging quality in high resolution microscopy is also of key importance for biological science and biomedical diagnosis. The justifications for the current study on tissue optics modeling in high resolution microscopy are summarized below:

- The previous studies are based on the assumption that the medium is homogeneous and isotropic, and the scattering particles are spheres, for the sake of calculation simplicity. However, as we all know, the tissue and cells in living organisms are various in shapes, sizes and directional sensitivity.
- The discrete particle model obtains results based on spherical particles with smooth surface, which is not applicable in many cases. Besides, the study on biological science only considers the single scattering case, while multiple scattering is unavoidable, especially for thick tissue.
- The previous analysis given by C. J. Koester [8-9] and P. J. Dwyer [10-11] on confocal microscopy with divided apertures is based on geometrical optics or various approximations, which deviates much with the experimental results.
- The selective detection mechanism is not so effective when the focal point moves deep into the tissue, where multiple scattering dominates over ballistic scattering.

The main aim of this study was to propose a tissue optics model which is applicable to biological science and medical diagnosis, and develop a high resolution microscopy which has a deep penetration depth, as well as high resolution. The specific objectives of this research were to:

- Propose a comprehensive discrete model based on *T*-matrix method, which is suitable for biological science.
- Study the scattering effects on the nonspherical shapes, different sizes and random distributions of the biological tissue and cells.
- Analyze the confocal microscopy with divided apertures based on diffraction optics.
- Develop and analyze focal modulation microscopy, which can increase imaging depth into tissue and rejection of background from a thick scattering object.

The interaction of light with tissue and cells is the underlying mechanism for optical biomedical technology used in optical imaging and spectroscopy for detection of pathologic changes. The optical properties of tissue are determined by chromophores, microstructures, and local refractive index variations. Any unrealistic assumptions may make the theoretical results deviating from the practical results dramatically. Therefore, the results of this present study, which break the conventional assumptions may have significant impact on precise tissue features representation, thus might be helpful and auxiliary in:

- medical diagnosis to make a better analysis of the patients data
- surgical guidance operation, which provides the intraoperative data reflecting the tissue changes during surgery and providing optimum feedback for surgical guidance .

This thesis provides tissue optics modeling in high resolution microscopy. In terms of experimental work, the theoretical results are examined with rat embryo fibroblast cell, mitochondria and mouse skeletal tissue. Therefore, the test modeling is restricted to biological tissue and cells. For other applications, for example, seafloor morphology, more experiments should be carried out to examine the validity. For the study of high resolution microscopy, the study is based on the assumption of paraxial approximation and single scattering. Therefore, for the case of high numerical aperture and multiple scattering dominating, more parameters should be considered.

1. 5 Structure of the thesis

This thesis studies the light scattering properties in biological tissue and cells and imaging formation in advanced high resolution microscopy. Chapter 2 investigates the light scattering mechanism by random non-spherical particles with rough surface. The phase function, which is an important quantity to describe the angular distribution of the scattered intensity, is estimated. In Chapter 3, the imaging formation in confocal

microscopy using divided apertures is presented. The coherent transfer function (CTF) is calculated in coherent confocal microscopy with divided apertures. Secondly, a diffraction analysis for coherent imaging and for incoherent imaging in confocal microscopy using divided apertures is provided. In addition, the optimization of axial resolution is investigated. Finally, the improvements with the use of serrated divided apertures are reported. Chapter 4 introduces focal modulation microscopy (FMM). Image formation and edge enhancement in FMM are described. Further improvements with annular apertures in FMM are also presented. Finally, conclusions and future directions are summarized in Chapter 5.

Chapter 2 Modeling optical properties in biological tissue

2.1 Random non-spherical particle model

2.1.1 Introduction

A growing number of applications in optical biomedical technology, such as optical imaging and spectroscopy, rely on the measurement of scattering properties of tissue and cells. Preliminary studies suggest that optical properties of tissue and cells depend on its microstructure and refractive index. Several approaches [48-49] have been proposed based on the assumption that the biological tissue and cells are homogeneous and isotropic. Usually, the scattering particles are assumed as spheres with smooth surfaces, because a suitable model or theoretical formulation has yet to be made for random particles. However, microstructure in biological tissue and cells can consist of different types of particles having arbitrary shapes, size distributions (ranging from organelles 0.2-0.5μm to nuclei 3–10μm in diameter) [50], and orientations, as well as an overall mass density that varies spatially within them. Optical properties of particles strongly depend on their shapes, so to create an appropriate model for light scattering by biological tissue and cells is important not only for theoretical interest but also for practical reasons. All previous studies of non-spherical scatterers have been based on solving

Maxwell's equations either analytically or numerically. For particles with axial symmetry, the *T*-matrix method [31, 51] can be implemented for computing rigorously electromagnetic scattering by single and compound particles. Mishchenko has applied the T-matrix method to multiple scattering by random distributed dust-like aerosols [32].

2.1.2 Generation functions for random non-spherical particles

To describe the light scattering by biological tissue, we model tissue by random non-spherical rough-surfaced particles with axially-symmetric properties instead of spherical scatterers. Assume that the random variables $X = (x_1, x_2, ..., x_N)^T$ corresponding to given spherical coordinates $S = (\alpha, \beta_1; \alpha, \beta_2; ...; \alpha, \beta_N)^T$ obey the normal distribution n_N with mean $\overline{x}$ and covariance matrix Σ_x:

$$n_N\left(x, \Sigma_x\right) = \frac{1}{\left(\sqrt{2\pi}\right)^N \sqrt{\det \Sigma_x}} \exp\left[-\frac{(X-\overline{x})^T \Sigma_x^{-1} (X-\overline{x})}{2}\right], \qquad (2.1.1)$$

where $\alpha = (\alpha_1, \alpha_2, ...\alpha_M)^T$ is the azimuth vector and $\beta = (\beta_1, \beta_2, ...\beta_N)^T$ is the elevation vector. The covariance matrix elements are:

$$\Sigma_{x,ij} = \sigma^2 C_x(d_{ij}), \quad i, j = 1, 2, \ldots, N, \qquad (2.1.2)$$

where σ^2 is the variance, C_x is the autocorrelation function, and d_{ij} is the angular distance between the direction *i* and *j*. If $x_1, x_2, \ldots, x_N$ are independent with identical distributions, we can simplify Eq. (2.1.1) to:

$$n_N\left[x(\alpha,\beta_k)\right]=\frac{1}{\sqrt{2\pi}\sigma_1}\exp\left[-\frac{(x-\overline{x})^2}{2{\sigma_1}^2}\right],\quad k=1,2,\ldots,N. \qquad (2.1.3)$$

$$\sqrt{\quad}$$

The random vector $\gamma=(\gamma_1,\gamma_2,...,\gamma_N)^T$ relates to the elevation vector $\beta=(\beta_1,\beta_2,...\beta_N)^T$ through:

$$\gamma=2ba^{(K-1)/2}\left[z(\beta)^{K-2}\right]\exp\left[-Kz(\beta)\right]^2/2\sigma_2^2), \qquad (2.1.4)$$

where $a=K/2\sigma_2^2$, $b=1/\Gamma\left[(K-1)/2\right]$. K is the shape parameter, *z(β)* is the height of the random particles at a particular elevation and Γ is the Gamma Function. Eq. (2.1.4) is similar to the form of the probability density function of the standard deviation distribution. To control the height of the random particle, a "display window" is established to select the span $W=z(\beta_N)-z(\beta_1)$ of the γ:

$$W=\begin{cases}1, & z(\beta_1)<z(\beta)<z(\beta_N),\\ 0, & \text{otherwise.}\end{cases} \qquad (2.1.5)$$

The corresponding random radii $R=(r_{i1},r_{i2},...,r_{iN})^T$ can be calculated through:

$$r_{ij}=x_{ij}\gamma_{ij}W_{ij},\quad i=1,2,\ldots,M;\ j=1,2,\ldots,N. \qquad (2.1.6)$$

The five-parameter generation functions in Eqs. (2.1.3-2.1.6) can completely describe the random non-spherical shape. The coefficient *K*, in conjunction with σ_2 and the center point of the "display window" (denoted as "*CP*"), approximately determines the shape of the particles. Changing the value of *K*,

σ_2 and *CP*, a variety of random non-spherical particles can be obtained, including sub-spherical, cylindrical, conical and double-spherical particles. A small value of the roughness parameter σ_1 is selected to represent slightly rough surfaces. $\overline{r}/W$ is the aspect ratio of the maximum-to-minimum particle dimensions for a sphere or a cone, or the diameter-to-length ratio (*D*/*L*) for a cylinder. Fig. 2.1.1 illustrates four random non-spherical particles with weak axial symmetry.

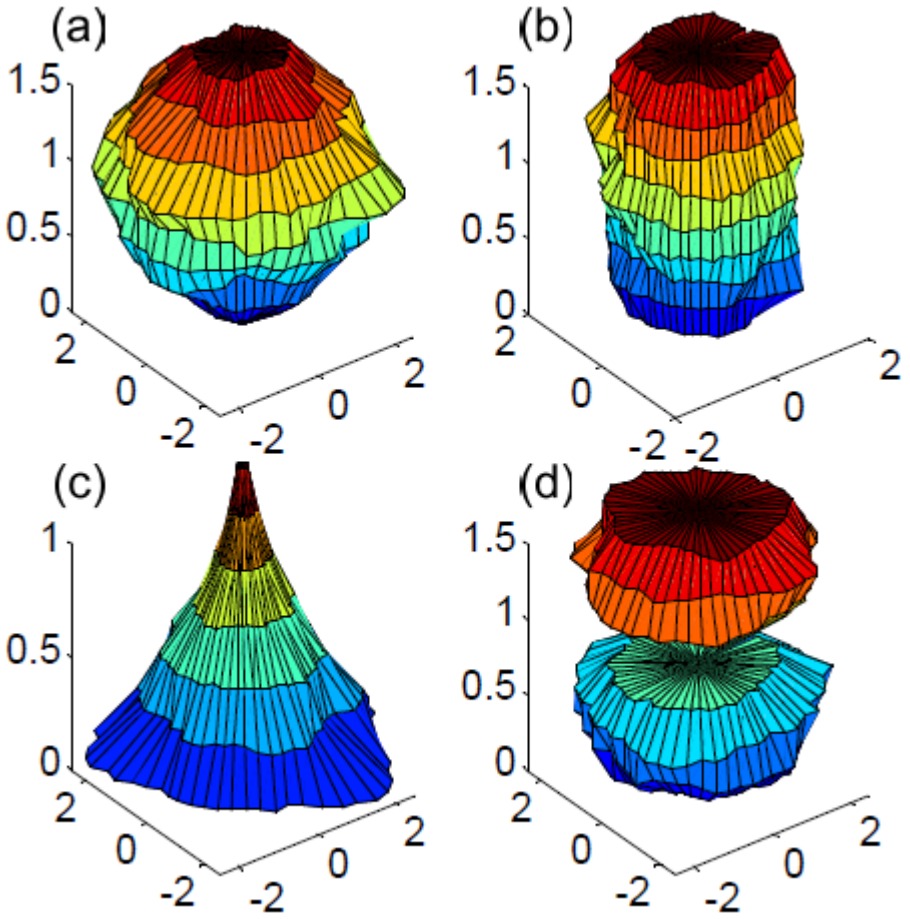

Fig. 2.1.1. 3D structure of the random non-spherical particles with respect to the mean value $\overline{r}=1$, roughness parameter σ_1=0.2, and the span of the window W=1. Different shapes can be obtained by changing the parameters *K*, σ_2 and the display window's center *CP*. (a): *K* = 2, σ_2 = 0.38, *CP* = -0.5; (b): *K* = 2,

σ_2 = 0.7, *CP* = -0.5; (c): *K* = 2, σ_2 = 0.38, *CP* = 0; (d): *K* = 3, σ_2 = 0.4, *CP* = -0.5.

2.1.3 Phase function

The basic quantities that fully describe the scattering process are the ensemble-averaged extinction C_{ext} and scattering C_{sca} cross-section and the elements of the so-called normalized Stokes scattering matrix $S(\theta)$ given by [31]:

$$S(\theta)=\begin{bmatrix} P(\theta) & b_1(\theta) & 0 & 0 \\ b_1(\theta) & a_2(\theta) & 0 & 0 \\ 0 & 0 & a_3(\theta) & b_2(\theta) \\ 0 & 0 & -b_2(\theta) & a_4(\theta) \end{bmatrix}. \tag{2.1.7}$$

Here, $\theta \in [0^\circ, 180^\circ]$ is the scattering angle. The well-known block-diagonal structure of this matrix is confirmed by the *T*-matrix results and is mainly caused by averaging over the uniform orientation distribution of a multi-particle group coupled with sufficient randomness of particle positions. The (1,1) element $P(\theta)$, which is called the phase function, is an important quantity used to describe the single scattering of a monochromatic beam by a volume element containing randomly oriented non-spherical particles. It describes the angular distribution of the scattered intensity and satisfies the normalization condition:

$$\frac{1}{2}\int_0^\pi P(\theta)\sin\theta d\theta = 1. \tag{2.1.8}$$

where θ is the scattering angle. the angular distribution of the scattered intensity. Traditionally, the phase function has been calculated directly for a

large set of scattering angles, which causes an unbearable computation time. To accelerate the *T*-matrix technique, the phase function is explicitly represented as a Legendre polynomial expansion [52]:

$$P(\theta) = \sum_{i=0}^{i_{\max}} \omega_i P_i(\cos\theta), \tag{2.1.9}$$

where $P_i(\cos\theta)$ are Legendre polynomials, the value of the upper summation limit $i_{\max}$ determines on the desired numerical accuracy of computations, and ω_i is the ensemble-average expansion coefficient which can be calculated with *T*-matrix method [53]:

$$\omega_i = \frac{1}{MC_{sca}} \sum_{m=1}^{M} \sum_{n=1}^{N} f'(r_n) \omega_i(r_n) C_{sca}^m(r_n) w_n, \tag{2.1.10}$$

where the index m = 1, …, M numbers aspect ratios, r_n and w_n (n = 1, …, N) are quadrature division points and weights, respectively, on the interval $[r_{\min}, r_{\max}]$. $f'(r)$ is the size distribution function, and r is the radius for spherical particles or radius of the equal-projected-area sphere for nonspherical particles, C_{sca} is the scattering cross section. $\omega_i(r_n)$ is the expansion coefficient at point r_n, and $C_{sca}^m(r_n)$ represents the scattering cross section at point r_n with an aspect ratio m.

The computation of the *T*-matrix involves a numerical integration over the zenith angle on the interval $[0,\pi]$ by using Gaussian quadrature [54]. The integral interval $[0,\pi]$ can be reduced to $[0,\pi/2]$ for axial symmetry. We use slightly rough cylindrical particles (Fig. 2.1.1b) to simulate scatterers in

mouse muscle tissue with different diameter-to-length ratios *D*/*L*. For high accuracy we divided the interval $[0,\pi/2]$ into two subintervals $[0, \arctan(D/L)]$ and $[\arctan(D/L), \pi/2]$, and applied Gaussian quadrature separately to each subinterval. By calculating ensemble-average expansion coefficients α_i using *T*-matrix method, the phase function can be obtained with Eq. (2.1.9).

The anisotropy factor, which is the mean cosine of the scattering angle used to measure the scattering retained in the forward direction following a scattering event [55], can be expressed as:

$$g = \int \mu P(\theta) d\Omega / \int P(\theta) d\Omega, \tag{2.1.11}$$

where $\mu \equiv \cos\theta$. Isotropic scattering can be described by the reduced scattering coefficient $\mu_s^{'}$, which is related to the anisotropic factor by $\mu_s^{'} = \mu_s(1-g),$ In an average sense, this relationship equates the number of anisotropic scattering steps, given by $1/(1-g),$ with one isotropic scattering event [55]. A more explicit formula is given as follows:

$$\mu_s^{'} = \int (1-\mu) P(\theta) d\Omega. \tag{2.1.12}$$

2.1.4 Size distribution

For non-spherical particles, the phase function is related to the equal-projected-area sphere size parameter *r* [31]. In order to average the light scattering characteristics over particles sizes, a size distribution *f(r)* must be

applied. Since currently there is no clear consensus as to the size distribution best describing biological tissue, we compare three size distributions of power law, normal, and skewed logarithmic distributions with our experiments. The power law distribution can be written as [48, 50]:

$$f_1(r) = c_0 r^{3-D_f}, \tag{2.1.13}$$

where D_f is the fractal dimension and c_0 is the normalization constant. The normal distribution can be given by [56]:

$$f_2(r) = 1/(\sqrt{2\pi}\sigma_m) \cdot \exp[-(r - r_m)^2/(2\sigma_m^2)], \tag{2.1.14}$$

where r_m and σ_m are the mean and standard variation, respectively. The general form of skewed logarithmic distribution can be expressed as [25, 57-59]:

$$f_3(r) = c_n r^n \exp[-(\ln r - \ln r_n)^2/(2\sigma_n^2)], \tag{2.1.15}$$

where c_n is a normalizing factor, and the quantities r_n and σ_n set the center and width of the distribution, respectively. For n = -1 and n = 0, the distribution function is called the logarithmic normal distribution and zeroth-order logarithmic distribution, respectively. Both distributions are used extensively in particle-size analysis [25, 59] .

Considering practical particle size and the *T*-matrix computation, the minimum and maximum particle size should be limited. Thus we modify the distribution functions to avoid the infinity while still remaining smooth:

$$f_i^{'}(r) = \begin{cases} c_i, & \text{for} \quad r \le r_{\min} \\ f_i(r), & \text{for } r_{\min} \le r \le r_{\max} \end{cases}, i = 1, 2, 3. \tag{2.1.16}$$

where $f_i(r)$ represents the three size distributions, c_i is a constant used to normalize the distribution function. r_{min} and r_{max} refer to the maximum and minimum particle size parameters. Accordingly, the effective radius and effective variance of a size distribution are defined as:

$$r_{eff} = \frac{1}{S}\int_{r_{\min}}^{r_{\max}} \pi r^3 f_i^{'}(r) dr, \tag{2.1.17}$$

and the effective variance is given by

$$v_{eff} = \frac{1}{S \cdot r_{eff}^2}\int_{r_{\min}}^{r_{\max}} \pi r^2 (r - r_{eff})^2 f_i^{'}(r) dr, \tag{2.1.18}$$

where S is the average cross-sectional area

$$S = \int_{r_{\min}}^{r_{\max}} \pi r^2 f_i^{'}(r) dr. \tag{2.1.19}$$

The effective size parameter is $S_{eff} = k \cdot r_{eff}$, where $k = 2\pi n_0 / \lambda$ is the wave number in the surrounding medium, and n_0 is the background refractive index.

2.2 Light scattering in biological tissue

The refractive index variation for biological tissue is approximately 0.04-0.10 with a background refractive index of n_0 = 1.35 [58]. We take the complex refractive index as 1.35 + 0.008i, where the imaginary part represents

for a small absorption coefficient. Considering microstructures ranging from organelles 0.2-0.5μm to nuclei 3–10μm in diameter [50], we take r_{min} = 0.2μm and r_{max} = 5μm, and thus v_{eff} = 0.12, r_{eff} = 3.355μm according to Eqs. (2.1.17-2.1.18). The wave length of the incident light is selected as 1100 nm. Therefore, the effective size parameter S_{eff} is 25.9.

We used a phase-contrast microscope to measure spatial variations in the refractive index of tissue. Fresh tissue specimens of mouse skeletal muscle were frozen and sectioned along the cross-section to a thickness of 5μm for immediate analysis after thawing. Images of specimens taken at magnifications of 40, 100, 200 and 400 were recorded with a CCD camera and stored in gray-scale format. Fig. 2.2.1 shows two typical phase-contrast images of mouse skeletal muscle taken at different magnifications.

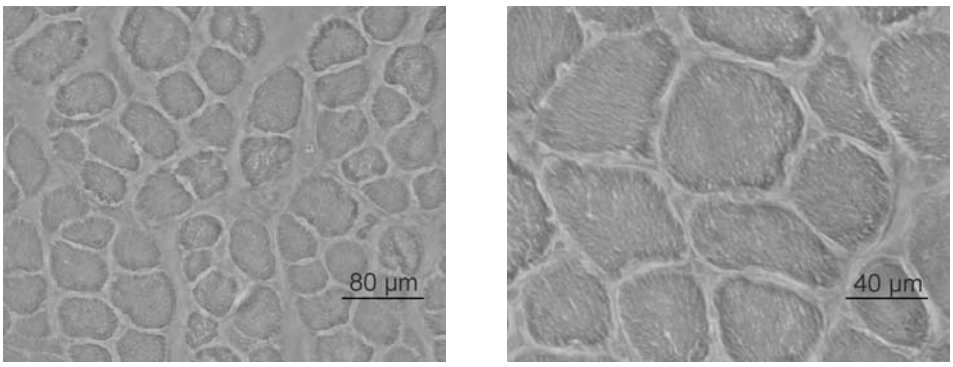

Fig. 2.2.1. Phase contrast images of mouse muscle tissue acquired at two different magnifications.

Since the tissue is cut in cross-sections, it is better to simulate the sample slice as a cluster of roughly cylindrical particles (Fig. 2.1.1b) with different equal-surface-area-sphere size parameters r and effective diameter-to-length ratios D/L. We assumed the parameter r satisfies the

modified power law distribution function (Eq. (2.1.10)) with fractal dimension D_f = 3.9671 obtained from experiments. We also assumed that D/L has a uniform distribution between 0.25 and 4. The computation of phase function is repeated for several randomly oriented cylindrical particles with D/L ranging from 0.25 to 4 with a step size of 0.25. Fig. 2.2.2 illustrates the phase function versus scattering angle for the rough cylinders with three different ratios D/L of 1/2, 1 and 2, and surface-equivalent spheres with effective size parameter S_{eff} = 25.9. One interesting feature is that the phase functions are insensitive to the dimension-to-length ratios D/L in most of the scattering regions for different kinds of rough cylinder. This agrees with claims that the phase function of a representative shape mixture of non-spherical particles is fairly insensitive to the elementary shapes used to form the mixture [53].

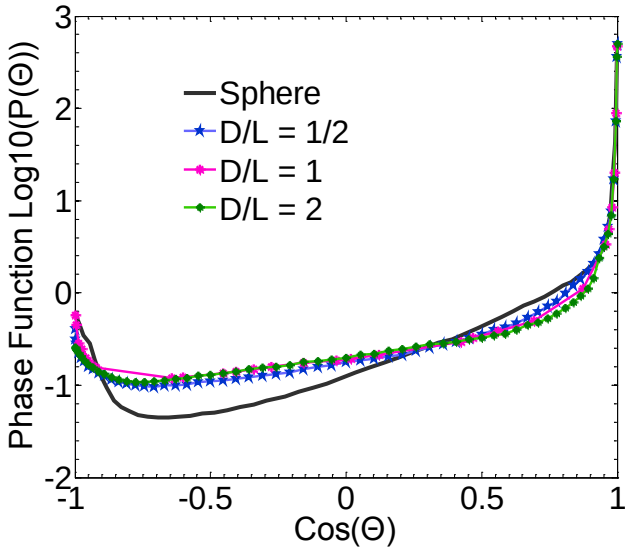

Fig. 2.2.2. Phase functions for randomly oriented rough cylinders with different ratios D/L of 1/2, 1 and 2, and surface-equivalent spheres with effective size parameter S_{eff} = 25.9.

Fig. 2.2.3 describes the phase functions calculated with a mixture of rough surface cylindrical particles, a cluster of surface-equivalent spheres, and also from experiments. The experimental results are obtained with a series of phase contrast images as in Fig. 2.2.1, by using our formerly-studied fractal mechanism [60]. As shown in Fig. 2.2.3, the random non-spherical model fits well with the experimental results, though there are slight differences in the forward scattering region and back scattering region, mainly caused by multiple scattering. The phase function for surface-equivalent spheres shows larger discrepancy with experiments, especially in the side-scattering and backscattering regions. Thus, our random non-spherical model has the power to simulate biological tissue better than the spherical model.

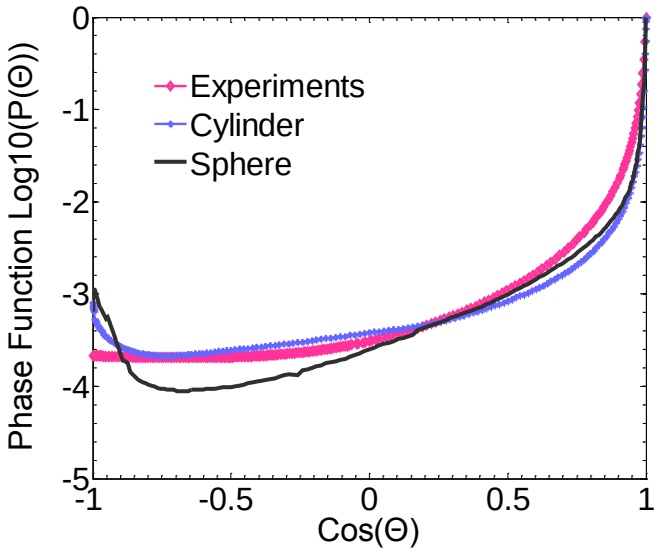

Fig. 2.2.3. Phase functions for randomly oriented rough cylinders with uniform distributed D/L, a cluster of surface-equivalent spheres with effective size parameter S_{eff} = 25.9, and experimental results.

Experimental results corroborate that scattering properties of non-spherical particles can be significantly different from those of equivalent

spheres. To understand better the light-scattering of biological tissue it is necessary to substitute the spherical model with the random non-spherical model. Finally, we note that our experimental results are limited to mouse skeletal muscle and the computational results pertain to a specific refractive index typical of biological tissue. To extrapolate our conclusions to other kinds of tissue, additional laboratory experiments with specific biological sample and additional corresponding calculations with various density and concentrations of the scatterers are necessary.

2.3 Light scattering in biological cells

Slightly rough surface random nonspherical particles were applied to simulate scattering centers in biological tissue and cells. Since the candidates for scattering centers in biological tissue and cells are the cell itself, the nucleus, and other organelles, and their microstructures range from peroxisomes and lysosomes 0.2-0.5 μm or smaller, to mitochondria approximately 0.3-0.7 μm in diameter and 1-4 μm in length, to nuclei 3-10 μm in diameter [61-62]. We assume the size of the random particles is not too large compared with the incident wavelength and the particle orientation is uniform distributed. Fig. 2.3.1 illustrates phase functions computed by randomly oriented slight rough surface cylinders [63] with three size distributions at wavelength of 1100 nm. Parameters are selected to retain the

same values of r_{eff} and v_{eff}, which are 3.36 and 0.12, respectively. It is interesting to notice that different size distributions have similar phase functions providing the same values of r_{eff} and v_{eff}. The result is quite practical and important, since only two key parameters can provide a unified classification of all distributions, and the same result can be obtained for many different analytical parameterizations of natural size distributions [64]. Currently the size distribution best describing biological tissue is not clear, because of the complicated structure of tissue, composed of tightly packed groups of cells entrapped in a network of fibers through which water percolates. The two key parameters r_{eff} and v_{eff} provide an effective approach to describe the scattering properties of the biological tissue.

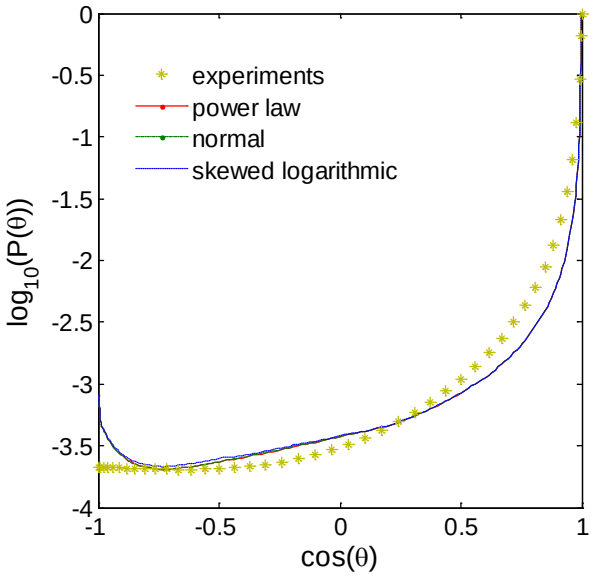

Fig. 2.3.1. Phase functions with different size distribution functions with same $r_{eff} = 3.36$ and $v_{eff} = 0.12$, and same shape parameters (K = 2, τ = 0.7, CP = -0.5), at incident wavelength 1100 nm.

Here slightly rough surface spheroids, including both oblate and prolate spheroids, are used to model light scattering properties of rat embryo fibroblast cells (M1) and mitochondria *in vitro*. Experimental data were reported by Mourant *et al.* [29]. According to Schmitt [58], the refractive index variation for the scatterers in M1 cells and the media are 1.4 and 1.35, respectively. Therefore we take the complex refractive index as 1.38 + 0.008i, and characterize the size of the random spheroids with the radius of the equal-projected-area sphere. Fig. 2.3.2 compares the phase functions of prolate and oblate rough surface spheroids, with those of equal-projected-area spheres, at different effective size parameters after size and orientation averaging. It shows that phase functions of nonspherical particles are quite different from those of equal-projected-area sphere, especially in the side-scattering and backscattering region. Even for a single rough surface spheroid, it produces a unique, shape-specific phase function. Similar results can be found in the literature of Macke et al. [65] and Muinonen [66]. However, in Figure 2.3.2, the phase functions are similar for prolate and oblate spheroids with small aspect ratios. This is understandable, because for small aspect ratios, the shape difference between prolate and oblate spheroids is negligible.

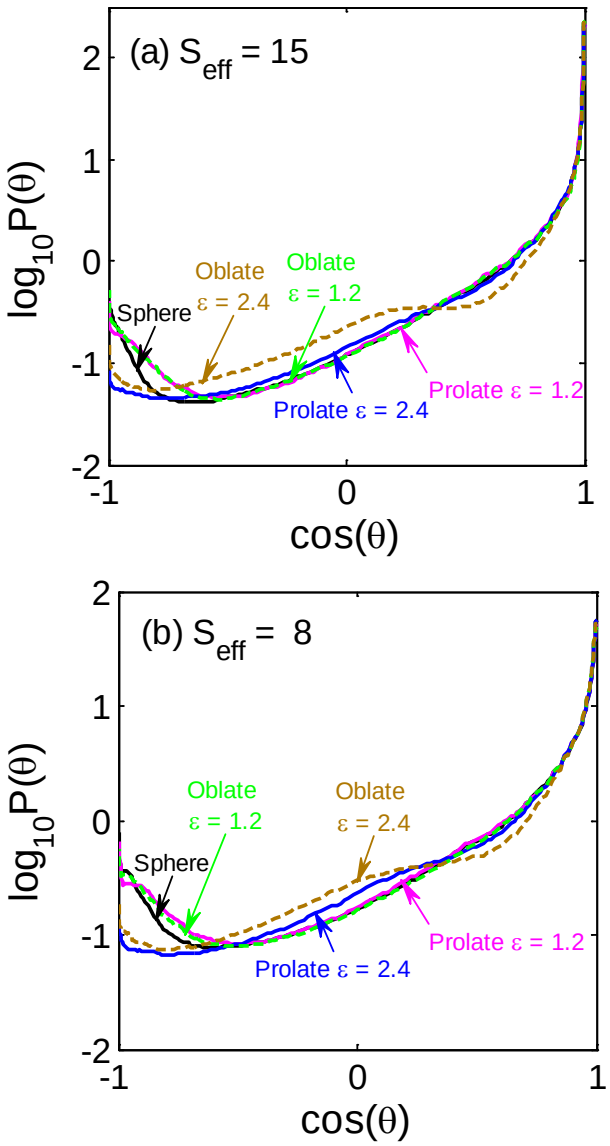

Fig. 2.3.2. Phase functions for randomly oriented slight rough prolate (solid curves) and oblate (dash curves) spheroids with different aspect ratios of 1.2, 2.4, and equal-projected-area spheres with different effective size parameter S_{eff} .(a) S_{eff} = 15; (b) S_{eff} = 8;

Figs. 2.3.3 and 2.3.4 compare the phase functions measured by experiments with those calculated by a spherical model and a nonspherical

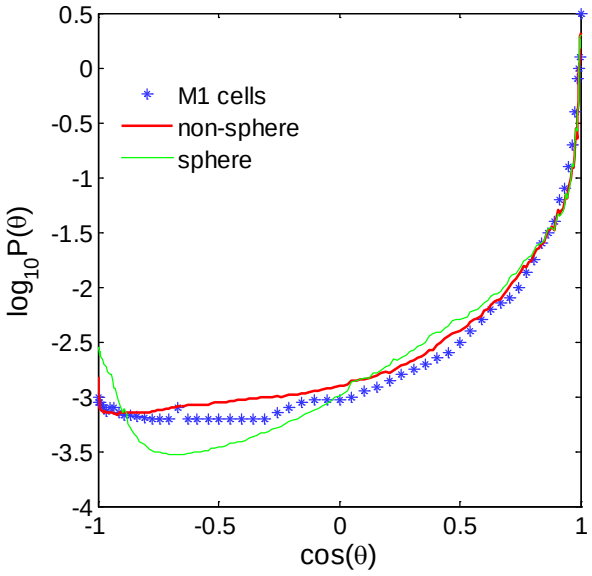

Fig. 2.3.3. Phase functions for suspensions of rat embryo fibroblast cells (M1) with spherical and nonspherical model with the effective size parameter $S_{eff} = 15.5$ and experimental results.

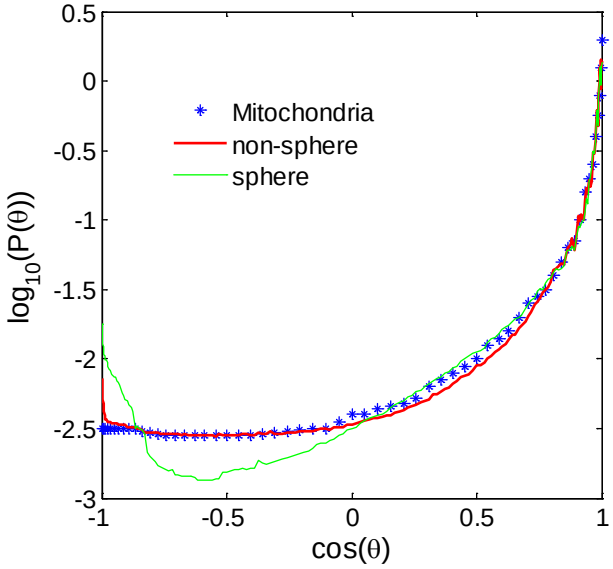

Fig. 2.3.4. Phase functions for suspensions of mitochondria with random non-spherical model, spherical model with the effective size parameter $S_{eff} = 10.3$ and experimental results.

model which is mixture of prolate and oblate slightly rough surface spheroids.

The theoretical computations are obtained by averaging over a wide

aspect-ratio distribution of prolate and oblate spheroids. To simplify the calculation, we assume the aspect ratios are uniformly distributed, centered at the aspect ratio 2 for both prolate and oblate spheroids, while the incident wavelength is taken as 760 nm. Note that in the exact forward scattering region, the phase function is insensitive to particle nonsphericity and the equal-projected-area spheres can be used to characterize the randomly oriented nonspherical particles. It means that Mie theory can be used to analyze transmittance measurements of biological tissue and cells in microscope without causing significant errors. However, the difference between spherical and non-spherical models becomes quite obvious in the side-scattering and backscattering regions, and therefore the results from Mie theory would cause serious errors in biological image detection when applied to analyze reflectance measurements in a microscope.

Table 2.3.1 gives the anisotropy factors g and reduced scattering coefficients μ_s' from experiment data, and computations with nonspherical and spherical models, respectively. Compared with the experiment data, the difference of g between nonspherical and spherical models is small, which confirms our conclusion that forward scattering is least sensitive to particle nonsphericity. The same phenomenon can be found in μ_s', which means that in the diffusion regime, the number of anisotropic steps of both nonspherical and spherical models are similar.

Table 2.3.1. Anisotropy factors and reduced scattering coefficients for M1 cells and mitochondria.

	Experiments		Spheroids		Sphere	
	g	μ_s'	g	μ_s'	g	μ_s'
M1 cell	0.90	1.21	0.87	1.32	0.88	1.27
Mitochondria	0.78	3.65	0.79	3.49	0.80	3.52

Slightly rough surface spheroids are used to model scatter center in biological cells. Experimental results corroborate that scattering properties of non-spherical particles can be significantly different from those of equivalent spheres in both biological tissue and biological cells. To understand better the light-scattering mechanism, it is necessary to substitute the spherical model with the random non-spherical model. Finally, we note that our experimental results are limited to M1 cells and mitochondria and the computational results pertain to a specific refractive index scale of biological tissue. To extrapolate our conclusions to other kinds of tissue, additional laboratory experiments of the specific biological sample and the corresponding calculations are necessary.

Chapter 3 Image formation in confocal microscopy using divided apertures

3. 1 Diffraction analysis for coherent imaging in confocal scanning microscope with D-shaped apertures

3.1.1 Three-dimensional coherent transfer function

The divided-aperture technique has been widely applied in microscopy, stemming from the fact that the illumination and detection beams overlap only in the focal region, resulting in an angular gating effect and thus improving rejection of scattered light [33]. Since for weakly scattering objects, 3-D transfer functions can be used to completely describe image formation, it is important to derive the 3-D transfer functions for the confocal microscope with D-shaped pupils. The geometry of the confocal microscope with two D-shaped pupils is given by Fig. 3.1.1.

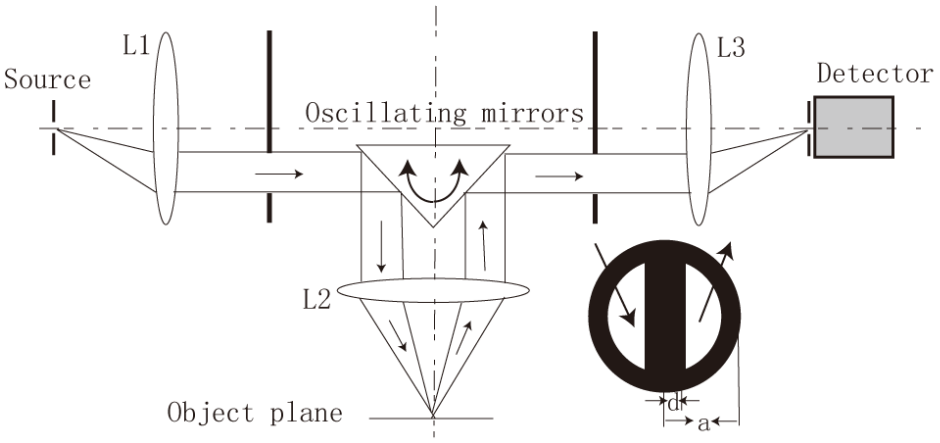

Fig. 3.1.1. Geometry of the confocal microscope with two centro-symmetric D-shaped pupils.

In a coherent confocal scanning microscope system with point detector, assuming that the objective and collector lenses are aberration-free, we can express the image intensity of a thick object with amplitude reflectivity $t(x, y, z)$ as [67]:

$$I(\mathbf{r_s}) = \left| \int_{-\infty}^{\infty} c(\mathbf{m}) T(\mathbf{m}) \exp(2\pi i \mathbf{m} \cdot \mathbf{r_s}) d\mathbf{m} \right|^2 , \tag{3.1.1}$$

where $r_s = (x_s, y_s, z_s)$ is the scan point, **m** represents the spatial frequency vector with two transverse components *m* and *n*, and one axial component *s*. *c*(**m**) is the 3-D amplitude coherent transfer function (CTF). *T*(**m**) is the Fourier transform of $t(x, y, z)$.

Consider a single D-shaped pupil with outer radius a and normalized distance parameter d $(0 \le d \le 1)$ (Fig. 3.1.1). The defocused pupil function under the paraxial approximation can be expressed as:

$$P(\rho, \theta, u) = \begin{cases} \exp[-i(u/2)\rho^2], & d \le \rho \le 1 \,\&\, -\cos^{-1}(\rho/d) \le \theta \le \cos^{-1}(\rho/d) \\ 0, & otherwise \end{cases} , \tag{3.1.2}$$

in cylindrical coordinates, where $\rho = r/a$ denotes the normalized radial coordinate, *r* is the real radial coordinate, and *u* is the axial optical coordinate defined as

$$u = (8\pi n/\lambda) z \sin^2(\alpha/2). \tag{3.1.3}$$

Here λ and $n\sin\alpha$ are the incident wavelength and the numerical aperture (NA) of the objective, respectively, and z is the defocus distance from the focal plane.

The point spread function (PSF) of the overall confocal system is given by:

$$h(v_x, v_y, u) = h_1(v_x, v_y, u)h_2(v_x, v_y, u), \tag{3.1.4}$$

where h_1 and h_2 denote the PSFs corresponding to the objective and collection lenses. For the reflection-mode confocal scanning microscope system, the two PSFs are centro-symmetric and can be written as

$$\begin{aligned} h_1(v_x, v_y, u) &= h_2(-v_x, -v_y, u) \\ &= \iint P(\rho, \theta, u)\exp[-i(v_x\rho\cos\theta + v_y\rho\sin\theta)]\rho d\rho d\theta. \end{aligned} \tag{3.1.5}$$

where v_x and v_y are the transverse optical coordinates given by:

$$v_x^2 + v_y^2 = ((2\pi n/\lambda)r\sin\alpha)^2. \tag{3.1.6}$$

The 3-D coherent transfer function $c(l, \psi, s)$ for the confocal system is given by the 3-D Fourier transformation of the amplitude PSF, which can be expressed as:

$$\begin{aligned} c(l, \psi, s) &= F_3[h_1(v_x, v_y, u)h_2(v_x, v_y, u)] \\ &= F_3[h_1(v_x, v_y, u)h_1(-v_x, -v_y, u)], \end{aligned} \tag{3.1.7}$$

where F_3 denotes the 3-D Fourier transformation. Here $l = \sqrt{m^2 + n^2}$ represents the radial spatial frequency, ψ is the azimuth, while s is the axial

spatial frequency. According to Fourier transform theory, Eq. (3.1.7) can be rewritten as:

$$c(l,\psi,s)=\int[P(\rho,\theta,u)\otimes_2 P(\rho,\theta+\pi,u)]\exp(-ius)du, \qquad (3.1.8)$$

where $\otimes_2$ represents the 2-D convolution operation with respect to l and ψ. Substituting Eq. (3.1.2) into Eq. (3.1.8) and evaluating the convolution gives:

$$c(l,\psi,s)=\iint_{\sigma}\delta(s-\rho^2-l^2/4)\rho d\rho d\theta, \qquad (3.1.9)$$

where σ is the area overlapped by the two D-shaped pupils (Fig. 3.1.2).

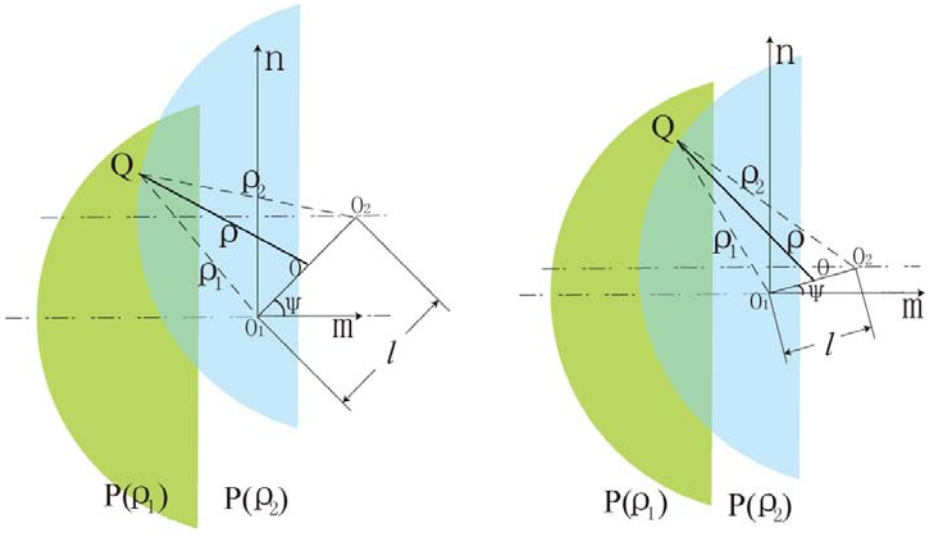

Fig. 3.1.2. 2-D convolution of two D-shaped pupils $P(\rho_1)$ and $P(\rho_2)$. Q is an arbitrary point on the boundary of the overlapping region. The lengths of O_1Q and O_2Q are ρ_1 and ρ_2, respectively. The distance between O_1 and O_2 is l.

For a confocal reflection microscope with two D-shaped pupils, the range of imaged transverse spatial frequency l for confocal reflective system is centro-symmetric as illustrated in Fig. 3.1.3. It can be seen that the effective

transverse frequency is divided into two cases: region A (blue area) and region B (green area), according to the overlapping areas shown in Fig. 3.1.2(a) and Fig. 3.1.2(b), respectively. Due to the centro-symmetry of the effective region, we can consider only the first quarter region of the transverse spatial frequency, where ψ ranges from 0 to $\pi/2$. The pink circle in Fig. 3.1.3

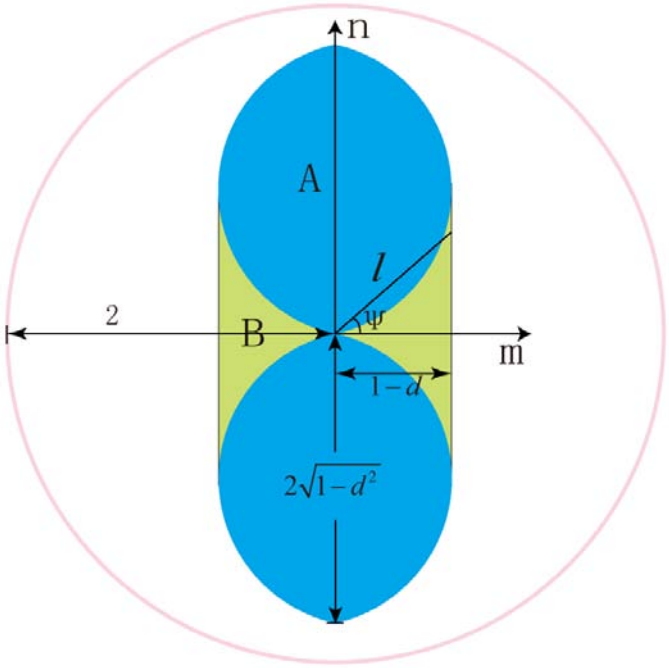

Fig. 3.1.3. Effective region of *l* in confocal microscope with two D-shaped pupils compared with the conventional confocal microscope with two circular pupils.

indicates the transverse cut-off frequency of the conventional confocal microscope with circular pupils. Compared with the conventional confocal microscope, the effective transverse frequency region for the confocal microscope with two D-shaped pupils is no longer circular: the transverse cut-off frequency varies with the angular parameter ψ from $1-d$ to $2\sqrt{1-d^2}$, in contrast with the conventional confocal microscope where the

transverse cut-off frequency is a constant of 2 [5, 67]. When d = 0, which indicates the semi-circular pupils, the transverse cut-off frequency reaches its maximal value of 2 at $\psi = \pi/2$. While this reduces the transverse resolution of the system, it also has an effect of increasing the angular sensitivity to specular reflections from surfaces normal to the optical axis, which also increases as d is increased [68].

After mathematical manipulations, the 3-D CTF $c(l,\psi,s)$ normalized by the value of $c(l=0,\psi=0,s=0)$ at $d=-1$ (corresponding to the circular pupils), can be derived as:

In region A: $(m+d)^2+(n-\sqrt{1-d^2})\le 1$, and $0\le m\le 1-d$.

$$c_A(l,\psi,s)=\frac{1}{2\pi}\int_{\vartheta 0}^{\vartheta 1}\int_{(d+m/2)/\cos\theta}^{\rho_0}\delta(s-\rho^2-l^2/4)\rho d\rho d\theta. \qquad (3.1.10)$$

In region B: $(m+d)^2+(n-\sqrt{1-d^2})\ge 1$, and $0\le m\le 1-d$.

$$c_B(l,\psi,s)=\frac{1}{2\pi}\int_{\vartheta 0}^{\vartheta 2}\int_{(d+m/2)/\cos\theta}^{\rho_0}\delta(s-\rho^2-l^2/4)\rho d\rho d\theta. \qquad (3.1.11)$$

where $m=l\cos\psi$, $n=l\sin\psi$, and

$$\begin{cases}\vartheta_0=-\tan^{-1}\{[\sqrt{1-(d+m)^2}-n/2]/(d+m/2)\},\\ \vartheta_1=\tan^{-1}\{[\sqrt{1-d^2}-n/2]/(d+m/2)\},\\ \vartheta_2=\tan^{-1}\{[\sqrt{1-(d+m)^2}+n/2]/(d+m/2)\},\\ \rho_0=-l\,|\cos(\psi+\theta)|/2+\sqrt{1-l^2\sin^2(\psi+\theta)/4}.\end{cases} \qquad (3.1.12)$$

Therefore, the 3-D coherent transfer function in frequency domain can be expressed as:

$$c(l,\psi,s)=\begin{cases} c_A(l,\psi,s), & \text{when} \quad \tan^{-1}[\sqrt{1-d^2}\,/\,(1-d)] \le \psi \le \pi/2, \\ c_A(l,\psi,s)+c_B(l,\psi,s), & \text{when} \quad 0<\psi<\tan^{-1}[\sqrt{1-d^2}\,/\,(1-d)], \\ c_B(l,\psi,s), & \text{when} \quad \psi=0. \end{cases}$$

(3.1.13)

It should be pointed out that the amplitude coherent transfer function in Eq. (3.1.13) has a constant spatial frequency shift s_0 along the *s*-direction [69], given by:

$$s_0=\frac{1}{2\sin^2(\alpha/2)}. \tag{3.1.14}$$

Considering the special case of $\psi=0$, $c(l,0,s)$ becomes a one-dimensional coherent transfer function along the *m* direction:

$$c(l,0,s)=\begin{cases} 1/\pi\cos^{-1}(\dfrac{d+l/2}{s-l^2/4}), & d^2+l^2/2+dl \le s \le 1+l^2/2-l, \\ 1/\pi[\cos^{-1}(\dfrac{d+l/2}{s-l^2/4})-\cos^{-1}(\dfrac{1-s}{l\sqrt{s-l^2/4}})], & 1+l^2/2-l \le s \le 1-l^2/2-dl. \end{cases}$$

(3.1.15)

Confocal microscopy can be implemented using a single-mode optical fiber in place of the physical confocal pinhole, called FOCSM (fiber optic confocal scanning microscope) [70-74]. Such an arrangement is practically useful because fiber optic technology is compatible with an endoscopic device [75].

In FOCSM where optical fibers are used as an illumination source and a signal collector, the system is still fully coherent even with a finite fiber spot size, thus the imaging can be described by the 3-D CTF [5, 76]. For simplicity, considering the case that the illumination fiber and the collection fiber are identical single-mode fibers, the 3-D CTF for the FOCSM with two centro-symmetric D-shaped pupils can be expressed as [76-77]:

$$c_f(l,\psi,s) = K\exp(-Al^2/4)\iint_\sigma \exp(-A\rho^2)\delta(s-\rho^2-l^2/4)\rho d\rho d\theta, \tag{3.1.16}$$

where K the constant of normalization, $A=(2\pi r_0 n\sin\alpha/\lambda)^2$, which incorporates the effects of the radius of single mode fiber r_0, the wavelength and the numerical aperture of the objective. Therefore, the 3-D CTF normalized by $c(l=0,\psi=0,s=0)$ at $d=-1$ and $A=0$ can be given by:

$$c_f(l,\psi,s) = \exp(-As)c(l,\psi,s), \tag{3.1.17}$$

where the expression for $c(l,\psi,s)$ is given by Eq. (3.1.13). When $A=0$, Eq. (3.1.17) can be reduced to Eq. (3.1.9), which corresponds to the CTF with a point detector.

Fig. 3.1.4 gives the complete view of the 3-D CTF $c(l,\psi,s)$ in the reflection-mode confocal scanning microscope with two D-shaped pupils for different distance parameter d and different angular parameter ψ. For the special case of $d=0$ and $\psi=\pi/2$, the 3-D CTF is the same as the conventional confocal microscope with two circular pupils. It is interesting to

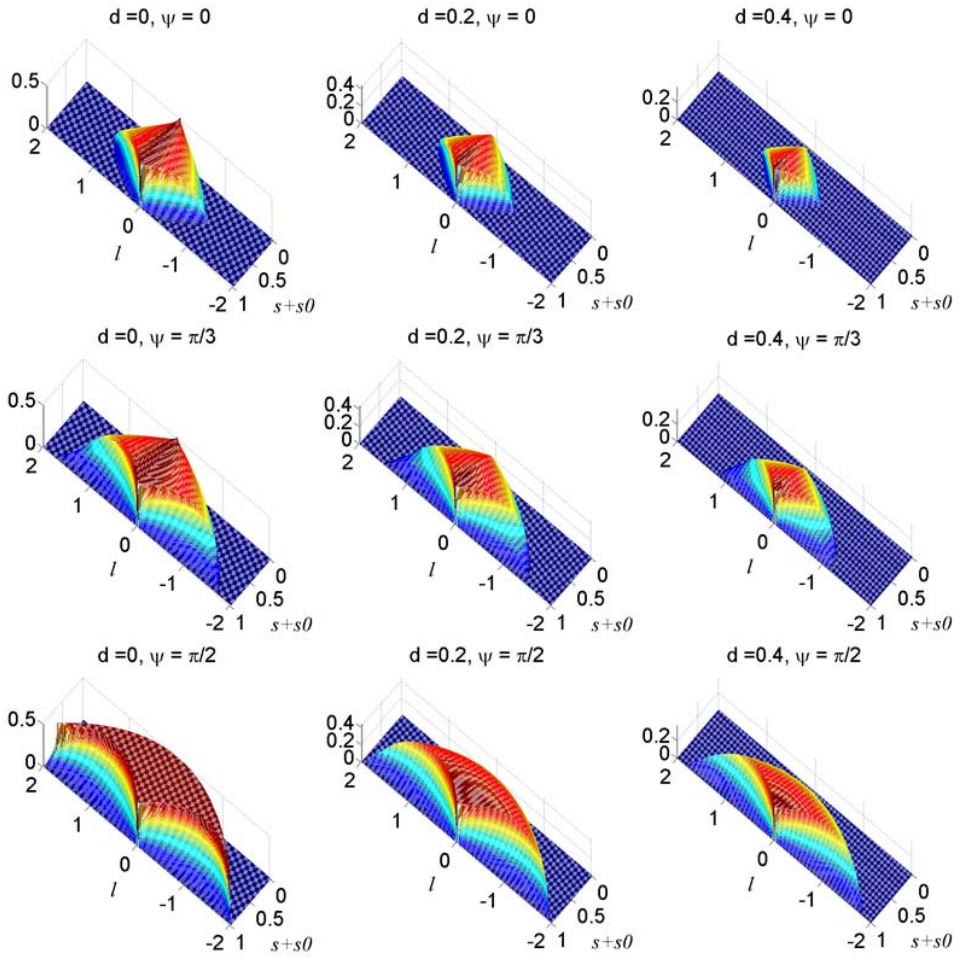

Fig. 3.1.4. The 3-D coherent transfer functions with different distance parameter *d* and different angle ψ. For *d* = 0 and $\psi = \pi/2$, the 3-D CTF is the same as the conventional confocal microscope with two circular pupils.

note that the transverse cut-off frequency $l_{cutoff}(d,\psi)$ depends on both *d* and ψ; while the axial cut-off frequency $s_{cutoff}(d)$ only depends on *d*. For a given ψ, as *d* is increased, both the axial cut-off frequency and the transverse cut-off frequency reduce. However, for a given *d*, as ψ increases, only the transverse cut-off frequency increases and reaches the maximum of $l_{cutoff}(\pi/2,\psi) = 2\sqrt{1-d^2}$ at $\psi = \pi/2$; while the axial cut-off frequency remains at $s_{cutoff}(d) = d^2$. Therefore, in the region $0 \le s + s_0 \le d^2$, the value of

the CTF is zero, which indicates that the image information in this region is missing, thus the low axial frequency region cannot be imaged.

The degradation effect can be further displayed in Fig. 3.1.5, which illustrates the distribution of $c(l=0,s)$ for confocal microscope with two D-shaped pupils at different d values. Since the strength of the optical sectioning effect is determined by the modulus square of $c(l=0,u)$, which is the inverse Fourier transform of $c(l=0,s)$ [67], the optical sectioning of the

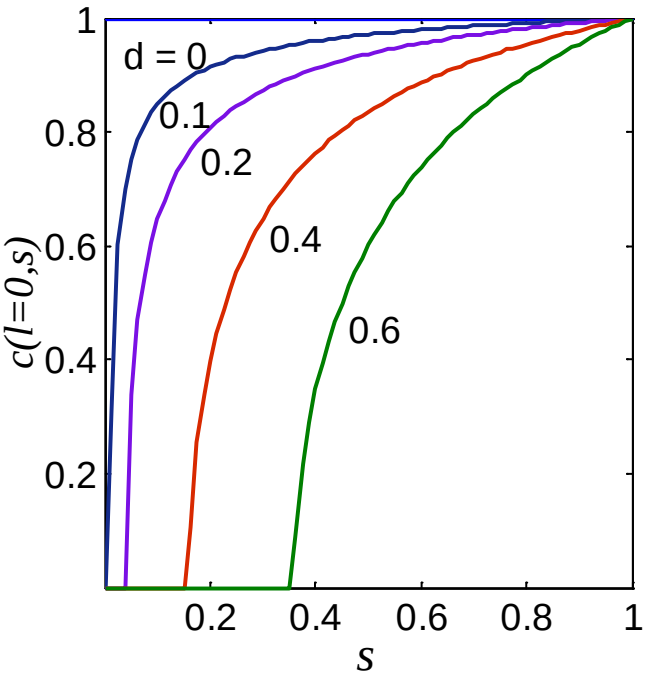

Fig. 3.1.5. The 3-D coherent transfer function c (l = 0, s) as a function of the distance parameter d.

confocal microscope can be analyzed through the scale of $c(l=0,s)$. It is important to notice that for confocal microscope with two D-shaped pupils, $c(l=0,s)$ is no longer a square function as in the conventional confocal microscope. The shape of the variation $c(l=0,s)$ is independent on ψ but dependent on d, and its length is given by 1 - d^2. Therefore, as d is increased,

$c(l=0,s)$ becomes narrower, indicating a degradation of the optical sectioning. A compromise must therefore be reached between optical sectioning and efficiency of rejection of scattered light [12].

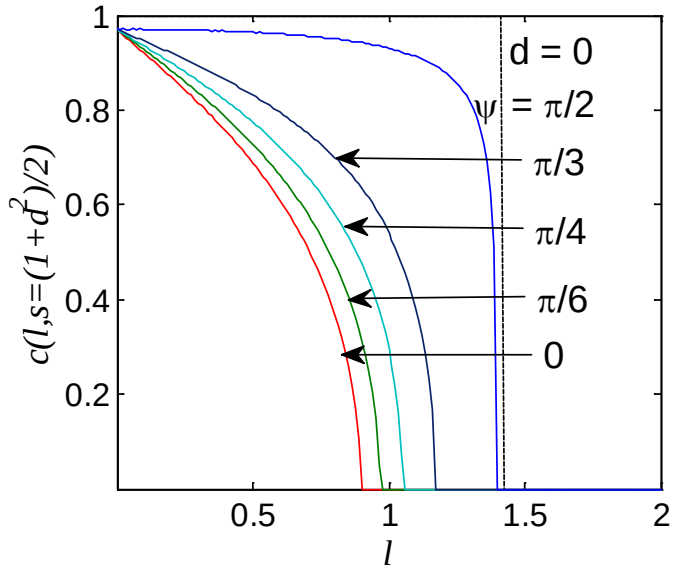

(a)

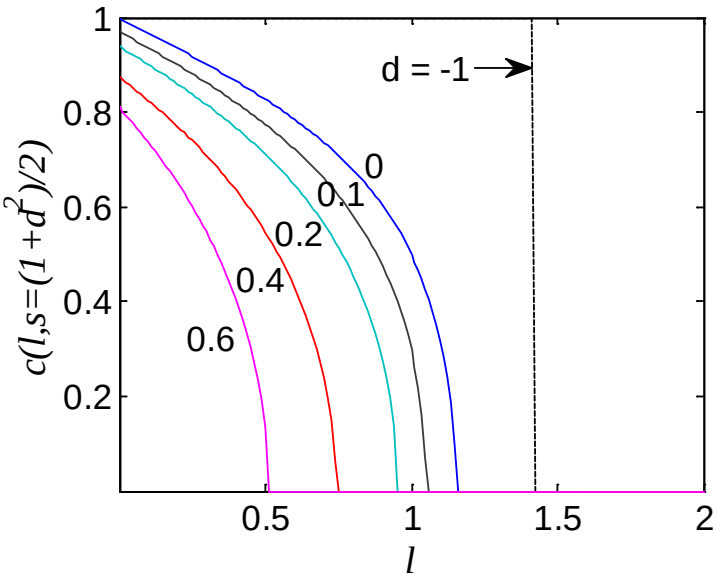

(b)

Fig. 3.1.6. Transverse cross sections, (a) for different angular parameter ψ with d = 0.1; (b) for different distance parameter d with $\psi = \pi/4$.

Fig. 3.1.6 shows the cross sections of the 3-D CTF at $s = (1+d^2)/2$, which corresponding to the middle transverse section of the 3-D CTF in the non-zero region, for different angle ψ (Fig. 3.1.6(a)) and different distances d (Fig. 3.1.6(b)). For a particular value of d, as ψ is increasing, the transverse cut-off frequency also increases and the value of CTF decays much slower. However, for a given ψ, as d increases, the transverse cut-off frequency decreases and the value of the CTF decays faster. It is also seen that both the transverse cut-off frequency and the decay rate of the CTF are more sensitive to the value of d than the value of ψ.

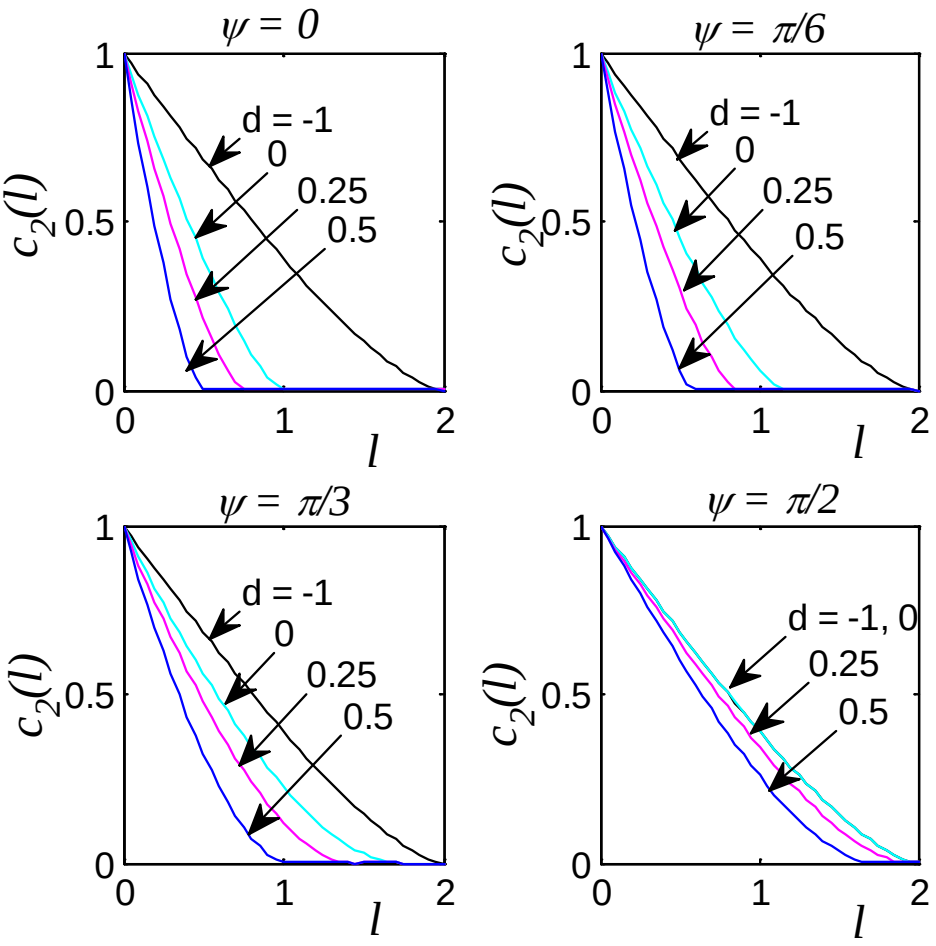

Fig. 3.1.7. 2-D in-focus CTF in a confocal microscope with two centro-symmetric D-shaped pupils.

If a thin planar object is located on the focal plane, the in-focus CTF $c(l,u=0)$ is determined by the integration of the 3-D CTF $c(l,s)$ with respect to the variable *s* [12]. The result is shown in Fig. 3.1.7 for different values of *d* and angle ψ, from which we can see that the dependence on angle ψ decreases when *d* is smaller. Figs. 3.1.5-3.1.7 demonstrate that the CTF contains much information concerning the optical performance of the imaging system.

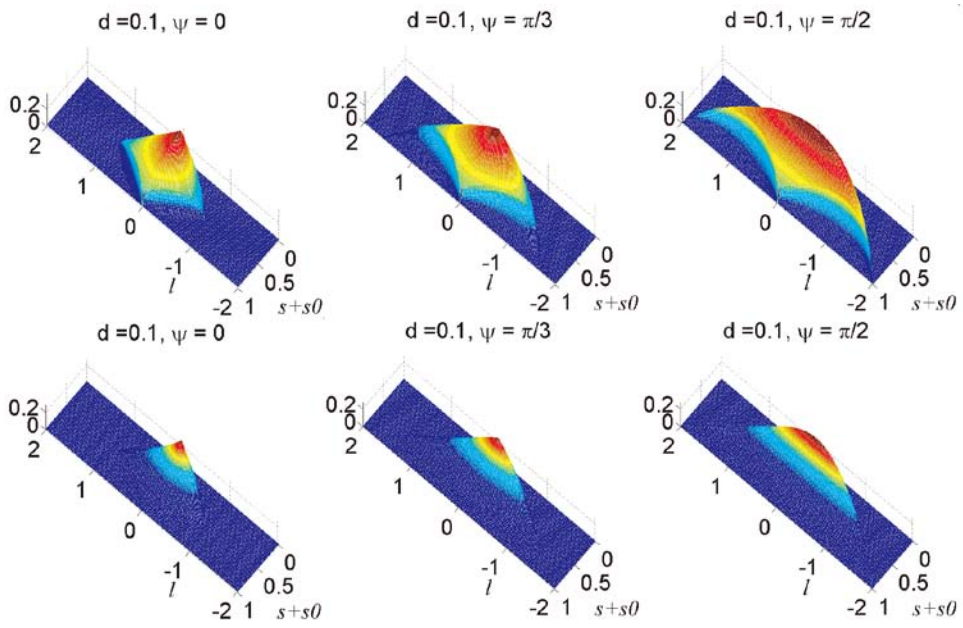

Fig. 3.1.8. The 3-D coherent transfer functions for FOCSM at *d* = 0.1, with different parameter *A* and different angle ψ.

For FOCSM with identical single-mode illumination fiber and collection fiber, the 3-D CTF can be given by Fig. 3.1.8. It is seen that for a given distance parameter *d*, the 3-D CTF is decreased as *A* increases. When $A=5,$ which is shown in the bottom row of Fig. 3.1.8, the 3-D CTF exhibits

a considerable decrease along both the transverse and axial direction, indicating degraded resolution in both directions.

In conclusion, the 3-D CTF for reflection-mode confocal scanning microscope using D-shaped pupils has been analytically derived. It can be seen from the numerical results that the transverse resolution is degraded by increasing the distance parameter *d* of the D-shaped pupils in confocal system with point detector. However, for the same distance parameter *d*, the degree of degradation is reduced as the angle ψ increases. In addition, the 2-D in-focus CTF for thin objects, which can be expressed as the projection of the 3-D CTF in the focal plane, is also dependent on both *d* and ψ. It should be emphasized that the above analysis is based on a coherent confocal system with point detector. For a finite-sized detector, the system becomes partially coherent. Therefore, the CTF is no longer valid for that system and a partially coherent transfer function should be derived instead. For FOCSM, the system is coherent even for a finite-sized fiber spot. Therefore, the 3-D CTF with identical single-mode illumination fiber and collection fiber of the confocal microscope with two D-shaped pupils can be derived based on former calculation. As A increases, the 3-D CTF decreases, which indicates a degradation in both transverse and axial resolution. In practice the fiber spot size should be kept to a minimum to maintain resolution, but a compromise must be made with signal strength [78].

3.1.2 Coherent imaging in confocal scanning microscope with D-shaped apertures

The amplitude in the focal region of a lens is calculated from the paraxial Fresnel diffraction formula [79]:

$$h(v_x, v_y, u) = \frac{1}{\pi} \iint_P P(\rho_x, \rho_y) \exp\left\{ i \left[v_x \rho_x + v_y \rho_y - \frac{1}{2} u(\rho_x^2 + \rho_y^2) \right] \right\} d\rho_x d\rho_y . \tag{3.1.18}$$

Here v_x, v_y, u are optical coordinates given by Eqs (3.1.3, 3.1.6). The coordinates ρ_x, ρ_y are distances in the pupil plane, normalized by the pupil radius a. The pupil is a D-shaped segment of a circle, with a boundaries at $\rho_x = d$ and $\rho = (\rho_x^2 + \rho_y^2)^{1/2} = 1$.

Figure 3.1.9 shows a plot of the variation with defocus of the intensity point spread function, normalized by the maximum intensity at each defocus plane, for a D-shaped pupil for $d = 0.1$. As defocus increases, the illuminated region becomes closer in shape to that of the pupil, but a bright Poisson spot begins to form on the axis. Figure 3.1.10 shows contour plots of *x*-*z* and *y*-*z* cross-sections through the intensity point spread function. The behaviour in the *x*-*z* plane agrees with the results of Török [43], while in the *y*-*z* plane the behaviour is very similar to that for a plain circular aperture [79].

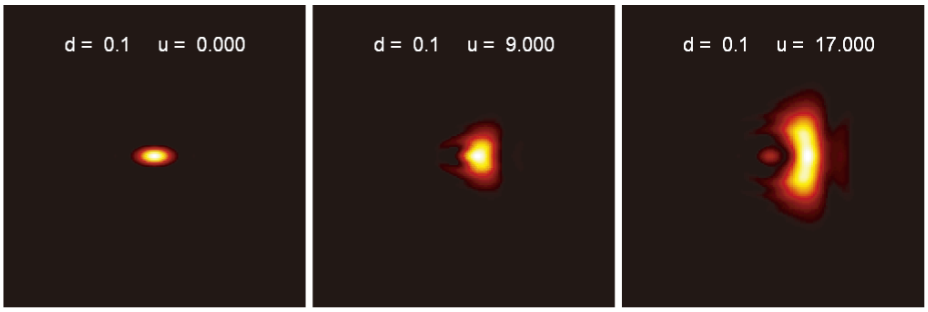

Fig. 3.1.9. The intensity point spread function for a D-shaped pupil for d = 0.1.

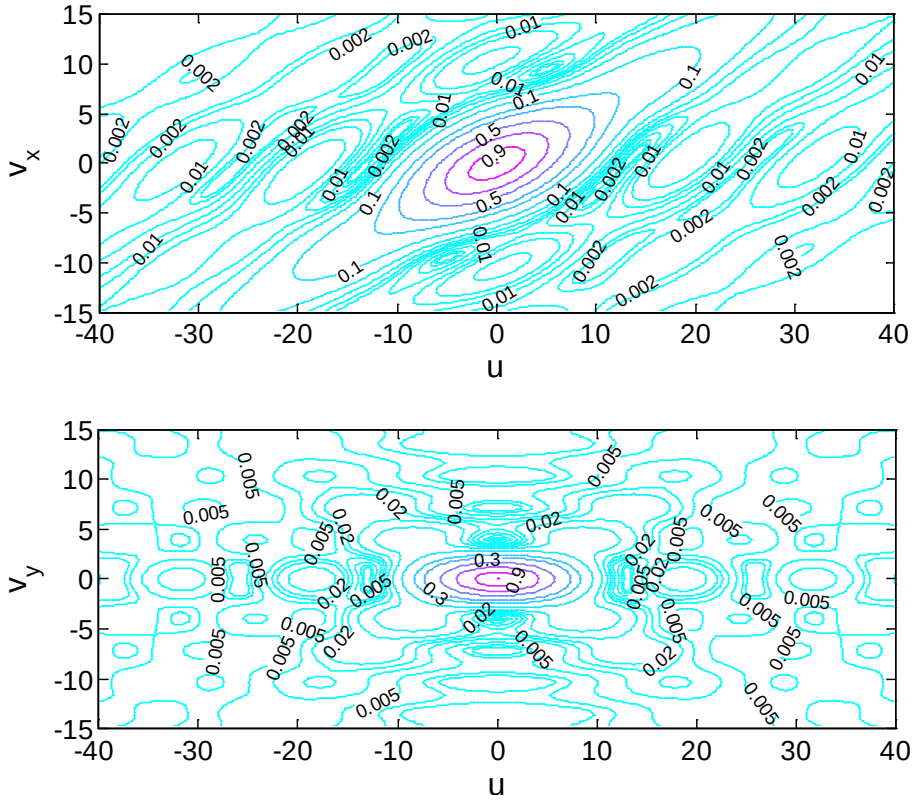

Fig. 3.1.10. Cross-sections through the intensity point spread function for a D-shaped pupil for d = 0.1: (a) x-z section, (b) y-z section.

The intensity along the axis can be calculated by transforming to polar coordinates ρ, ϕ where $\rho^2 = t = \rho_x^2 + \rho_y^2$ and performing the integration in ϕ first, to give

$$P(t) = \int_0^{2\pi} P(\rho,\phi)\, d\phi = \frac{2}{\pi}\arccos\left(\frac{d}{\sqrt{t}}\right). \qquad (3.1.19)$$

Then the amplitude at the focus is $\sqrt{\ }$

$$U(0) = \frac{2}{\pi}\left[\arccos(d) - d\left(1-d^2\right)^{1/2}\right] \qquad (3.1.20)$$

and the amplitude along the axis is

$$U = \frac{2}{\pi}\int_{d^2}^{1} P(t)e^{-iut/2}dt\,. \qquad (3.1.21)$$

Figure 3.1.11 shows the pupil function $P(t)$ for different values of *d*, and Fig. 3.1.12 shows a log-log plot of the intensity along the axis, which is the Fourier transform of $P(t)$ for a D-shaped pupil, normalized by the intensity at the focal point. As *d* increases, the width of the central lobe in the axial intensity also increases. For $d = 0$, the intensity along the axis decays asymptotically as $1/u^2$, which behaves the same as the circular apertures (*d* = -1). But as *d* increases, the asymptotic behaviour of the intensity for intermediate values of *u* tends to fall off more quickly. An optimum value for the absolute value of the slope of about 2.2 is achieved at $d \approx 0.07$. For large *u* (>2000), the absolute value of the slope becomes two, for any value of *d*, as is expected from the theory of asymptotic values of Fourier transforms [80].

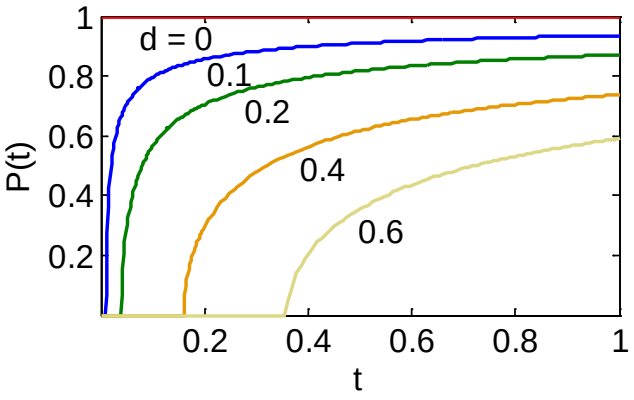

Fig. 3.1.11. The pupil function *P(t)* for different values of *d*.

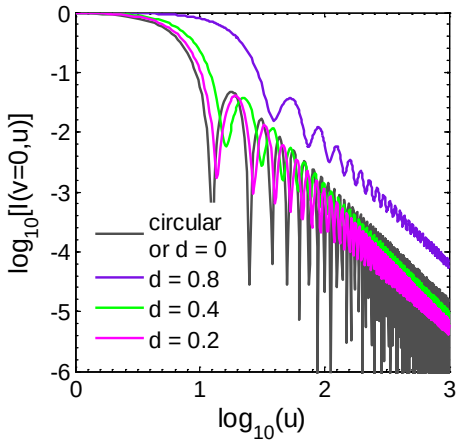

Fig. 3.1.12. The intensity along the axis for a D-shaped pupil shown as a log-log plot.

Figure 3.1.13 shows the variation with defocus of the intensity, normalized by the central point intensity at each defocus plane, in the image of a point object in a confocal system consisting of two D-shaped pupils and a point detector. As the defocus increases, the illumination and detection point spread functions tend not to overlap, so their product is zero, but the Poisson spot of each pupil coincides and hence remains strong. The intensity along the axis is thus just the square of that for a single D-shaped pupil. For $d = 0$, the

intensity along the axis decays as $1/u^4$, but as d increases, the asymptotic behaviour of the intensity for intermediate values of u again tends to fall off more quickly. An optimum value for the absolute value of the slope of about 4.4 is achieved at $d \approx 0.07$. For large u (>2000) the absolute value of the slope becomes four, independent of the value of d. Figure 3.1.14 shows a contour plots of x-z cross-section through the intensity image of a point object. This can be compared with the diamond shape predicted by Koester for a theory based on geometrical optics [8]. In the y-z plane, the intensity is just the square of that from a single D-shaped pupil. Figure 3.1.15 shows the half-widths at half-maximum (HWHM) $v_{x1/2}$, $v_{y1/2}$, u for the intensity image of a point object. The value $d = -1$ corresponds to a full circular pupil. We see that $v_{y1/2}$ and u are virtually unchanged for small positive values of d.

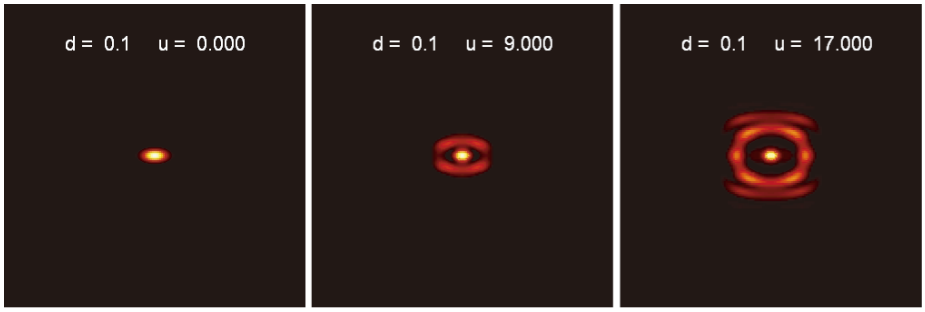

Fig. 3.1.13. The intensity point spread function for a confocal microscope with two D-shaped pupils and a point detector, $d = 0.1$.

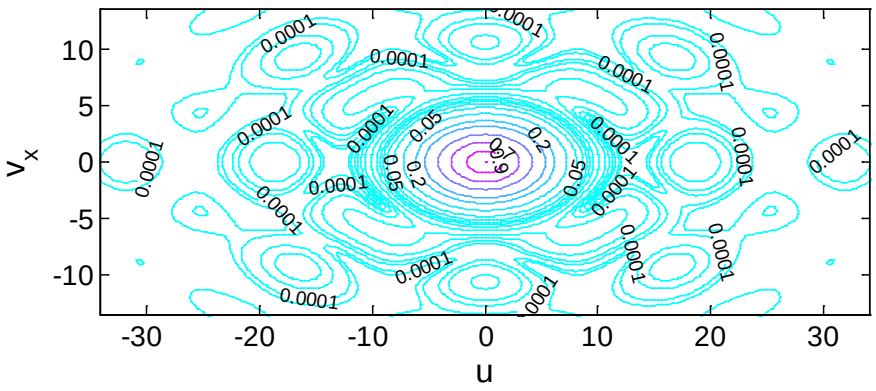

Fig. 3.1.14. Cross-section x-z through the intensity point spread function for a confocal microscope with two D-shaped pupils and a point detector, $d = 0.1$.

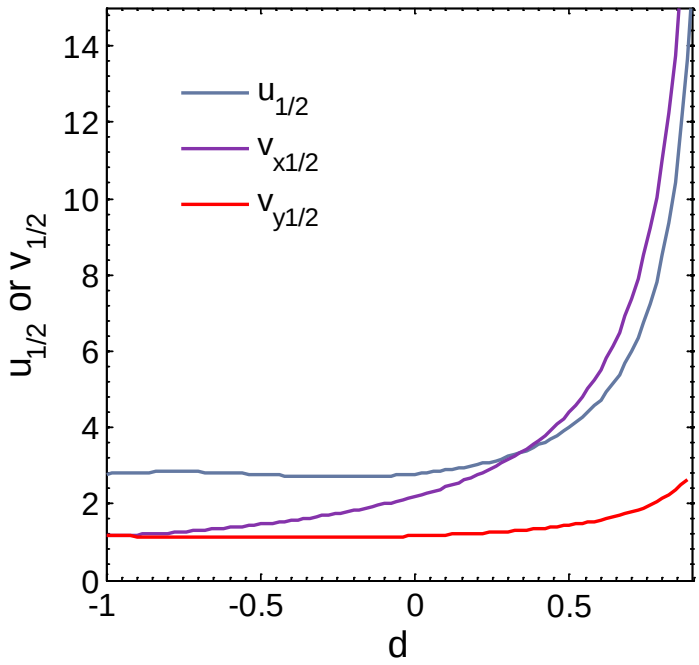

Fig. 3.1.15. Half-width at half-maximum (HWHM) of the intensity point spread function for a confocal microscope with two D-shaped pupils and a point detector in the v_x, v_y, and u directions.

The concept of integrated intensity, which is a measurement of the total power in the image, is used to describe the capability of a microscope to discriminate against parts of the object not in the focal plane [81-82]. In

confocal microscopy, this concept can be used to quantify the background produced by a scattering media. Its definition is given by

$$I_{\text{int}}(u) = \iint I(v_x, v_y, u)\, dv_x\, dv_y, \tag{3.1.22}$$

where $I(v_x, v_y, u)$ is the intensity image of an object. Figure 3.1.16 shows the integrated intensity $I_{\text{int}}(u)$ for a confocal microscope with two D-shaped pupils and a point detector as a log-log plot. For a confocal microscope with two circular pupils, $I_{\text{int}}(u)$ falls off as $1/u^2$, and for one circular and one narrow annular pupil it falls off roughly as $1/u$ [81]. For the divided aperture system, $I_{\text{int}}(u)$ falls off more quickly, for $d = 0$ as $1/u^{2.54}$, becoming close to $1/u^{3.2}$ for larger values of *d*. This demonstrates the advantage of the divided aperture technique for imaging through scattering media.

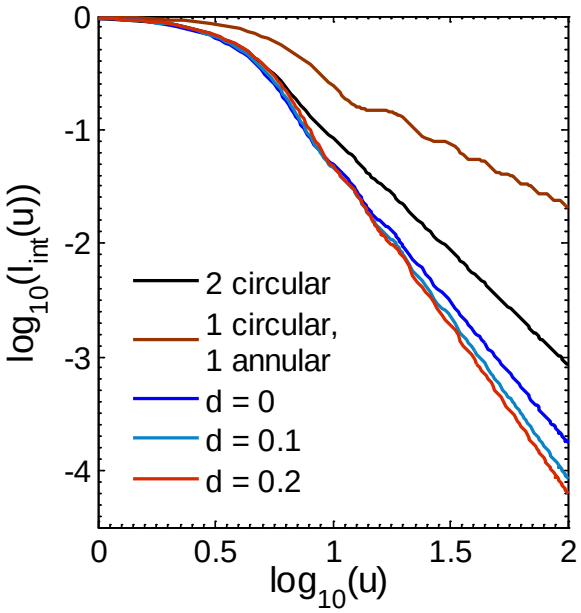

Fig. 3.1.16. The integrated intensity for a confocal microscope with two D-shaped pupils and a point detector $I_{int}(u)$ shown as a log-log plot.

The signal to background ratio is defined by $S/B = I(0,0,0)/I_{\text{volume}}$, where $I(0,0,0)$ is the intensity at the focal point and is proportional to the fourth power of the pupil area for a point detector, I_{volume} is the total contribution from single scattering by a thick scattering media given by $I_{\text{volume}} = \int I_{\text{int}}(u)du$. Note that as d increases, the area of the pupil decreases, resulting in a decreased $I(0,0,0)$. However, I_{volume} also decreases. Note that the value of S / B is independent of the absolute strength of the signal and background. Figure 3.1.17 shows the variation of S / B with d, showing that it increases monotonically with the value of d.

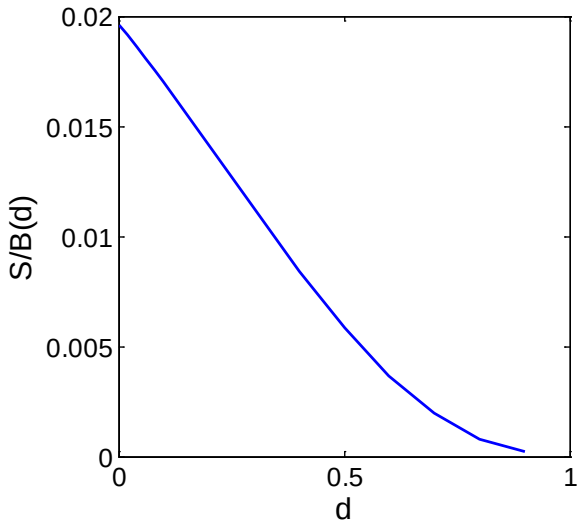

Fig. 3.1.17. Signal / Background for a confocal microscope with two D-shaped pupils and a point detector as a function of d.

The axial response from a plane reflector in a confocal microscope with two D-shaped pupils and a point detector is just the intensity along the axis for a single D-shaped pupil, compressed by a factor of two along the axis. Again the intensity falls off as $1/u^2$ for large u (>1000). For intermediate

values of *u*, again an optimum value for the absolute value of the slope of about 2.2 is achieved at $d \approx 0.07$.

The effect of using non-overlapping D-shaped pupils in a confocal microscope has been investigated. The transverse resolution in one direction, and also the axial resolution, is degraded because the pupil is smaller. If the pupils are separated by a strip of width 2*d*, as *d* increases the resolution further decreases. But there is a Poisson spot on the axis that degrades the confocal performance. As the value of *d* is increased, the rejection of out-of-focus light from scattering increases.

3.1.3 Optimization in confocal scanning microscope with D-shaped apertures

In section 3.1.1, the amplitude coherent transfer function indicates that the cutoff frequencies in both axial and transverse directions for a system with point detector are decreased by using D-shaped apertures. This is as expected, as the sizes of the pupils are decreased. However, in practice, a finite-sized pinhole is placed in front of the detector, and in practice the size of the pinhole is sometimes increased to raise the signal strength. Therefore, it is of highly practical significance to investigate the confocal system with two centro-symmetrically placed D-shaped apertures with a finite-sized detector, and to identify the optimum geometry for the pupils.

The schematic diagram for the confocal scanning microscope with two centro-symmetrically placed D-shaped apertures was illustrated in Fig 3.1.1.

For a confocal scanning microscope with two D-shaped apertures [13], the detected signal intensity for a perfectly reflecting planar object and a point source can be expressed as:

$$I(u) = \iint D(v_x, v_y) \left| h_1(v_x, v_y, u) \otimes h_2(v_x, v_y, u) \right|^2 dv_x\, dv_y, \qquad (3.1.23)$$

where $\otimes$ denotes the convolution operation, $D(v_x, v_y)$ is the intensity sensitivity of the finite-sized detector. For a circular detector, the intensity sensitivity is

$$D(v) = \begin{cases} 1, & v < v_d \\ 0, & v \geq v_d \end{cases}, \qquad (3.1.24)$$

where $v_d = 2\pi r_d a / \lambda d_0$ is the normalized radius of the pinhole, r_d is the real radius of the pinhole and d_0 is the distance between the collector and the detector. h_1 and h_2 are amplitude point spread functions given by Eq.(3.1.18).

The detected signal intensity can be reduced to:

$$I(u) = \iint D(v_x, v_y) \left| \iint P(\rho, \theta, 2u) \exp[-i(v_x \rho \cos\theta + v_y \rho \sin\theta)] \rho\, d\rho\, d\theta \right|^2 dv_x dv_y. \qquad (3.1.25)$$

The half width $u_{1/2}$, which is defined as the defocus distance at which the intensity drops to one half of the in-focus intensity [7], can be obtained as a measure of axial resolution. From the definition of the half width $u_{1/2}$, we can see that a smaller value of the half width $u_{1/2}$ indicates a better axial

resolution. For $v_d = 0$, corresponding to a point detector, the detected intensity $I(u)$ can be expressed as:

$$I(u) = \int_{d^2}^{1} \arccos\left(\frac{d}{\sqrt{\rho}}\right) \exp(iu\rho)\, d\rho. \qquad (3.1.26)$$

Figure 3.1.18(a) and 3.1.18(b) give the axial response of the intensity for $v_d = 1$ and $v_d = 6$, respectively. It can be seen that the optical sectioning

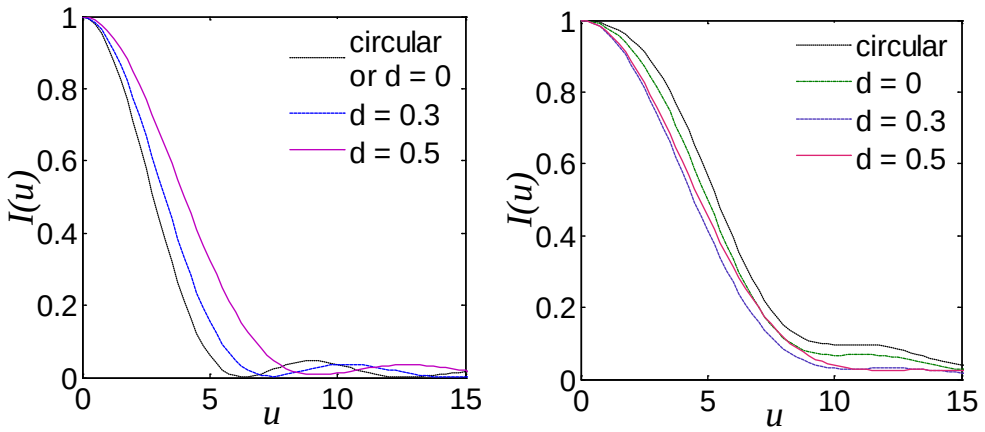

(a) (b)

Fig. 3.1.18. The axial response of the intensity with different distance parameters d, (a) when $v_d = 1$; (b) when $v_d = 6$.

effect for $d = 0$ is stronger than that for $d = 0.5$ when $v_d = 1$. However, when $v_d = 6$, for $d = 0$ it is weaker than that for $d = 0.5$. This is somewhat surprising, as usually we would expect the larger pupil to give a better axial response. The behaviour can be explained qualitatively using geometrical optics, as for the defocused case a finite-sized pinhole can be completely in the shadow region for a big enough value of d.

This property can be further illustrated in numerical plots of the half width $u_{1/2}$. Figure 3.1.19(a) illustrates the half width as a function of v_d for

a confocal microscope using D-shaped apertures with different distance parameter *d*, compared with a conventional confocal microscope with circular apertures. Although for a point detector, the confocal microscope with D-shaped apertures exhibits a poorer axial resolution than in the conventional confocal microscope with circular apertures, the behavior is different with a finite-sized detector. It is of practical significance that for a given finite-sized detector, there is an optimum configuration (value of *d*) for the confocal microscope with D-shaped apertures. Figure 3.1.19(b) shows the variation of the half width of the axial response as a function of *d* for given values of the detector radii. It can be noted that for $v_d = 0$, there is no improvements of the axial resolution for the confocal microscope with D-shaped apertures. However, for non-zero values of v_d, as *d* increases the half width of the axial response decreases until a minimum appears. Then, it increases again and eventually approaches infinity at the non-physical case of two point apertures. This indicates an optimum d_0 for the confocal system with finite-sized detector at the minimum of the half width. The dashed line in Fig. 3.1.19(b) shows the variation of the half width at the optimum point d_0 for different detector radii.

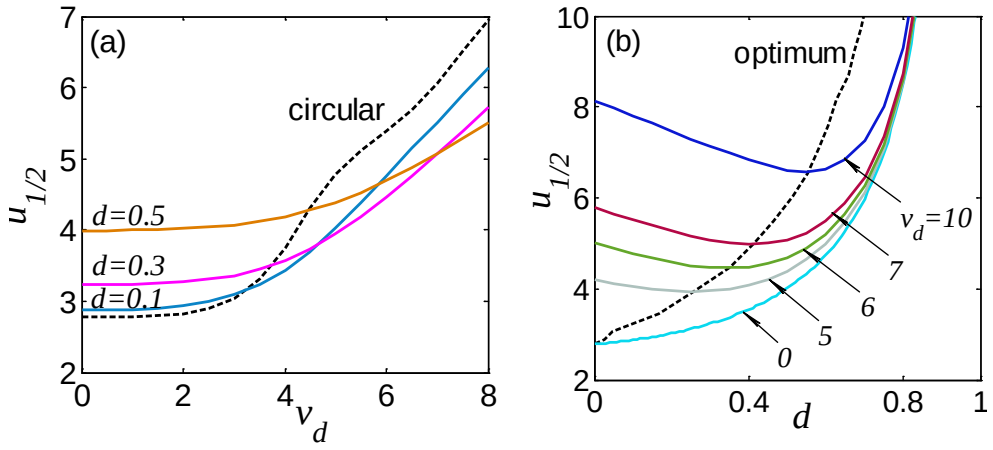

Fig. 3.1.19. The half width $u_{1/2}$ of the axial response, as a function of (a) the detector radius v_d; and (b) the distance parameter d.

Figure 3.1.20 shows the variation of the detector radius at the optimum point compared with that at the critical point d_c, where the half width is equal

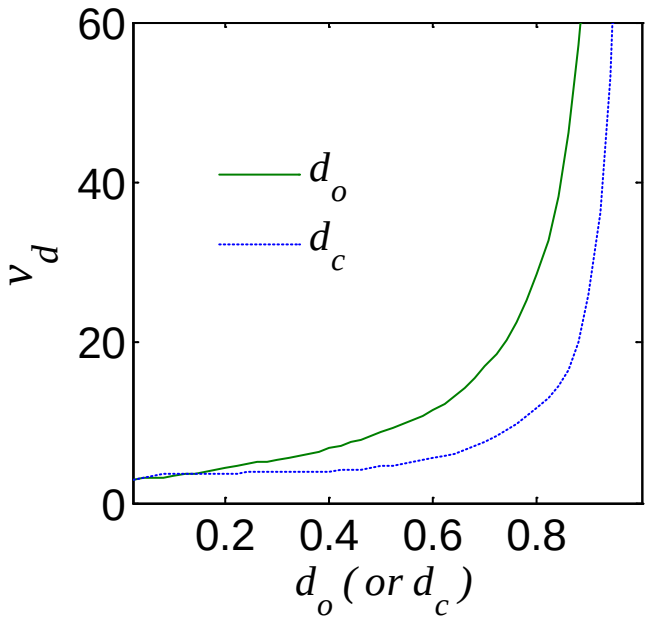

Fig. 3.1.20. The variations of the detector radius at the optimum and the critical points.

to that for circular apertures. For the region between zero and the critical point, the axial resolution is improved compared with that in a conventional confocal microscope with circular apertures. When v_d is small, d_0 and d_c

are close together and then gradually separate with increasing v_d. Eventually both of them approach infinity, as optical sectioning vanishes for large pinhole sizes. In practice, for a given value of the detector radius, an improvement in the axial resolution can be obtained by altering the distance parameter to an optimum value d_0.

From the above analysis, it is shown that the axial resolution improves only when a finite-sized detector is used. For a finite-sized detector, the detected signal strength is enhanced, but the amount of unwanted scattered light is also increased. Therefore, in order to fully understand the overall performance, it is necessary to introduce the signal level defined as the measured energy divided by that which enters the entrance pupil [85]. The detected intensity on the focal plane can be expressed as:

$$I_{u=0} = \iint D(v_x, v_y) \left| \iint P(\rho, \theta, 0) \exp[-i(v_x \rho \cos\theta + v_y \rho \sin\theta)] \rho d\rho d\theta \right|^2 dv_x dv_y. \tag{3.1.27}$$

The signal level for a given system can be given by:

$$\eta = \frac{I_{u=0}}{4\pi^2 \left(\arccos d - d\sqrt{1-d^2} \right)}, \tag{3.1.28}$$

which is normalized to unity for a large area detector. For d = -1, it reduces to the conventional confocal microscope with circular pupils, and η becomes the well-known result $\eta = 1 - J_1^2(v_d) - J_0^2(v_d)$.

Figure 3.1.21(a) illustrates the signal level as a function of detector radius v_d, with values of d of 0, 0.3, 0.5, and also for circular pupils. It is seen that for a given value of d, the signal level increases as the size of the detector increases. However, for a given radius v_d of the detector, the signal level decreases monotonically as d increases. For larger value of detector size, the signal level changes more slowly when d is small, but a much steeper curve is obtained as d increases. Figure 3.1.21(b) shows the relationship of the signal level to the half width $u_{1/2}$. At the optimum point, the signal level varying with the detector radius and the half width are shown with dashed lines in Fig. 3.1.21(a) and 3.1.21(b), respectively. The results are similar to those reported previously for a confocal microscope with annular pupil and finite sized detector [85]. Although for a given pinhole size there is an optimum value of d to minimize $u_{1/2}$, the value $d = 0$ always gives the minimum value of $u_{1/2}$ for a given η.

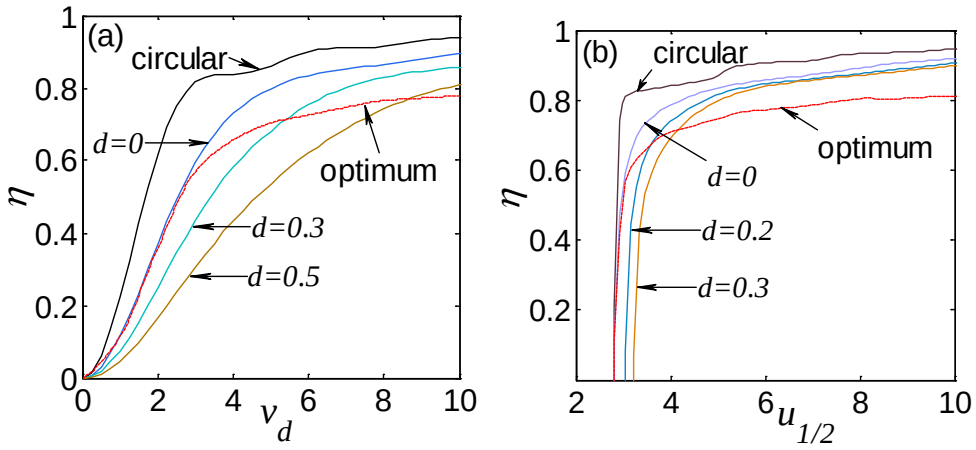

Fig. 3.1.21. The signal level, as a function of (a) the detector radius v_d; (b) the half width $u_{1/2}$.

In this section, we have theoretically analyzed the variations of the axial response as a function of the radius of the detector and distance parameter of the D-shaped aperture for the confocal microscope with D-shaped apertures. The result shows that for a given finite size of detector, by altering the distance parameter *d*, the axial resolution can be maximized, which is of practical significance in design and setting up of the microscope. For the detector size v_d less than 2.58, the optimal value of *d* is zero, for bigger v_d, the optimal value of d increases. When $v_d = 3.30$, the optimal value of d becomes 0.1.

3. 2 Diffraction analysis for incoherent imaging in fluorescence confocal scanning microscope with D-shaped apertures

3.2.1 Three-dimensional optical transfer function

In section 3.1, based on diffraction theory, we investigated the performance of a coherent confocal microscope with a divider strip of width 2*d* placed in the center of the objective aperture to separate the illumination path and the detection paths [12-13, 86-87]. The illumination and detection pupils are thus D-shaped segments of a circle. We found that: i) there is no advantage from the view of rejection of singly-scattered background in increasing *d* above a value of zero. However, the use of a non-zero value of *d*

may help to reject multiply-scattered light; ii) compared with conventional confocal microscopy, both the axial and transverse resolution are degraded for a point detector. However, the axial resolution can be improved when combined with a finite-size detector and an optimum *d* can be derived for a given finite-size detector; iii) serrated D-shaped apertures can be used to further reject the background scattering.

However, other work [88-89] has shown that fluorescence imaging has the advantage of greater specificity in cancer detection in clinical diagnosis. The divided aperture technique can be used also with a confocal fluorescence modality. In this section, we therefore propose the use of the divided aperture technique in confocal fluorescence, and extend our previous study to the performance of a system with divided D-shaped apertures (DCM), based on incoherent image formation theory. This system has potential applications in any area of fluorescence microscopy into scattering media such as tissue.

The system diagram of DCM can be found in Fig. 3.1.1. In confocal fluorescence microscopy (CM), a finite-size detector must always be selected in practice in order to increase the signal strength. The corresponding effective intensity point spread function (IPSF) for confocal single-photon fluorescence microscopy with divided apertures is

$$h(v_x, v_y, u) = |h_1(v_x, v_y, u)|^2 \left(|h_2(v_x, v_y, u)|^2 \otimes_2 D(v_x, v_y) \right), \qquad (3.2.1)$$

where $\otimes_2$ denotes the two-dimensional convolution operation. h_1 and h_2 are the amplitude point spread function given by Eq.(3.1.18). D is the the intensity sensitivity given by Eq.(3.1.24). Note that here we neglect the Stokes' shift, and thus assume that the system has equal fluorescence and incident wavelengths. In practice, the longer fluorescence wavelength may result in a small degradation of the imaging performance. The Stokes' shift for practical dyes is often around 6%.

The corresponding 3D optical transfer functions (OTF), $C(m,n,s)$, is given by the 3D Fourier transform of the 3D IPSF.

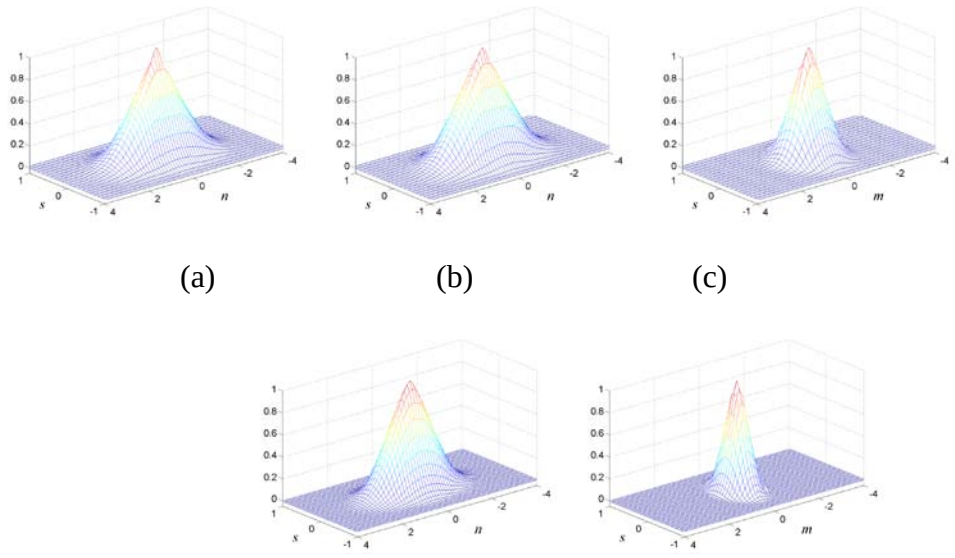

Fig. 3.2.1. 3D OTFs for confocal single-photon fluorescence microscopy with a point detector (a) $C(l,s)$ for circular apertures; (b) $C(m=0,n,s)$ for D-shaped apertures with $d=0$; (c) $C(m,n=0,s)$ for D-shaped apertures with $d=0$; (d) $C(m=0,n,s)$ for D-shaped apertures with $d=0.4$; (e) $C(m,n=0,s)$ for D-shaped apertures with $d=0.4$.

Since the D-shaped aperture is not circularly symmetrical, we consider two special cases: $C(m=0,n,s)$ and $C(m,n=0,s)$. Figure 3.2.1 shows the 3D OTFs of DCM, normalized to unity at the origin, for a point detector as a function of the divider strip width 2*d*, compared with those of CM. As the width of the obstruction *d* increases, the 3D OTF of DCM becomes, as expected, narrower in all the *m*, *n*, and *s* directions. The cross-section of the OTF in *n* direction and *s* direction are shown in Fig. 3.2.2 as a function of *d*,

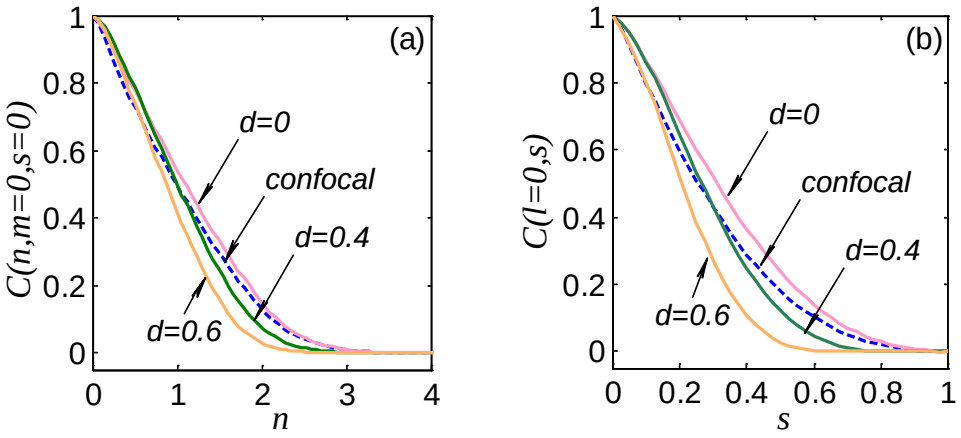

Fig. 3.2.2. Transverse (a) and axial (b) cross-section of the 3D OTF for confocal microscopy with circular apertures and D-shaped apertures with a point detector.

respectively. Compared with CM, the region in which the 3D OTF of DCM is appreciable is narrower in the *m* direction, resulting in a degraded transverse resolution in that direction. However, interestingly, for small value of *d* it becomes broader in the *n* and *s* directions, resulting in a superior response in high spatial frequencies, which implies that even for a point detector, both the transverse resolution in the *n* direction and axial resolution can be improved by selecting the value of *d*. As *d* further increases, no advantages in respect of

spatial resolution can be found. This phenomenon will be further discussed later.

In practice, the detector is not a single point but has a finite size to increase the signal strength. Figure 3.2.3 illustrates the 3D OTF of DCM with $v_d = 6$ for different values of *d*, compared with that of CM. Note that for CM a well-known missing cone of spatial frequencies appears around the origin [90]. However, as the width of the divider strip increases, this cone gradually disappears. The transverse and axial cross-sections of the 3D OTF,

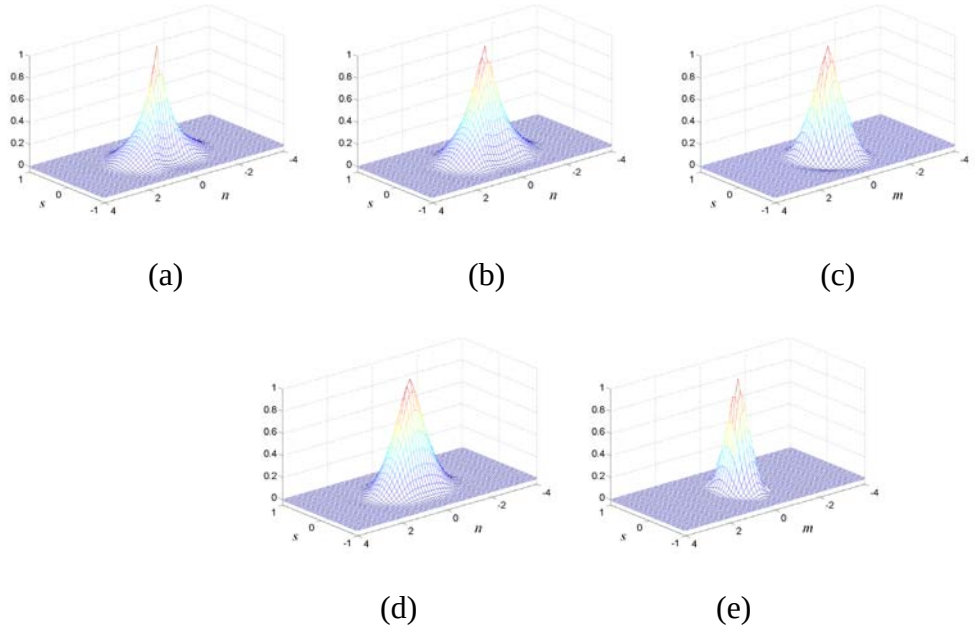

(a) (b) (c)

(d) (e)

Fig. 3.2.3. 3D OTFs for confocal one-photon fluorescence microscopy with a finite-size detector $v_d = 6$. (a) $C(l,s)$ for circular apertures; (b) $C(m=0,n,s)$ for D-shaped apertures with $d=0$; (c) $C(m,n=0,s)$ for D-shaped apertures with $d=0$; (d) $C(m=0,n,s)$ for D-shaped apertures with $d=0.4$; (e) $C(m,n=0,s)$ for D-shaped apertures with $d=0.4$.

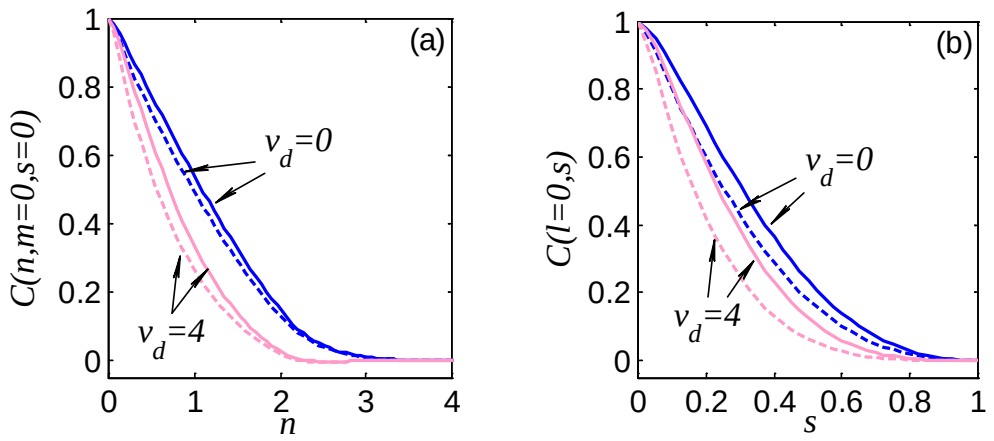

Fig. 3.2.4. Transverse and axial cross-section of the 3D OTF for CM (dash lines) and DCM with $d = 0$ (solid lines) for $v_d = 0$ and $v_d = 4$, respectively. (a) $C(n, m = 0, s = 0)$; (b) $C(l = 0, s)$.

$C(n, m = 0, s = 0)$ and $C(l = 0, s)$, normalized to unity at the origin, are respectively shown in Fig. 3.2.4, revealing their dependence on the detector radius v_d for $d = 0$. As expected, as v_d increases, $C(n, m = 0, s = 0)$ and $C(l = 0, s)$ gradually become narrower and their tails go negative due to the effects of the finite-size detector, for both CM and DCM cases. However, as a result of increasing v_d, compared with CM, for DCM case the magnitudes of the negative tails are reduced and the regions in which $C(n, m = 0, s = 0)$ and $C(l = 0, s)$ have appreciable value become broader. These properties imply that we can further improve the transverse resolution in the *n* direction and the axial resolution by using a combination of a finite-size detector and a small value of *d*.

3.2.2 Incoherent imaging and optimization in confocal scanning microscope with D-shaped apertures

One way to characterize axial resolution in confocal one-photon fluorescence microscopy is to measure the axial response of a thin fluorescent sheet [91]. This response gives the strength of optical sectioning: a sharper axial response means a higher axial resolution [92]. Consider an infinitely thin fluorescent sheet with an object function $\delta(z)$. The corresponding fluorescence image is given by the 3D Fourier transform of the 3D OTF multiplied by the spatial spectrum of the object, i.e., the 3D inverse Fourier transform of the object function. The axial response thus can be expressed as

$$I(u) = \int_{-\infty}^{\infty} C(l = 0, s) \exp(ius)\, ds. \tag{3.2.2}$$

Figure 3.2.5 illustrates the comparison of axial response between CM and DCM with various of d for the cases of $v_d = 0$ and $v_d = 4$. In section 3.1.3, we found that for DCM with the coherent imaging process, no superior axial resolution compared with CM can be obtained until v_d is larger than 2.58 [86]. However, for the fluorescence imaging, superior axial resolution can be obtained even for a point detector by selecting a small value of d. For example, when $d = 0$, the half width of half maximum (HWHM)

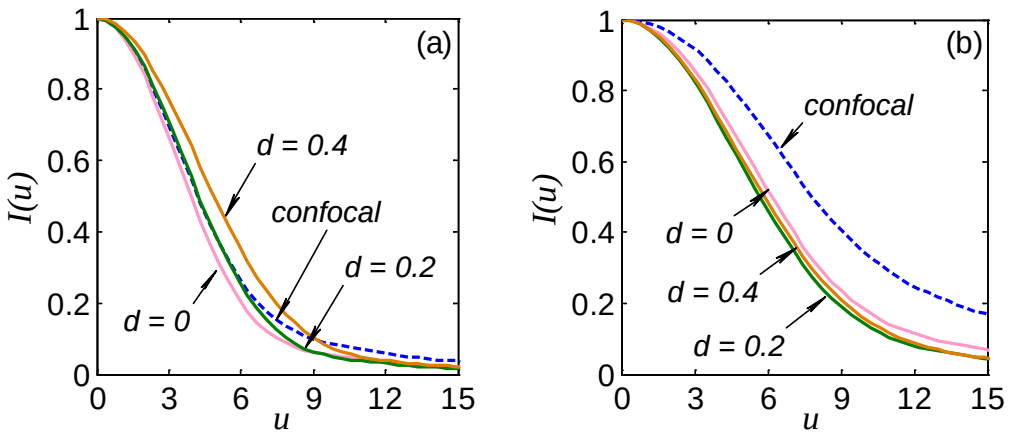

Fig. 3.2.5. Intensity of the axial response to a thin fluorescence sheet for different values of divider strip width *d* in the cases of $v_d = 0$ and $v_d = 6$.

ratio of DCM to CM is 0.93. If a finite-size detector is employed, the improvement of the axial resolution of DCM can be further enhanced (Fig 3.2.5b). For instance, given $v_d = 6$ if we choose $d = 0.2$, the HWHM ratio of DCM to CM is reduced to 0.72. For a point detector, the strength of the optical sectioning of DCM decreases as the width of the divider strip *d* increases. However, for a finite-size detector, as *d* increases, the strength of the optical sectioning first increases then decreases, indicating an optimum value of *d* for axial resolution. The optimum value of d_o having the maximum axial resolution is plotted in Fig. 3.2.6 (solid line) as a function of v_d. The critical width d_c, where the HWHM of DCM is equal to that of CM, is also plotted in Fig. 3.2.6 (solid line).

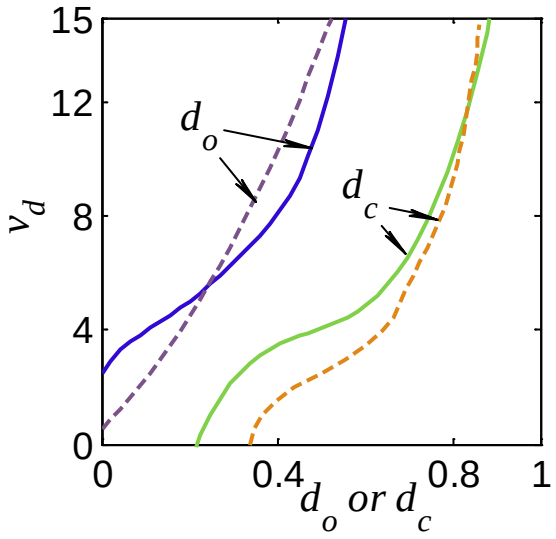

Fig. 3.2.6. Optimum and critical width of the divider strip d as a function of detector size v_d to achieve best axial resolution (solid line) or best transverse resolution (dashed line).

An alternative way to examine the axial response is to image a thick uniform fluorescence layer, sometimes called a fluorescent sea, scanned in the axial direction [93]. The corresponding object function is

$$o_f(x,y,z)=\begin{cases}1, & z\ge 0,\\ 0, & z<0.\end{cases} \tag{3.2.3}$$

Thus the axial response can be expressed as

$$\begin{aligned} I(u) &= \int_{-\infty}^{\infty} O_f(s)C(l=0,s)\exp(ius)ds \\ &= \frac{1}{2}+\frac{1}{\pi}\int_0^{\infty}\frac{C(l=0,s)\sin(us)}{s}ds. \end{aligned} \tag{3.2.4}$$

where O_f is the spatial spectrum of the object, given by 3D inverse Fourier transform of the object function. The gradient at the surface ($u=0$) of the thick layer is given by

$$I'(u=0)=\frac{1}{\pi}\int_0^{\infty} C(l=0,s)ds. \qquad (3.2.5)$$

The larger the gradient, the sharper is the image.

Figure 3.2.7 illustrates the images of a thick fluorescence layer for DCM, compared with those for CM, with various detector sizes. Note that

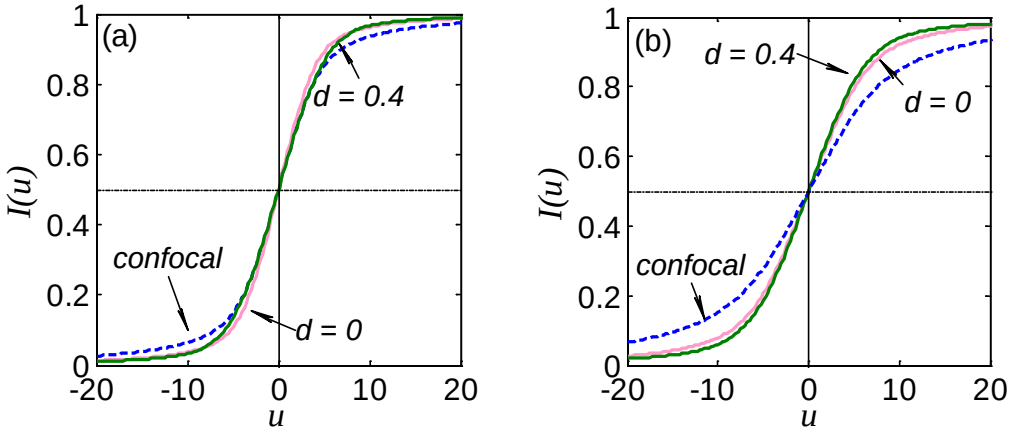

Fig. 3.2.7. Image of a thick fluorescence layer scanning in the axial direction for DCM and CM with various of detector size. (a) $v_d = 0$, (b) $v_d = 6$.

even for a point detector, a sharper axial response can be obtained if a small value of d is selected. For example, when $d = 0$, the surface gradient ratio of DCM to CM is 1.15. As v_d increases, the improvement of the axial response can be further enhanced. For example, when $v_d = 6$, the surface gradient ratio of DCM with $d = 0.4$ to CM is increased to 1.54. Note that for a finite-size detector, as d increases, the image of the layer first becomes sharper then flatter, implying an optimum value of d for each given v_d that gives the sharpest image. The above results are similar to those for the axial response for a thin fluorescence sheet, which confirms the advantages of DCM from the point of view of improving the axial resolution.

From the analysis of the 3D OTF of the DCM, we find that the cut-off frequency in the *m* direction is reduced compared with the case of CM, resulting in a degraded transverse resolution in the *x* direction. However, the region where the value of OTF is appreciable becomes broader in the *n* direction, resulting in a superior transverse resolution in *y* direction. In general, the image of a sharp edge can be used to characterize the transverse resolution of a system: the sharper the image, the better the transverse resolution [94]. Consider a thick, straight and sharp edge placed perpendicular to the divider strip, and the object function is

$$o_f(x,y,z)=\begin{cases}1, & y\geq 0,\\ 0, & y<0.\end{cases} \tag{3.2.6}$$

The corresponding image intensities of the edges in the focal plane can be derived as

$$I(v_y)=\frac{1}{2}+\frac{1}{\pi}\int_0^{\infty}\frac{C(m=0,n,s=0)\sin(v_y n)}{n}dn. \tag{3.2.7}$$

The gradient of the image at the surface ($v_y=0$) is given by

$$I'(v_y=0)=\frac{1}{\pi}\int_0^{\infty}C(m=0,n,s=0)dn. \tag{3.2.8}$$

Figure 3.2.8(a) shows the images of a thick, straight and sharp edge for CM and DCM with different values of *d* and v_y, respectively. Interestingly,

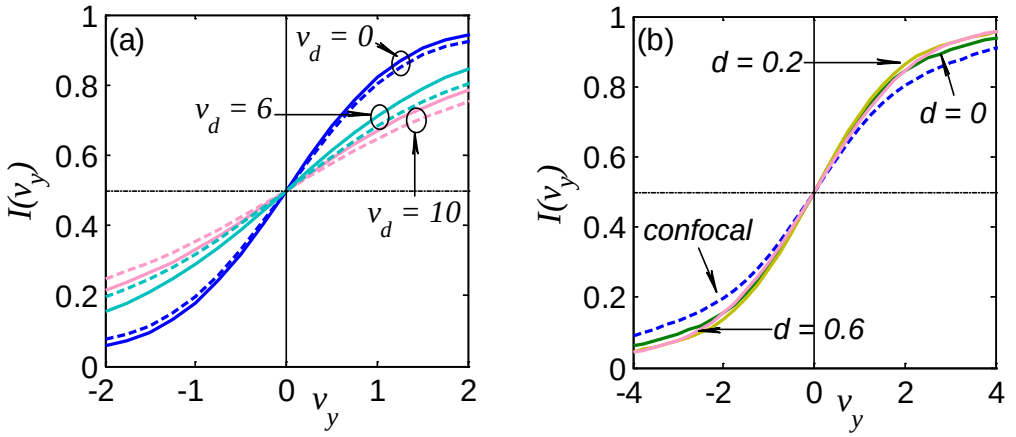

Fig. 3.2.8. Images of a thick, straight and sharp edge placed perpendicular to the divided strip for CM (dash lines) and DCM (solid lines), respectively: (a) given $d = 0$, but with different values of detector size v_d; (b) given $v_d = 6$, but with different values of the width of the divider strip *d*.

compared with CM, a sharper image can also be obtained by DCM for a point detector. For instance, if we choose $d = 0$, the image gradient ratio at the surface of DCM to CM is 1.06. As the detector size increases, the improvement is further enhanced. For example, when $v_y = 6$, if we select $d = 0.2$, the gradient ratio of DCM to CM increases to1.21. This result can be expected from the transverse cross-section of 3D OTF in Fig. 3.2.4(a). For a point detector, as the width of the divider strip *d* increases, the sharpness of the image reduces. However, for a finite-size detector, as *d* increases, the sharpness of the image first increases then decreases (Fig. 3.2.8(b)), resulting in an optimum value of *d* to achieve the sharpest image in *y* direction, i.e. the highest transverse resolution. Figure 3.2.6 (dash lines) illustrates the optimum value d_o and the critical value d_c (where given the same detector size the gradient of the image of DCM at the surface is equal to that of CM), as a function of detector size v_d, respectively.

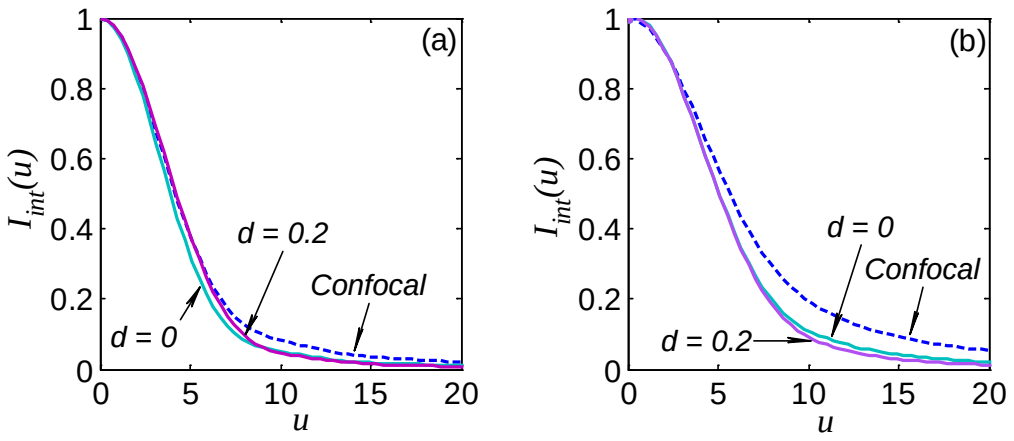

Fig. 3.2.9. Integrated intensities of CM (solid lines) and DCM (dash lines) for (a) $v_d = 0$, and (b) $v_d = 4$, respectively.

Figure 3.2.9 illustrates the integrated intensity of a point object, given by Eq.(3.1.22), for CM and DCM with various values of detector size. It is shown that for a point object with a point detector, $I_{\text{int}}(u)$ falls quickest for DCM with $d = 0$ in the region of small values of *u*. As *d* increases, $I_{\text{int}}(u)$ becomes gradually broader, and eventually broader than the case for CM. For larger values of *u*, $I_{\text{int}}(u)$ for CM falls off according to an inverse-square law. However, $I_{\text{int}}(u)$ for DCM falls off more quickly, for $d = 0$ as $1/u^{2.53}$, becoming close to $1/u^{3.2}$ for larger values of *d* [12]. For a finite-size detector, in the region of small values of *u*, as *d* increases the rate of decay of $I_{\text{int}}(u)$ for DCM first increases then decreases, leading to an optimum value of *d* to achieve the maximum rate of decay. However, for larger values of *u*, the rate of decay of $I_{\text{int}}(u)$ for DCM increases as *d* increases. For instance, when $v_d = 4$, $I_{\text{int}}(u)$ for DCM falls off for $d = 0$ as $1/u^{2.33}$, becoming close to $1/u^{2.5}$ for $d = 0.2$, compared with $1/u^{1.9}$ for CM. The fast decay of the

integrated intensity demonstrates the advantage of the divided aperture technique in imaging through scattering media.

Figure 3.2.10 shows S / B in CM and DCM as a function of d. For a given detector size v_d, as d increases, S/B reduces monotonically. For a given value of d, S/B reduces monotonically as v_d increases. This property means that there is no advantage from the point of view of single-scattering background rejection in increasing v_d and d above a value of zero. However it may be helpful in rejection of multi-scattering background. Similar results have been obtained for coherent confocal microscopy with D-shaped apertures [13].

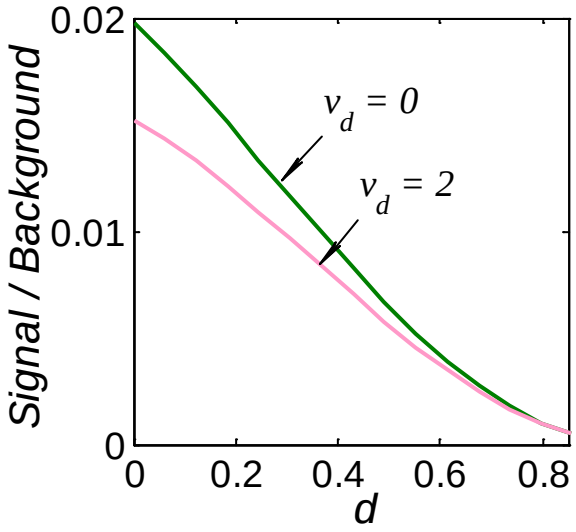

Fig. 3.2.10. Signal to background ratio S/B as a function of the width of divider strip d for various values of detector size v_d.

The performance of confocal single-photon fluorescence microscopy with non-overlapping D-shaped apertures has been investigated. The 3D IPSF is given. If the pupil is separated by a divider strip with width 2d, the

transverse resolution in the *n* direction and the axial resolution can be improved by selecting the value of *d*. For a given finite-size detector, as the value of *d* increases, both the transverse and axial resolutions first increase then decease, resulting in an optimum value of *d* (Fig. 3.2.6) to achieve the maximum transverse or axial resolution. The capability of rejection of the single-scattering background is reduced as the value of *d* increases, and further degraded as the detector size increases.

This modification of the confocal fluorescence microscope offers improved imaging performance for imaging into scattering media, with applications in clinical diagnosis, small animal imaging, and also basic studies such as developmental biology.

3. 3 Improvements in confocal microscopy imaging using serrated divided apertures

The angular gating mechanism, which uses the divided aperture technique, combines different beam paths for illumination and detection together with confocal imaging, so that the illumination and detection beam paths cross only in the focal region. Then light scattered other than in the focal plane is further rejected by the confocal pinhole (or slit) [8-9]. In divided aperture microscopy, most published work has focused on two D-shaped apertures (segments of circles), one each for illumination and detection,

respectively [9-11, 13]. In section 3.1 and 3.2, we analyzed imaging in such a system based on diffraction optics. The results show that the angular gating technique can enhance the efficiency of rejecting scattering light. However, it is interesting to note that a central bright spot exists even far from the focal plane. This out-of-focus central bright spot, analogous to the Poisson spot, allows overlapping of the illumination and detection regions, affecting imaging quality and contrast.

This section describes weakening the strength of the out-of-focus central bright spot with the use of serrated apertures [95-98], thus further increasing the efficiency of the angular gating technique. Consider a reflective-mode confocal microscope with divided serrated-apertures of mean radius a_0, which is illustrated in Fig. 3.3.1. A suitable scanning system has

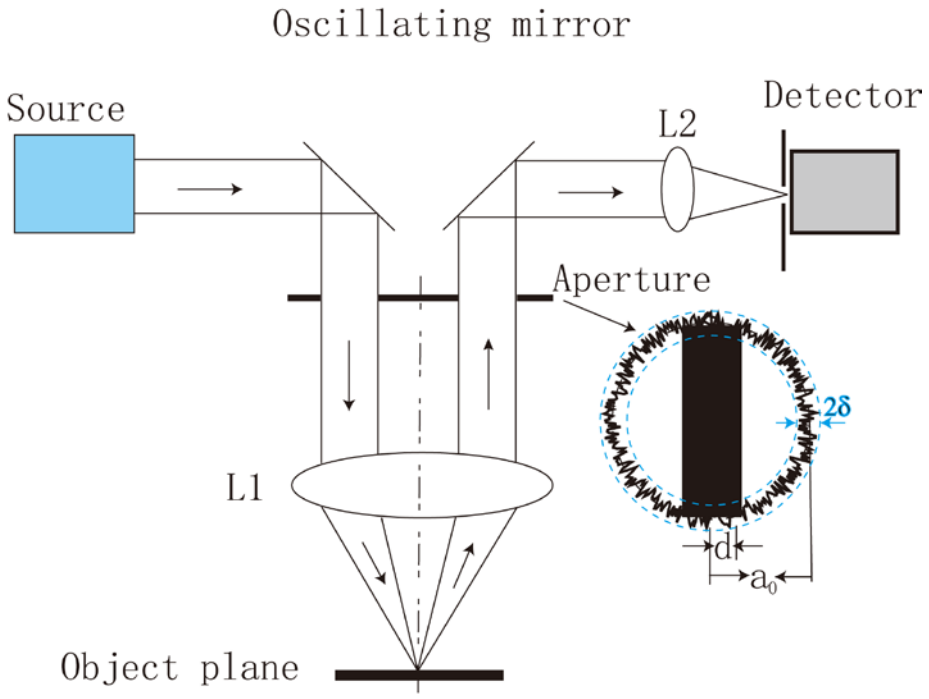

Fig. 3.3.1 Schematic diagram of the confocal optical system with serrated divided apertures.

been described by Koester [8]. The radius of the serrated-aperture is given by $r = a_0(1+\sigma)$, where σ is a random variable. Since the actual distribution function of σ does not affect the results much, we choose a uniform distribution function between $\pm\delta$. A divider strip of width 2*d* is placed in the center of the objective aperture to separate the illumination path and the detection path.

Using D-shaped apertures increases the rejection of out-of-focus light, since the illumination and the detection paths only overlap on the focal plane. However, from section 3.1.2, we understand that due to the diffraction by the apertures, there is a central bright spot out of the focal region caused by the coherent summation of rays from the circular edge. Therefore, we introduce serrated apertures to weaken the strength of the out-of-focus central bright

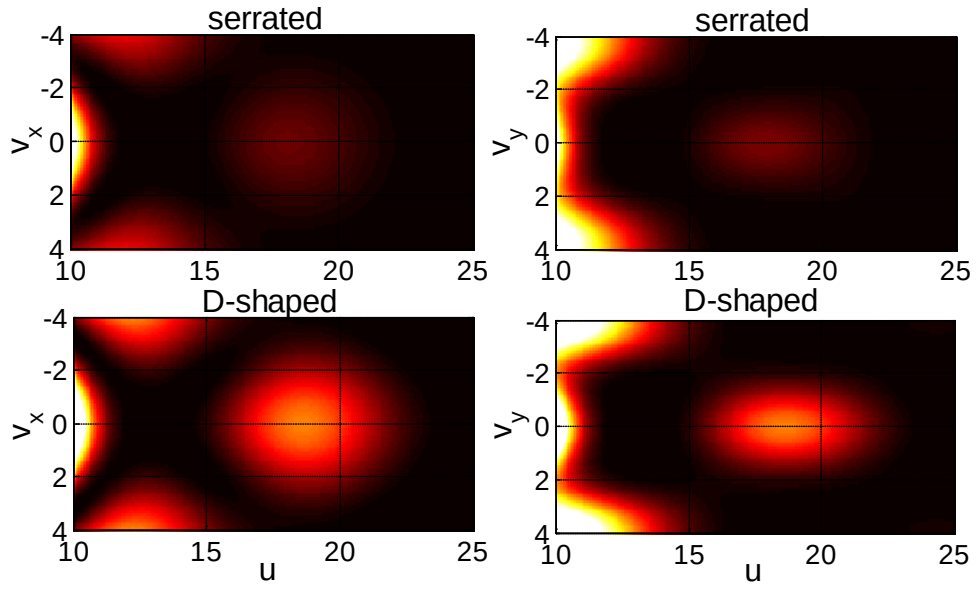

Fig. 3.3.2. The intensity point spread function of confocal system with serrated divided apertures and D-shaped apertures, for v_x-*u* section and v_y-*u* section, when $d = 0.1$ and $\delta = 0.1$.

spot. Fig. 3.3.2 illustrates the IPSF of the serrated divided apertures, compared with the D-shaped apertures. At the focal point, the IPSFs for the serrated apertures case and the D-shaped apertures case have the same value, since the intensity at the focal point is proportional to the fourth power of the area of the pupils. However, it can be seen that the serrated divided apertures dramatically weaken the strength of the out-of-focus central bright spot. For example, when $u = 20$, the intensity of central spot for serrated divided apertures case is reduce to 24% of that for D-shaped apertures case. That is because the centers of curvature of the aperture edges are identical for the D-shaped apertures, while randomly varying for the serrated apertures.

To further understand the imaging performance, Fig. 3.3.3 shows the half width half maximum (HWHM) of the axial response $u_{1/2}$ and the HWHM of the transverse intensity $v_{x1/2}$ and $v_{y1/2}$ of the confocal system with divided serrated apertures, compared with that for D-shaped apertures. Note that the $u_{1/2}$ becomes smaller before becoming larger as d increases for finite size pinhole, which shows that for a given detector pinhole size we can choose the value of d to optimize the axial resolution. It can be observed that the HWHM of the axial response of the system with serrated apertures is nearly the same as that with D-shaped apertures for various detector sizes v_d. However, the HWHM of transverse intensity of the system with serrated apertures is smaller than that with D-shaped apertures as v_d increases. This indicates that the axial resolution is nearly maintained, while the transverse resolution is

obviously improved for larger v_d. In addition, in the log-log plot of the axial intensity from a plane reflecting object shown in Fig. 3.3.4, it is seen that the intensity of the system with serrated apertures decays faster than that with D-shaped apertures (see the dashed lines). This is because that the energy in the side lobes for the serrated apertures reduces faster than the D-shaped apertures, which can be confirmed by the intensity point spread function shown in Fig. 3.3.2(a) for the $v_y = 0$ plane and Fig. 3.3.2(b) for the $v_x = 0$ plane. This phenomenon has practical significance, because more scattered light outside the focal region is rejected, meanwhile that in the focal region remains, allowing better imaging quality and contrast.

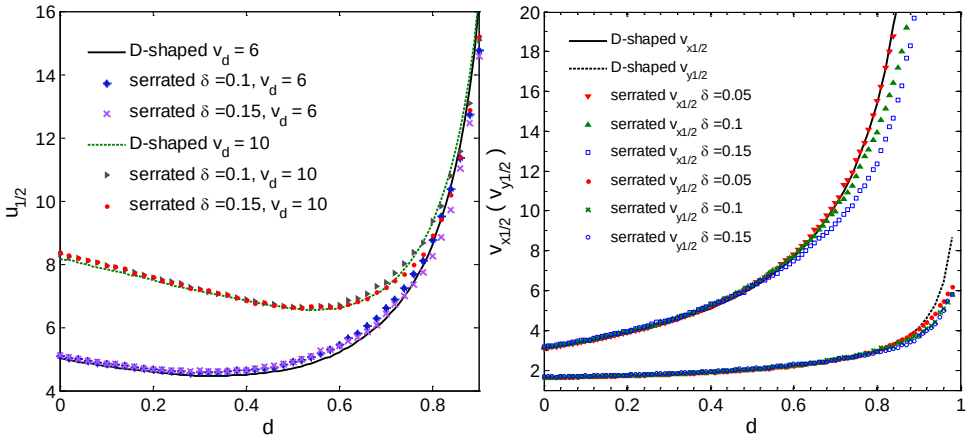

Fig. 3.3.3 (a) HWHM of the axial response for a perfect planar object, $u_{1/2}$, as a function of d for $\delta = 0.1$ and $\delta = 0.15$ when $v_d = 6$ and $v_d = 10$. (b) HWHM of the transverse intensity, $v_{x1/2}$ and $v_{y1/2}$, when $u = 0$ as a function of d with $\delta = 0.05$, 0.1 and 0.15, respectively.

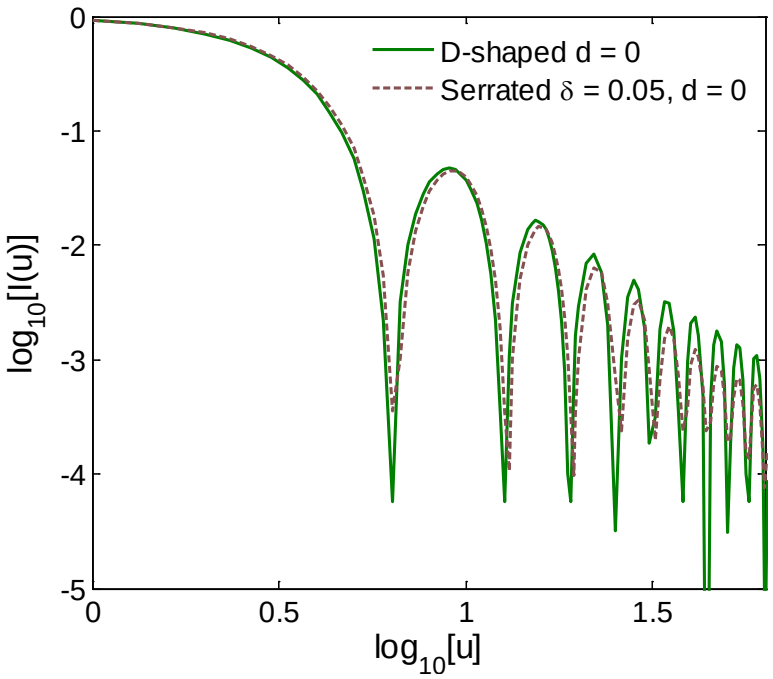

Fig. 3.3.4 Axial response $I(u)$ to a perfect reflector for point detector when d = 0.

Fig. 3.3.5 shows a comparison of S/B between confocal microscope with serrated divided apertures and D-shaped apertures. It can be seen that S/B decreases monotonically with the value of d, which means no improvements from the point of view of rejection of singly-scattered background in increasing d above a value of zero [12]. However, use of a non-zero value of d may help in rejected multiply scattered light. For a given d, S/B for the serrated divided apertures is higher than for D-shaped apertures. This confirms that the serrated apertures can reduce the effects of disturbances from out-of-focal region, thus enhancing the imaging quality.

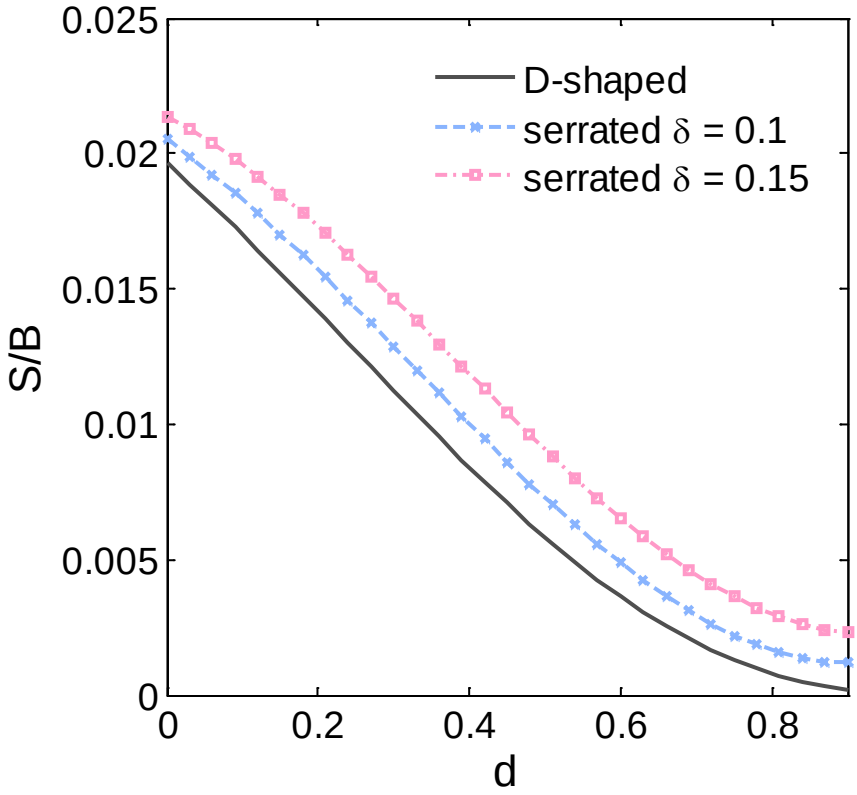

Fig. 3.3.5 Signal to background ratio, *S/B*, as a function of *d* for $\delta = 0.1$ and $\delta = 0.15$, respectively.

In this section, we have introduced a modified confocal microscopy with serrated divided apertures. The technique has practical significance, since the out-of-focus central bright spot, which affects the image performance, is greatly reduced; while the resolution is maintained. In addition, the signal to background ratio, which indicates an increased efficiency of the rejection of scattered light, is also improved. Finally, this approach could also be applied to the related technique of focal modulation microscopy (FMM) [16].

Chapter 4 Focal modulation microscopy

4. 1 Focal modulation microscopy with D-shaped apertures

4.1.1 Image formation in focal modulation microscopy

Confocal fluorescence microscopy has been used successfully to distinguish cancer cells rapidly and noninvasively from surrounding tissues [100-101]. In confocal microscopy, a pinhole or single-mode fiber is used to reject out-of-focus light scattered by the tissue. However, the selective detection mechanism is not so effective when the focal point moves deep into the tissue, when multiple scattering dominates over ballistic scattering [6]. More recently, our group has developed a modified confocal microscopy technique, which we call focal modulation microscopy (FMM) [16, 102-105], to effectively reject the multiply scattered photons. FMM can simultaneously

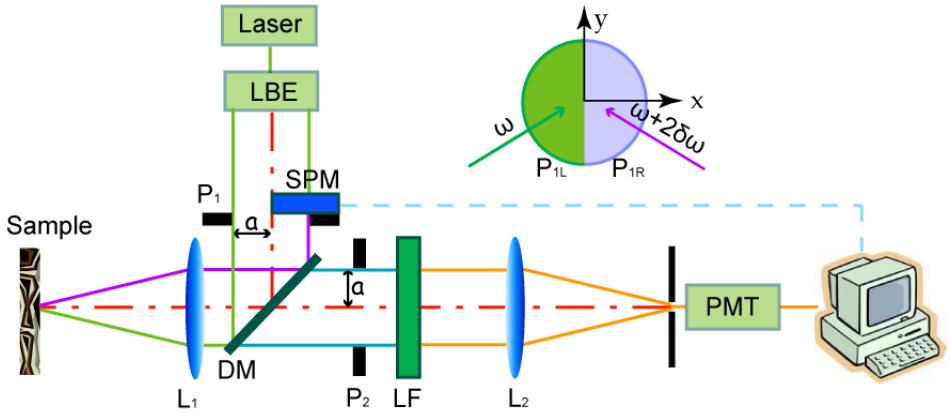

Fig. 4.1.1. Schematic diagram of the focal modulation microscope. LBE: laser beam expander. SPM: spatial phase modulator. DM: dichroic mirror. LF: long-pass filter. PMT: photomultiplier tube. L_1: objective lens. L_2: collection lens.

acquire conventional confocal images and FMM images. Experimental results for chicken cartilage show that the imaging depth of FMM can be extended to around 600 μm. Compared with conventional confocal microscopy, which is usually performed at an imaging depth up to a few tens of microns for subcellular imaging, our FMM system exhibits a substantial improvement.

Figure 4.1.1 illustrates a schematic diagram of our prototype experimental setup. Illumination is by a solid state single frequency laser at a wavelength of 640 nm. The expanded beam is split into two spatially separated half-beams, and only one half-beam passes through a spatial phase modulator, which causes the two half-beams to have a relative frequency shift. After focusing by the objective lens, the two half-beams interfere to produce an illuminating pattern that moves relative to the focal point, as a result of the relative phase between the beams. A modulation of the illumination intensity is achieved only around the focal region, generating a modulated fluorescence signal. Before the collected light enters the detector, a long pass filter is used to reject the excitation light, and finally, the detected modulated signal is analyzed using demodulation and lock-in techniques. Only the ballistic photons contribute to modulated excitation intensity as they have well defined phase and polarization, so that the scattered light is filtered out. FMM can be performed with various different geometries for the two illuminating beams, which must originate from non-overlapping apertures in the front focal plane of the objective.

For a better understanding of the operation of FMM, we first study the three dimensional (3D) intensity image of a point object. To simplify the simulation, we assume that the incident light and the emitted fluorescence light have the same wavelength, i.e. we neglect the Stokes' shift, which may result in a further degradation of the 3D image. The corresponding 3D image of a point object with a finite size detector is given by:

$$I(v_x, v_y, u, t) = \left| h_{1A}(v_x, v_y, u) + h_{1B}(v_x, v_y, u) e^{i2\delta\omega t} \right|^2 \left(\left| h_2(v_x, v_y, u) \right|^2 \otimes_2 D(v_x, v_y) \right), \tag{4.1.1}$$

where $2\delta\omega t$ is the instantaneous relative phase shift of the two half-beams, $h_{1A}(v_x, v_y, u)$ and $h_{1B}(v_x, v_y, u)$ are the 3D amplitude point spread functions (APSF) of the left and right half objective lenses (Fig. 4.1.1), respectively, and $h_2(v_x, v_y, u)$ is the APSF of the collection lens. Their definitions can be found in Eq. 3.1.18.

After passing through a lock-in amplifier, we can extract four signals: the DC signal I_{DC}, the modulation signal I_{mod}, and, by using a reference signal, the in-phase component I_{ip} and quadrature component I_{qu}. These are given by:

$$I_{DC} = \left(\left| h_{1A} \right|^2 + \left| h_{1B} \right|^2 \right) \left(\left| h_2 \right|^2 \otimes_2 D \right), \tag{4.1.2}$$

$$I_{\mathrm{mod}} = \left| h_{1A} h_{1B}^* \right| \left(\left| h_2 \right|^2 \otimes_2 D \right), \tag{4.1.3}$$

$$I_{ip} = \left(h_{1A} h_{1B}^* + h_{1A}^* h_{1B} \right) \left(\left| h_2 \right|^2 \otimes_2 D \right), \tag{4.1.4}$$

$$I_{qu} = \left(h_{1A}h_{1B}^{*} - h_{1A}^{*}h_{1B}\right)\left(\left|h_2\right|^2 \otimes_2 D\right). \qquad (4.1.5)$$

Fig. 4.1.2 illustrates contour plots of the image of a point object for the case of a point detector, normalized to unity at the focal point $I(0,0,0)$, for

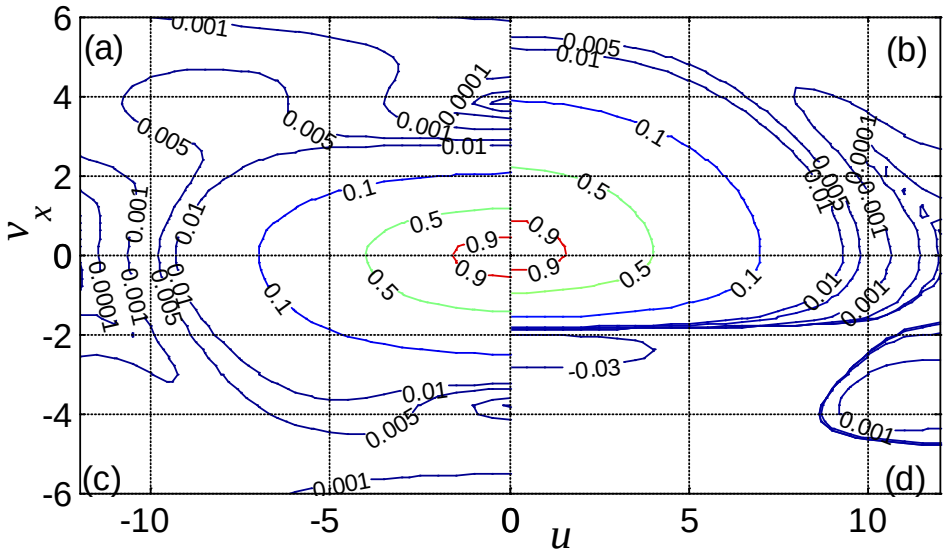

Fig. 4.1.2. The intensity image of a point object with a point detector, for (a) confocal microscope with two identical circular lenses; (b) confocal microscope with divided apertures (D-shaped apertures); (c) modulation signal in FMM ; and (d) in-phase signal in FMM. For (a), (b) and (d) this represents the intensity point spread function IPSF.

the modulation signal and the in phase-signal, compared with confocal microscopy using either circular apertures or D-shaped apertures. We compare these in the $v_y = 0$ plane only since they behave exactly the same as each other in the $v_x = 0$ plane. This is understandable, because in the *y* direction of the incident pupil space there is no phase change in FMM. From Fig. 4.1.2, it can be seen that the image for the modulated signal in FMM is narrower in the transverse direction than for the confocal microscope with D-shaped pupils, but broader than for confocal microscope with circular pupils. Because of the

nonlinear form of Eq. 4.1.3, image formation for the modulated signal in FMM is not linear in intensity, and hence the image of a point object cannot be regarded as an intensity point spread function (IPSF). However, for the in-phase signal, IPFMM, there is an IPSF, equal to the image of a point object, and this converges to a narrower transverse region than those for either confocal microscopy or the modulation signal in FMM. The half width at half maximum (HWHM) of the IPSF for IPFMM is improved by 16.4% compared with the confocal case, whereas the D-shaped case is degraded by 89.1%, as might be expected from the smaller pupil. This phenomenon shows that using the in-phase signal of FMM, an improved spatial resolution can be obtained. Moreover, as the detector size increases, the IPSF is only slightly degraded. The IPSF for IPFMM exhibits values that can be slightly negative, and these negative values increase for larger pinhole sizes. When v_d is approximately less than 2, the IPSF is similar to the point detector case. The resolution improvement of IPFMM can be understood as an example of two-pupil synthesis [106], which is a general method for generating an optical transfer function that is not an autocorrelation, thus increasing the relative strength of higher spatial frequencies.

Fig. 4.1.3 illustrates a log-log plot of the integrated intensities for IPFMM, compared with the confocal microscopy with circular apertures and with D-shaped apertures for a point detector. It can be seen that near the focal plane the integrated intensity of IPFMM has a narrower main lobe than for

confocal microscopy. More importantly, IPFMM has the sharpest slope in the log-log plot, increased from 2 to 2.9, which indicates that the background decays more quickly with distance from the focal plane. Background scattering can be described by the integrated intensity over a featureless volume, which is calculated as 5.31, 4.60, and 4.42 for the confocal, D-shaped, and IPFMM cases, respectively. The behavior of the integrated intensity does not change appreciably for non-zero, but small, pinhole sizes. The signal to background ratio (S/B) is defined as the ratio between the signal at the focal point $I(0,0,0)$ and the background scattering [12]. Note that the value of S/B is independent of the absolute strength of the signal and background, and the signal is proportional to the fourth power of the area of the pupils. The S/B is 0.032, 0.02, and 0.048 for the confocal, D-shaped, and IPFMM cases, respectively, indicating an improvement for IPFMM. Moreover, compared with confocal, the improvement of IPFMM is further increased when a finite size pinhole is used, from 50% for $v_d = 0$, to 81.6% for $v_d = 2$.

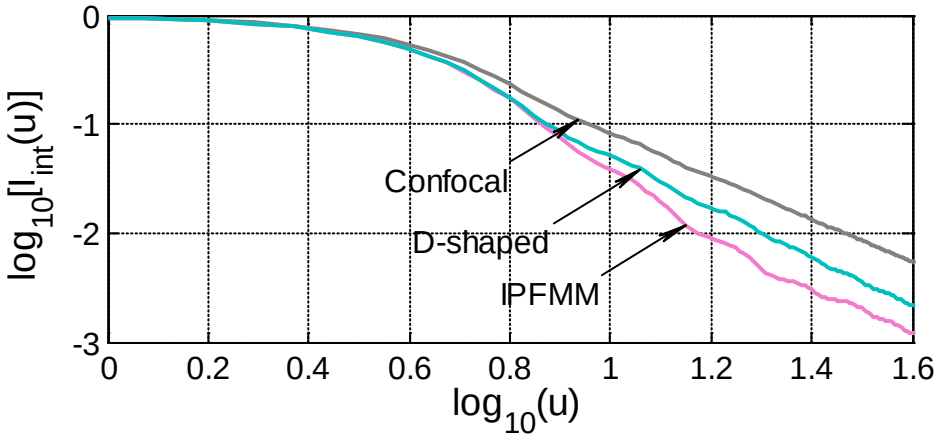

Fig. 4.1.3. The variations of the integrated intensity of IPFMM, compared with the conventional confocal microscope with circular apertures and with D-shaped apertures, for a point detector.

The superior image performance of FMM has a simple explanation. In the FMM case, only the ballistic photons in the focal region can be detected due to their well-defined phase and polarization. However, in confocal microscopy, some ballistic photons scattered from the vicinity of the focal plane can still be collected by the detector through the pinhole. Thus the spatial filtering effect using only a pinhole in confocal microscopy is not as effective as in FMM, where the spatial filtering effect is enhanced by a phase modulator. Moreover, detection of the in-phase signal IPFMM, instead of the modulation signal, gives better spatial resolution and deeper penetration depth, making it promising for *in vivo* imaging. In practice, the use of a lock-in amplifier can further enhance noise rejection by reducing noise components that do not fall on the modulation frequency.

FMM can also be performed in a saturated fluorescence mode [107-108] to provide in principle further unlimited increase in resolution. The geometry of FMM, using two beams with a relative frequency shift to result in intensity modulation, coupled with detection using lock-in techniques, is compatible with the technique recently described by Fujita et al.[46], where a time-harmonic fluorescence signal is generated by fluorescence saturation. This method, called saturated excitation microscopy (SAX), can be combined with IPFMM to obtain further improvements in spatial resolution coupled with increased depth penetration. The fluorescence signal obtained by harmonic demodulation at the frequency of $n\omega$ (n = 2,3…) is proportional to the nth

power of the excitation intensity when excitation is low enough that the harmonic power is not saturated. Therefore, the effective IPSF for IPFMM with saturated excitation, demodulated at the frequency of $n\omega$, is given by:

$$I_{ip} = \left(h_{1A} h_{1B}^{*} + h_{1A}^{*} h_{1B} \right)^{n} \left(\left| h_2 \right|^2 \otimes_2 D \right). \tag{4.1.6}$$

Fig. 4.1.4 shows profiles of the IPSFs in the lateral (v_x) direction at various demodulation frequencies for SAX, and IPFMM combined with SAX, respectively. It should be pointed out that the IPSF of IPFMM has side lobes with small negative values. As the order of the demodulation frequency increases, the magnitude of the negative components is drastically reduced. Thus the imaging artifacts caused by the negative components are negligible. The HWHM for SAX at demodulation frequencies ω, 2ω, 4ω, an 8ω are 1.16, 0.95, 0.74, and 0.55, respectively. However, when IPFMM is combined with SAX, the HWHMs at demodulation frequencies ω, 2ω, 4ω, and 8ω are reduced to 0.97, 0.77, 0.58, and 0.43, respectively. Compared with confocal microscope, the HWHMs of IPFMM combined with SAX can be improved by 16.4%, 33.6%, 50.0%, and 62.9% at demodulation frequencies ω, 2ω, 4ω, and 8ω, respectively. Note that the spatial resolution of SAX is not limited by fundamental effects, but rather by the S/N, the dynamic-range of the detection system and the nonlinearity incoherent in the light illumination. When the order of demodulation increases, not only does the S/N becomes dramatically degraded but also a strong excitation intensity is

required, thus giving rise to stronger photobleaching effects. However, if we combine SAX with IPFMM, we can reduce the order of demodulation frequency but retain the spatial resolution. For example, we can utilize 2nd-harmonic frequency (2ω) to obtain a spatial resolution which needs fourth-harmonic frequency (4ω) by SAX alone, making SAX more promising for observations of biological phenomena *in vivo*.

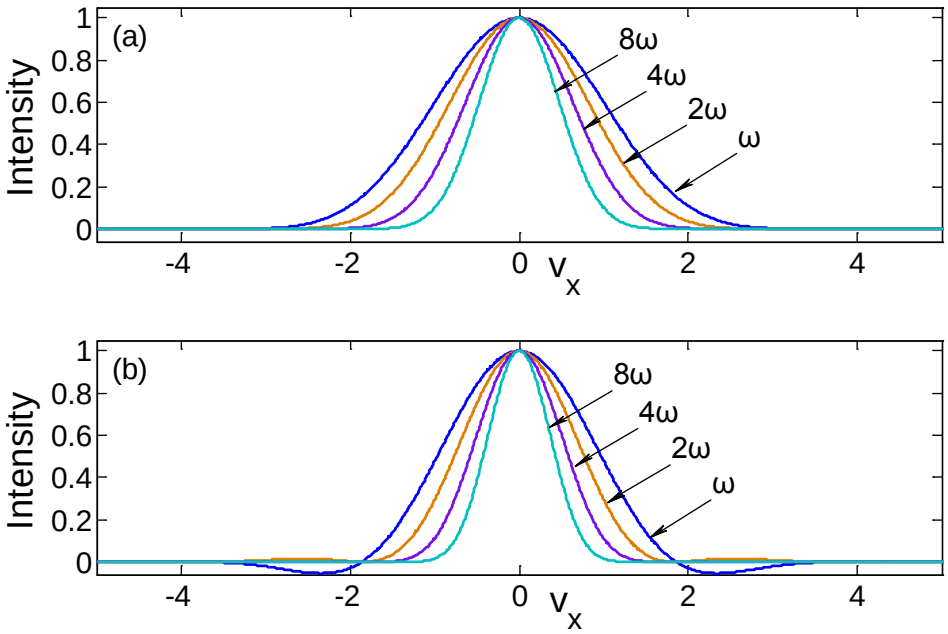

Fig. 4.1.4. PSFs of (a) saturated fluorescence microscopy, and (b) IPFMM combined with saturated excitation of fluorescence, for demodulation frequencies ω, 2ω, 4ω, and 8ω, respectively.

In conclusion, we have demonstrated that improved spatial resolution can be obtained by a standard optical setup for confocal fluorescence microscopy equipped with a spatial phase modulator and a lock-in detection system. It is also possible to combine this technique with SAX, which gives superresolution (i.e. spatial bandwidth increased beyond the classical limit), to

reduce the order of demodulation frequency while maintaining the spatial resolution.

4. 1.2 Edge enhancement for in-phase focal modulation microscopy

In this section, in terms of the three-dimensional (3D) optical transfer function (OTF), we further investigate images of a straight edge to show the improvement of transverse resolution in FMM. An image of straight edge shows an aspect of the two-dimensional imaging capability of an optical system. In general, a sharper edge image means a better transverse resolution [109].

The 3-D OTF $C(m,n,s)$ for the IPFMM is given by the 3D Fourier transformation of its IPSF, expressed as:

$$C(m,n,s) = F_3[I_{ip}], \tag{4.1.7}$$

where F_3 denotes the 3D Fourier transformation. For a point detector, the 3D OTF can be reduced to:

$$C(m,n,s) = F_3\left[\left(h_{1A}h_{1B}^{*} + h_{1A}^{*}h_{1B}\right)\left|h_2\right|^2\right], \tag{4.1.8}$$

Consider the special case when half of the objective pupil is covered by the phase modulator. Therefore, h_{1A} and h_{1B} are APSFs of the semi-circular objective pupil, and have the symmetric relationship that $h_{1b}(v_x, v_y, u) = h_{1a}(-v_x, -v_y, u)$. Figure 4.1.5 illustrates the 3D OTF of IPFMM with symmetric semi-circular objective pupils, normalized to unity at the

origin, for different values of detector size. For a point detector, the transverse and axial normalized cut-off spatial frequencies are 4 and 1, respectively. As

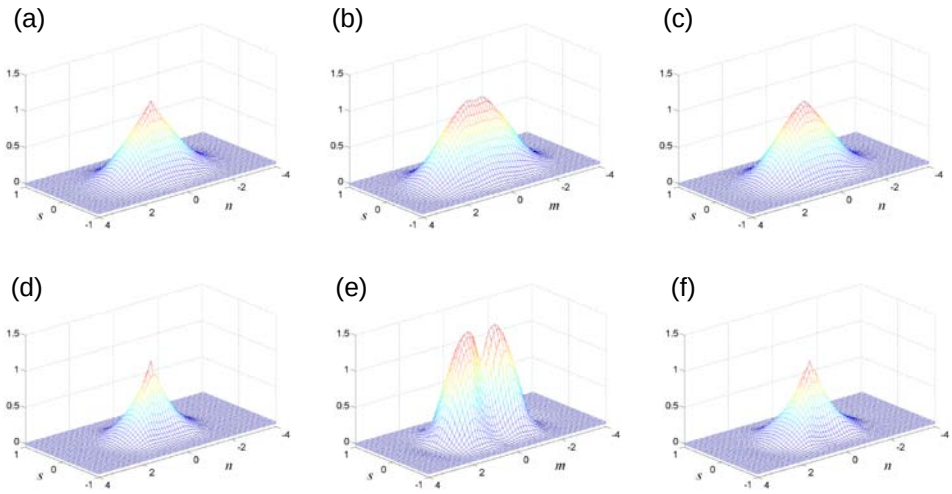

Fig. 4.1.5. 3-D optical transfer functions (a) of confocal microscope, $v_d = 0$; (b) $C(m, n = 0, s)$ of IPFMM, $v_d = 0$; (c) $C(m = 0, n, s)$ of IPFMM, $v_d = 0$; (d) of confocal microscope, $v_d = 4$; (e) $C(m, n = 0, s)$ of IPFMM, $v_d = 4$; (f) $C(m = 0, n, s)$ of IPFMM, $v_d = 4$.

v_d increases, the 3D OTF becomes narrower and the region over which the 3D OTF has appreciable value reduces gradually. This is understandable since the optical sectioning ability of the confocal microscope can be degraded with the utilization of a finite sized detector. In Fig. 4.1.5, compared with the confocal microscope, it is interesting to notice that there are double peaks in the *m* direction in IPFMM. Although the cut-off spatial frequencies remain the same as confocal microscopy, the magnitude of the 3D OTF is increased, which indicates that a stronger signal can be obtained. Therefore, the transverse resolution can be improved. This improvement in transverse

resolution is further discussed in the following section. The double peaks phenomenon results from the introduction of the phase modulator. The two illumination pupils, with and without phase modulator, do not overlap. Therefore, two peaks appear in the 3D OTF. With the convolution of the finite size detector, the ratio of the two peaks to the origin can be further enhanced.

Transverse resolution in confocal fluorescence imaging is determined by the transverse cutoff spatial frequency and transverse response of the 3D OTF. One of the methods for characterizing the transverse resolution is to consider the image of a shape and straight edge scanned in the focal plane.

We first consider a thick, straight and sharp fluorescent edge (i.e. the edge of a fluorescent sea) scanned in the focal plane. Since the IPSF for IPFMM is not central symmetrical, two important cases should be considered: the edge being oriented perpendicular (⊥) and parallel (//) to the *x* axis. The corresponding fluorescence strength of objects can be expressed as:

$$\begin{cases} o_{f\perp}(x,y,z) = \begin{cases} 1, & x \geq 0, \\ 0, & x < 0, \end{cases} \\ o_{f\parallel}(x,y,z) = \begin{cases} 1, & y \geq 0, \\ 0, & y < 0. \end{cases} \end{cases} \tag{4.1.9}$$

Because of the incoherent nature of image formation in the IPFMM, the image intensities of the edges can be expressed as:

$$\begin{cases} I(v_x) = I_{ip} \otimes_3 o_{f\perp} = \dfrac{1}{2} + \dfrac{1}{\pi}\displaystyle\int_0^{l_c} C(m, n=0, s=0)\frac{\sin(v_x m)}{m}dm, \\ I(v_y) = I_{ip} \otimes_3 o_{f\parallel} = \dfrac{1}{2} + \dfrac{1}{\pi}\displaystyle\int_0^{l_c} C(m=0, n, s=0)\frac{\sin(v_y n)}{n}dn. \end{cases} \tag{4.1.10}$$

The one-photon fluorescence images of the thick edge in IPFMM, compared with confocal microscopy (CM), for a point detector and a finite size detector with $v_d = 2.8$ are shown in Fig. 4.1.6. The value is normalized to unity by its value far from the edge. The intensity at the edge is one half of its value far from the edge, as is expected for incoherent imaging in confocal. It is seen that for a given size of pinhole, the images obtained in IPFMM are sharper than those in confocal, irrespective of the orientation of the edge. Besides, when the edge is oriented perpendicular to the *x* axis, the improvement becomes more significant. It is interesting to note that for IPFMM, the image of the thick edge oriented perpendicular to the *x* axis is even sharper as v_d increases; while for confocal microscope, the image of the thick edge becomes broader as v_d increases, indicating a degraded transverse resolution. The significance of this result is that IPFMM can obtain much higher sensitivity of edge detection than confocal in practical applications where a finite-size detector pinhole is always applied. This property is further shown in Fig. 4.1.7, where the gradient of the image at the edge ($(\partial I / \partial v_{x,y})_{v_{x,y}=0}$) is plotted as a function of v_d. It is noted that when the edge is orientated perpendicular to the *x* axis, the gradient for point detector is approximately 36.1% larger than that for confocal, whereas improvement reaches to 75.4% for a finite-sized detector pinhole with $v_d = 2.8$. It should be mentioned that negative value appears in the image intensity profile of the

edge for FMM cases, due to the modulation and demodulation procedures. However, if a small pinhole is applied, the negative value is negligible.

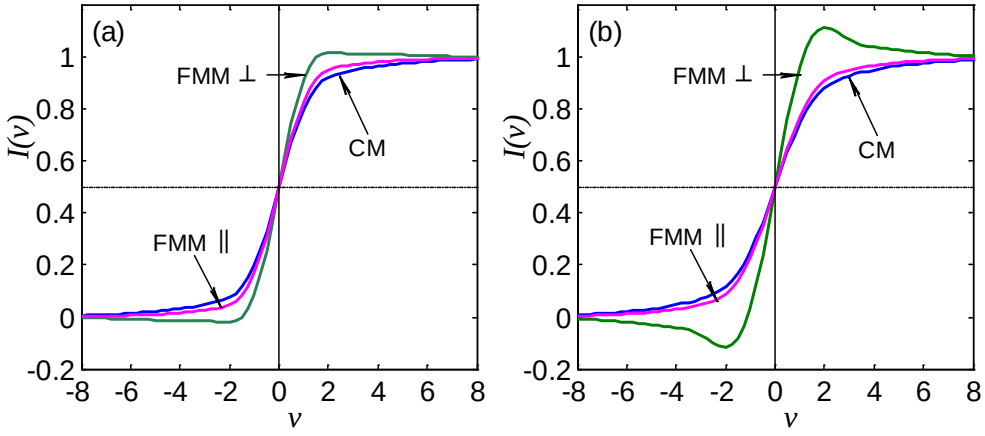

Fig. 4.1.6. The one-photon fluorescence images of the thick edge in IPFMM compared with confocal microscopy (CM) for (a) point detector; (b) detector pinhole radius $v_d = 2.8$.

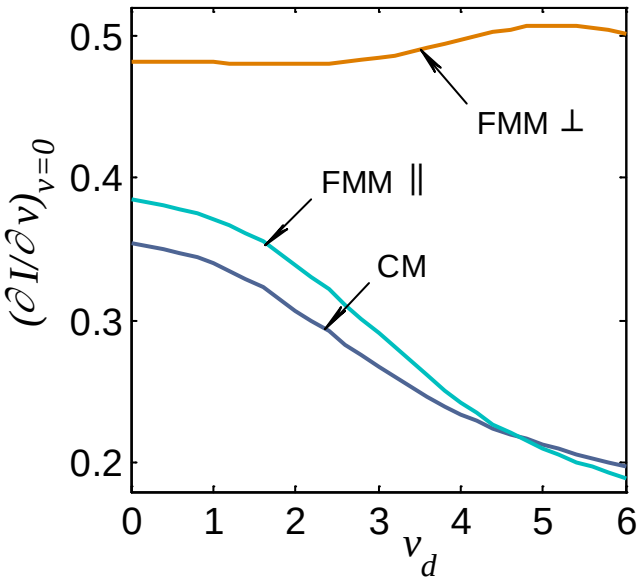

Fig. 4.1.7. Intensity gradient of the image $(\partial I / \partial v_{x,y})_{v_{x,y}=0}$ of the thick edge in IPFMM compared with confocal microscopy (CM).

The improvement in transverse resolution can be also found in the case of images for a thin, straight and sharp fluorescent edge scanned in the focal

plane. In this case, we also need to consider two extreme cases: the edge perpendicular and parallel to the *x* axis. The object functions thus are expressed as:

$$\begin{cases} o_{f\perp}(x,y,z)=\delta(z)\begin{cases}1, & x\geq 0,\\ 0, & x<0,\end{cases} \\ o_{f\parallel}(x,y,z)=\delta(z)\begin{cases}1, & y\geq 0,\\ 0, & y<0.\end{cases}\end{cases} \tag{4.1.11}$$

The corresponding image intensities of the edges in the focal plane can be derived as:

$$\begin{cases} I(v_x)=I_{ip}\otimes_3 o_{f\perp}=\dfrac{1}{2}+\dfrac{1}{\pi}\displaystyle\int_0^{l_c} C_2(m,n=0)\frac{\sin(v_x m)}{m}dm, \\ I(v_y)=I_{ip}\otimes_3 o_{f\parallel}=\dfrac{1}{2}+\dfrac{1}{\pi}\displaystyle\int_0^{l_c} C_2(m=0,n)\frac{\sin(v_y n)}{n}dn. \end{cases} \tag{4.1.12}$$

where $C_2(m,n)$ denotes the two-dimensional in-focus OTF of the IPFMM, given by the projection of the 3D OTF $C(m,n,s)$ in the focal plane.

Figure 4.1.8 displays the one-photon fluorescence images of the thin edge in IPFMM compared with confocal microscopy. For the edge oriented perpendicular to the *x* axis, the IPFMM method results in much sharper images compared with confocal, for both point and finite-sized detector pinhole cases. Besides, as the detector pinhole size increases, the image obtained in IPFMM becomes sharper (Fig. 4.1.9). For the edge parallel to the *x* axis, the intensity gradient at the edge of IPFMM for small detector pinhole size is slightly larger than that of confocal. However, as the detector pinhole size increases, the sharpness of the image in IPFMM becomes obviously

superior to that in confocal. It is noted that when the edge is oriented perpendicular to the x axis, the gradient for point detector is approximately 22.6% larger than that for confocal, whereas improvement reaches to 58.9% for a finite-sized detector pinhole with $v_d = 2.8$.

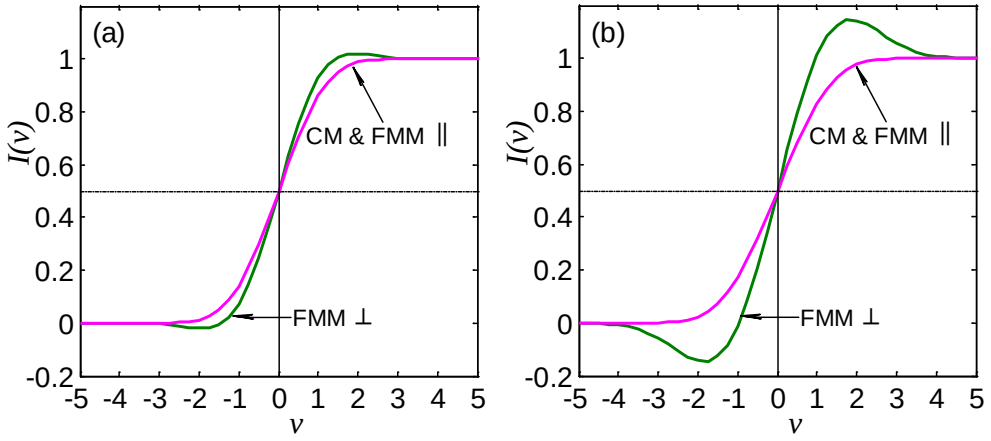

Fig. 4.1.8. The one-photon fluorescence images of the thin edge in IPFMM compared with confocal microscopy (CM) for (a) point detector; (b) detector pinhole radius $v_d = 2.8$.

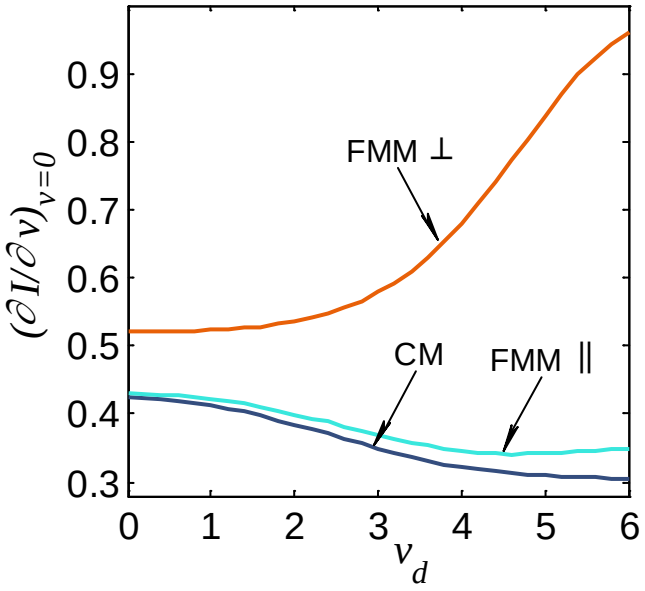

Fig. 4.1.9. Intensity gradient of the image $(\partial I / \partial v_{x,y})_{v_{x,y}=0}$ of the thick edge in IPFMM compared with confocal microscopy (CM).

We have shown that the improvements of the transverse resolution exist despite the orientation of the edge. Interestingly, as the detector pinhole size increases, the transverse resolution of IPFMM for the edge oriented perpendicular to x axis is dramatically improved compared with that of confocal, whose transverse resolution is gradually degraded. It seems that in order to obtain transverse resolution as high as possible, we should apply a detector pinhole as big as possible. However, as the size of the detector pinhole increases, the amount of unwanted scattered light is also increased. Thus, the signal level becomes practically important. In incoherent imaging, the signal level can be derived by considering the object to be a thin uniform fluorescent sheet in the focal plane [5]:

$$\eta(v_d) = \int_0^{s_c} C(m=0, n=0, s)ds, \tag{4.1.13}$$

where s_c is the axial cut-off spatial frequency.

Figure 4.1.10 illustrates the signal level η as a function of normalized detector radius v_d in IPFMM. It is seen that as the detector size increases, the signal level first increases then decreases, leading to a maximum at v_d around 2.8. The probable reason for this phenomenon is that as the detector size increases, the negative value of the IPSF of IPFMM becomes large enough to affect the image formation. Thus in practice, to obtain high transverse resolution with IPFMM, the normalized detector pinhole radius should not exceed 2.8. Besides, if the pinhole radius size is smaller than 2.8,

the axial resolution degradation can be negligible according to numerical experiments.

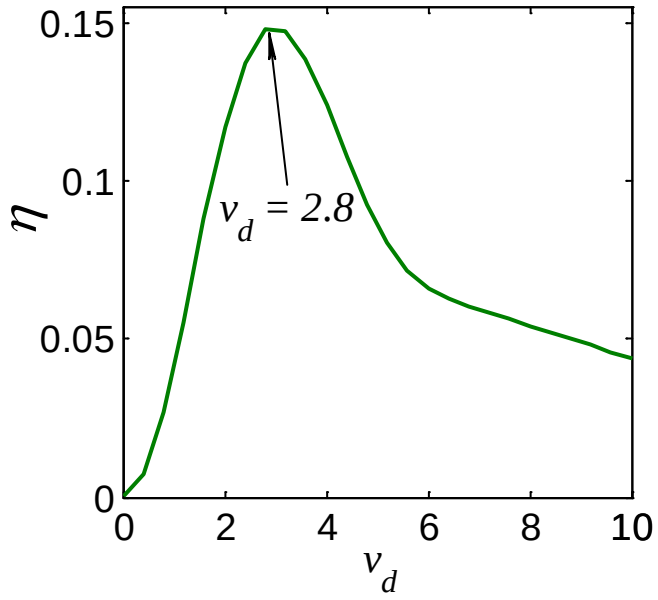

Fig. 4.1.10. Signal level η as a function of detector pinhole radius v_d in IPFMM.

In conclusion, we have theoretically analyzed the one-photon fluorescence images of straight edges in IPFMM. The simulations of the edge images are performed based on the 3D OTF of IPFMM. Numerical results show that given the value of normalized detector pinhole radius 2.8, the edge gradient can be increased up to 75.4% and 58.9% for thick edge and thin edge, respectively. Compared with confocal microscope, our low-cost IPFMM can not only reject background signal more effectively [104], but also obtain higher transverse resolution, especially when the edge is oriented perpendicular to the *x* axis. This development is particularly appealing for biological research and clinical diagnosis.

4. 2 Focal modulation microscopy with annular apertures

4.2.1 Introduction

In section 4.1, we investigated focal modulation microscopy with divided D-shaped apertures, which combines confocal fluorescence microscopy with the angular gating technique. The advantages of FMM over confocal microscopy have been demonstrated by a series of theoretical analyses and imaging experiments using a tissue phantom and chicken cartilage. Experimental results show that the imaging depth of FMM can be extended to around 600 μm [16]. In addition, the transverse resolution is also improved [103]. However, the prototype FMM system uses two non-overlapped D-shaped apertures (DFMM), which destroys the spatial resolution symmetry of the system.

In this section, we extend our previous work and propose an alternative geometry based on annular apertures to retain the symmetry of the system. We find that focal modulation microscopy with annular apertures (AFMM) can further enhance the background rejection compared with DFMM, and thus the penetration depth can be further extended. Numerical results also show that compared with confocal microscopy, AFMM can simultaneously increase both the axial and transverse resolutions. This is perhaps surprising, since as is well known confocal microscopy using an annular aperture with a small detector pinhole always results in an improvement in transverse resolution at the cost of

reduction of the optical sectioning strength [67]. But actually it has been shown previously that an annular pupil can give improved sectioning strength when used in conjunction with a finite sized pinhole [90]. Finally, the analysis of the signal level shows an optimal configuration of AFMM. In the following sections, we describe the behavior of AFMM based on scalar diffraction theory. The schematic diagram of AFMM is shown in Fig. 4.2.1.

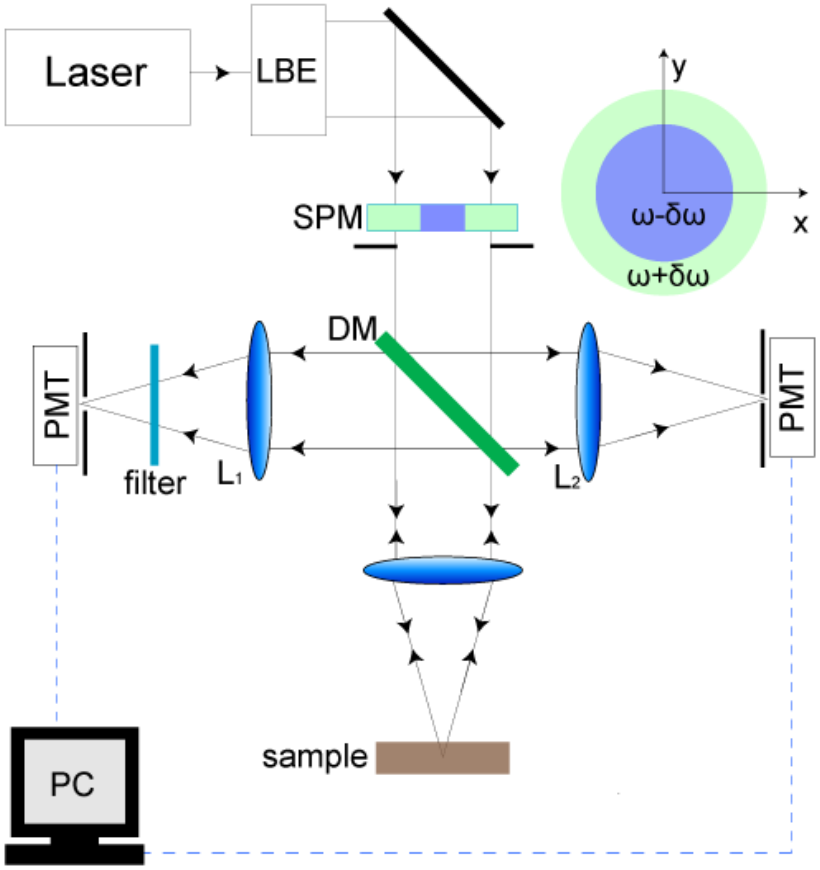

Figure 4.2.1. Schematic diagram of focal modulation microscopy with annular apertures.

4.2.2 Image of a point object

The 3D IPSF of AFMM is given by Eq. (4.1.4), where $h_{1A}(v,u)$ and $h_{1B}(v,u)$ are the 3D APSF of the annular and circular objective apertures, respectively, and $h_2(v,u)$ is the APSF of the collection lens. According to the scalar diffraction theory and paraxial approximation, these are defined by:

$$h_{1A,1B,2}(v,u) = \int_0^1 P_{1A,1B,2}(\rho) J_0(v\rho) \exp(-iu\rho/2) \rho d\rho, \qquad (4.2.1)$$

where P_{1A} and P_{1B} are the pupil functions of the annular objective aperture with inner and outer radii of εa and a ($0 < \varepsilon < 1$), and the circular objective aperture with radius of εa, respectively, and P_2 is the pupil function of the collection lens. These expressions also apply for other non-overlapping geometries for the pupils P_{1A} and P_{1B} with central symmetry. The image performance can be demonstrated by simulating the image of a test pattern such as a radial spoke pattern. Fig. 4.2.2 illustrates a comparison of the images of a sequence of fan blades which are arranged in a spiral away from the focal plane to a defocus plane at $u = 6.5$ with an interval of $\Delta u = 0.5$, for CM and AFMM, respectively, with various detector sizes. It can be noticed that for a point detector, the image intensity with AFMM degrades much faster in the optical axial direction than CM, indicating the better optical sectioning ability of AFMM. The imaging performance of AFMM with $\varepsilon = 0.9$ is slightly better than that of AFMM with equal area ($\varepsilon = \sqrt{2}/2$) in both axial and transverse resolutions. As the detector size increases, the images of both CM

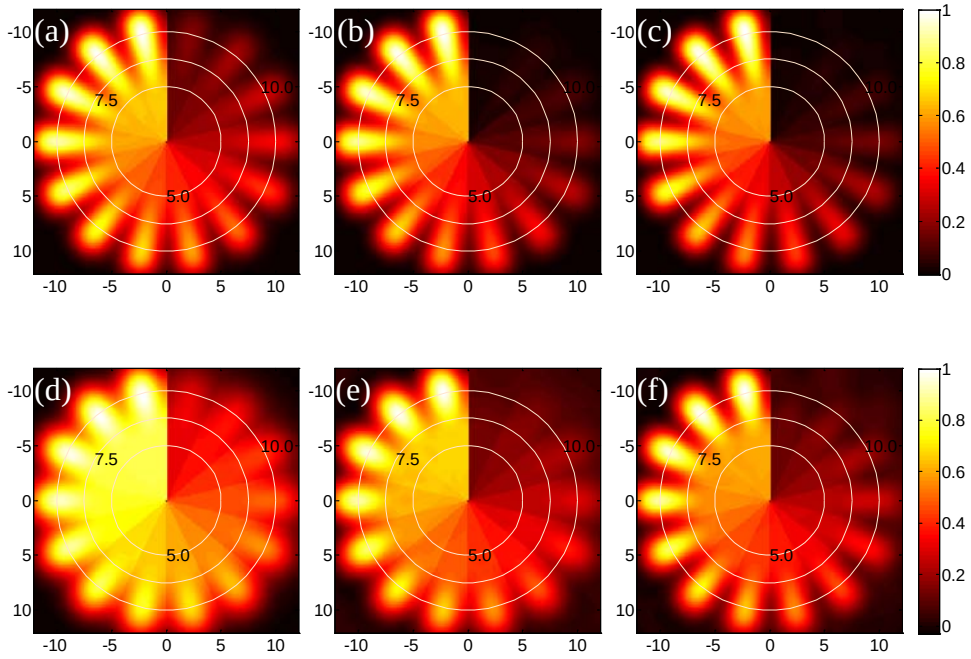

Figure 4.2.2. Images of a sequence of fan blades arranged in a spiral away from the focal plane to a defocus plane at $u = 6.5$ with an interval of $\Delta u = 0.5$ for (a) CM with a point detector; (b) AFMM with equal area $\varepsilon = \sqrt{2}/2$ with a point detector; (c) AFMM with $\varepsilon = 0.9$ with a point detector; (d) CM with $v_d = 4$; (e) AFMM with equal area $\varepsilon = \sqrt{2}/2$ with $v_d = 4$; (f) AFMM with $\varepsilon = 0.9$ with $v_d = 4$. The horizontal and vertical axes are in units of *v*.

and AFMM become blurred. In addition, the defocus intensity is relatively enhanced, indicating that the spatial resolution of both imaging systems is gradually degraded. However, the advantages of AFMM over CM become more obviously in both the strength of optical section and the transverse resolution. It is interesting to note that given the same detector radii, both the axial resolution and transverse resolution of AFMM can be further enhanced by increasing the inner radius (εa) of the annular objective aperture.

To further investigate the transverse resolution with AFMM, we compare the images of a radial spoke pattern at the focal plane for CM, DFMM and AFMM, respectively, for various values of the detector radii v_d in Fig. 4.2.3. It can be noticed that the transverse resolution of DFMM is asymmetric due to the asymmetric property of the two D-shaped illumination. In DFMM, improved transverse resolution can be obtained in the horizontal direction, however, it is gradually degraded when deviating from the horizontal direction to the vertical direction. In AFMM, the transverse resolution remains the same for all the directions because of the symmetric property of the annular and circular apertures. In fact, DFMM can improve the transverse resolution in one direction and when $v_d < 2.8$, its strength of optical sectioning can be maintained as similar to CM. Interesting, AFMM can not only improve the transverse resolution to the same level of DFMM, but also simultaneously increase the optical sectioning strength. As v_d increases, the advantages of AFMM over both CM and DFMM become more obvious in the spatial resolution, making AFMM quite promising for biological application.

The spatial resolution can be further investigated with the intensity point spread function (IPSF). Fig. 4.2.4 illustrates the three-dimensional intensity point spread function normalized to unity at $v = u = 0$, for confocal microscopy (CM), DFMM and AFMM with $\varepsilon = \sqrt{2}/2$, respectively, with a point detector. Compared with confocal microscopy, the size of the central

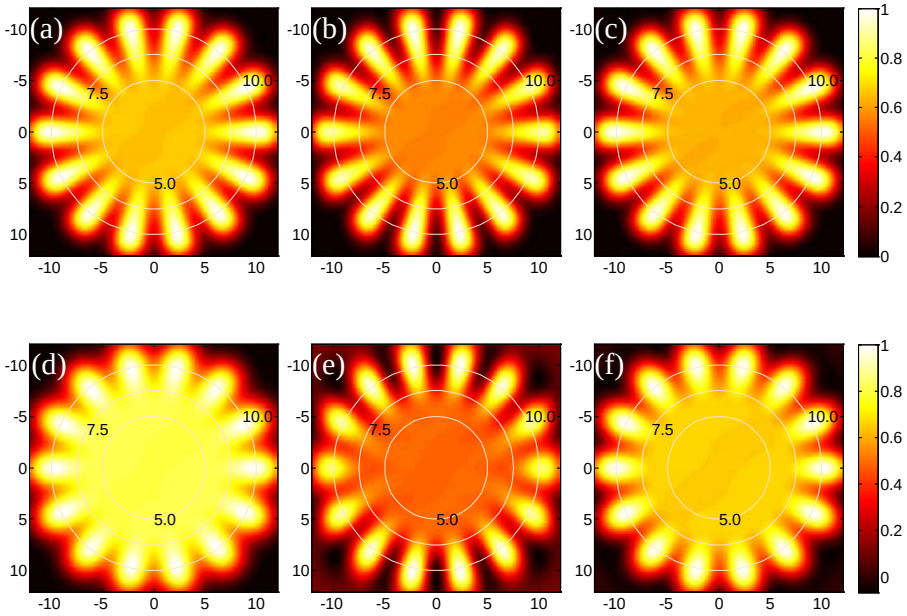

Figure 4.2.3. Images of a radial spoke at the focal plane for (a) CM with a point detector; (b) DFMM with a point detector; (c) AFMM with equal area $\varepsilon = \sqrt{2}/2$ with a point detector; (d) CM with $v_d = 4$; (e) DFMM with $v_d = 4$; (f) AFMM with equal area $\varepsilon = \sqrt{2}/2$ with $v_d = 4$. The horizontal and vertical axes are in units of *v*.

bright spot of the 3D IPSF of DFMM is smaller in the v_x direction, whereas remains the same in the v_y and axial directions, which means that DFMM can improve the transverse resolution in one direction. However, for the case of AFMM, the IPSF is narrower in the axial direction, whereas it remains the same as CM in the transverse direction, which means it can improve the axial resolution while maintaining the transverse resolution the same as the CM. Comparison of the cross sections of the IPSF for CM, DFMM and AFMM, along the v_x direction (solid lines) and axial direction (dash lines) are shown

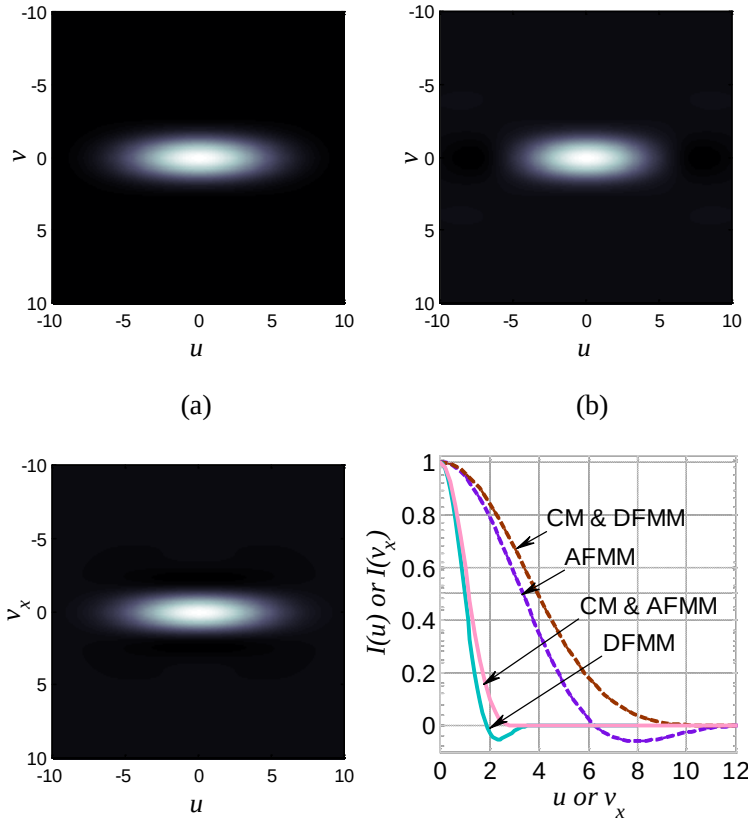

Figure 4.2.4. Intensity point spread functions with a point detector for (a) CM; (b) DFMM; (c) AFMM with equal area $\varepsilon = \sqrt{2}/2$. (d) Cross sections of the IPSF for CM, DFMM and AFMM with equal area $\varepsilon = \sqrt{2}/2$, in axial direction (dash lines) and in v_x direction (solid lines), respectively.

in Fig 4.2.4(d). The half width at half maximum (HWHM) of the 3D IPSF is improved up to 16.4% in the v_x direction by DFMM, and 17.8% in axial direction by AFMM. It should be pointed out that as the value of ε increases, the IPSF of AFMM will be further concentrated in both transverse and axial directions, leading to a further improvement in both transverse and axial resolution. Note that the IPSFs of both DFMM and AFMM exhibit

values that can be slightly negative, which is due to the modulation and demodulation process. However, when the detector radius $v_d < 3.8$, the relative negative value (compared to maximum) of AFMM is less than 10%.

4.2.3 Optical transfer function

The 3D optical transfer function (OTF) for AFMM is simply given by the 3D Fourier transform of IPSF, which can be expressed as:

$$C(l,s) = F_3\left[\left(h_{1A}(v,u)h_{1B}^*(v,u) + h_{1A}^*(v,u)h_{1B}(v,u)\right)\left(\left|h_2(v,u)\right|^2 \otimes_2 D(v)\right)\right], \tag{4.2.2}$$

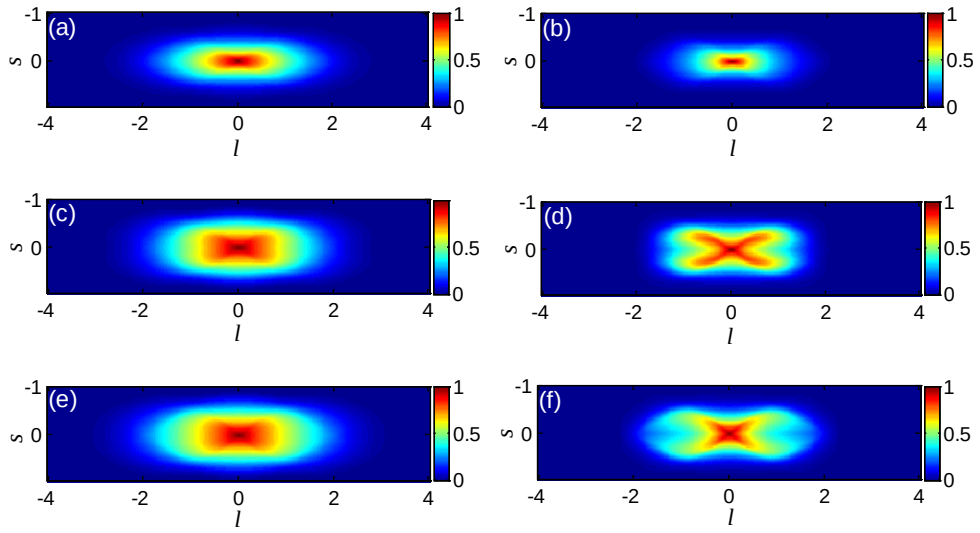

Figure 4.2.5. 3D Optical transfer functions for (a) CM with $v_d = 0$; (b) CM with $v_d = 4$; (c) AFMM with equal area $\varepsilon = \sqrt{2}/2$ with $v_d = 0$; (d) AFMM with equal area $\varepsilon = \sqrt{2}/2$ with $v_d = 4$; (e) AFMM with $\varepsilon = 0.9$ with $v_d = 0$; (d) AFMM with $\varepsilon = 0.9$ with $v_d = 4$.

Fig. 4.2.5 compares the 3D OTFs of CM with those of AFMM for various values of the detector radii v_d. The 3D OTFs are normalized to unity divided by $C(l=0, s=0)$. For a point detector, as expected, the normalized transverse and axial cut-off spatial frequencies of both CM and AFMM systems are 4 and 1, respectively. However, the high spatial frequency region in which the 3D OTF has appreciable values for AFMM is much broader than for CM. As v_d increases, the 3D OTF of AFMM becomes much broader than that of CM. This broadening of the 3D OTF results in a superior response at high spatial frequencies, due to more energy is distributed at higher spatial frequency in AFMM than in CM. Thus, an improved spatial resolution can be achieved by AFMM system. In addition, AFMM with $\varepsilon = 0.9$ shows a better performance than AFMM with equal area ($\varepsilon = \sqrt{2}/2$). For example, considering the in-focus OTF $C_2(l)$ which is given by the integration of the 3D OTF $C(l, s)$ with respect to the variable *s*, the value of $C_2(l)$ of AFMM with equal area increases by 10.6% over CM at frequency $l = 2$ for a point detector. However, the improvement increases to 43.1% with AFMM with $\varepsilon = 0.9$. For higher frequency such as $l = 3$, the improvement can be further enhanced to 100% with AFMM with $\varepsilon = 0.9$.

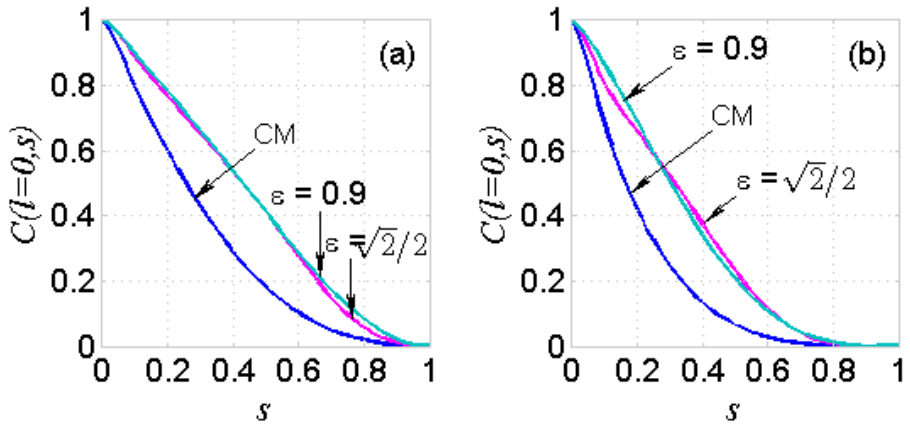

Figure 4.2.6. The cross section $C(l=0,s)$ of the 3D OTF for CM, AFMM with equal area $\varepsilon=\sqrt{2}/2$ and AFMM with $\varepsilon=0.9$ with (a) $v_d=0$; (b) $v_d=4$.

Fig. 4.2.6 shows the cross section $C(l=0,s)$ of the 3D OTF, whose one-dimensional inverse Fourier transform is directly proportional to the axial response of an infinitely thin fluorescent sheet, thus giving a measure of the strength of optical sectioning. Note that for a point detector, at high frequency such as s = 0.8, $C(l=0,0.8)$ of AFMM with equal area is enhanced four times compared with CM, while for AFMM with $\varepsilon=0.9$, the improvement reaches to 5.5 times. As v_d increases to 4, the improvements of $C(l=0,0.8)$ for AFMM with equal area and $\varepsilon=0.9$ increase to 4.5 times and 5 times, respectively, thus implying a larger improvement in the strength of optical sectioning.

4.2.4 Background rejection

Besides spatial resolution, penetration depth, which relates to the background rejection ability, is also of crucial importance in an imaging system. The integrated intensity can be used to describe the background from an infinitely thin autofluorescing sheet. The comparison of the integrated intensity of CM, DFMM and AFMM with equal area ($\varepsilon = \sqrt{2}/2$) is shown in Fig. 4.2.7 for various values of detector radii. It is well known that the integrated intensity decays as u^2 for CM with a point detector [12]. The decay rate increases to u^3 for DFMM and further increases for AFMM, indicating that more background can be eliminated, and thus higher penetration depth can be achieved. It can be noticed that a zero point of I_{int} appears along the optical axis, which results from the modulation and demodulation process, as well as the area match of the two objective apertures. For a finite-sized detector, the advantages of AFMM from the point of view of background rejection become more apparent (Fig 4.2.7b).

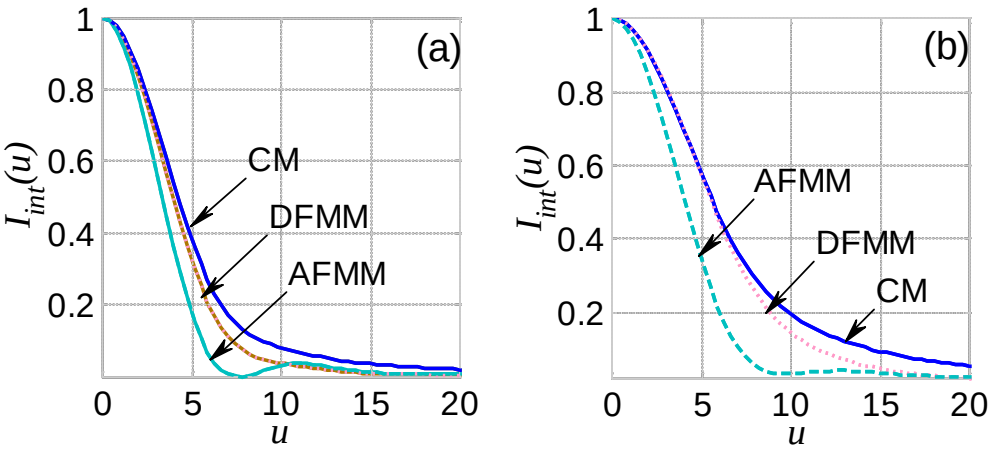

Figure 4.2.7. The integrated intensity for a confocal microscopy, DFMM and AFMM with equal area $\varepsilon = \sqrt{2}/2$ for: (a) $v_d = 0$: (b) $v_d = 4$.

For a thick object, the background of the different microscope geometries with a point detector is compared directly in Fig. 4.2.8, normalized to unity by the intensity at the focal point. It can be noticed that compared with CM, the background signal can be suppressed by either DFMM or AFMM. Interestingly, compared with DFMM, if AFMM with equal areas is used, the background rejection capability can be enhanced only when the normalized defocus distance $u > 6.7$. However, if AFMM with $\varepsilon = 0.9$ is used, the background rejection capability is improved for any thickness of the object, indicating that for AFMM as the value of ε increases, the background signal can be further reduced.

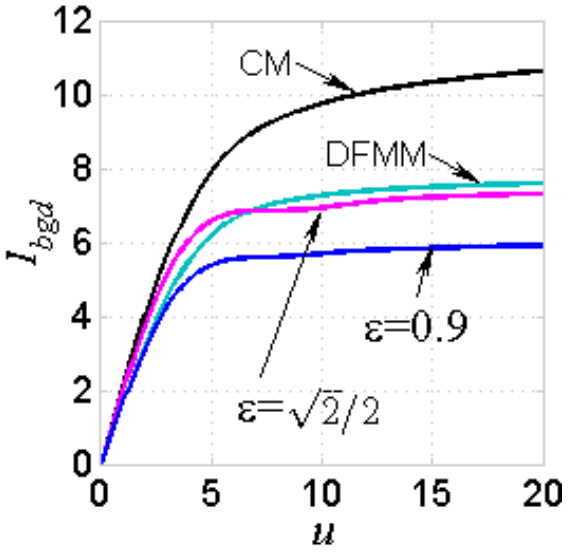

Figure 4.2.8. The background as a function of defocus distance for CM, DFMM, AFMM with equal area $\varepsilon = \sqrt{2}/2$ and AFMM with $\varepsilon = 0.9$, with a point detector.

Fig. 4.2.9 illustrates the signal level η, normalized to unity by the signal detected by CM with infinitely large detector, as a function of normalized detector radius v_d of AFMM with

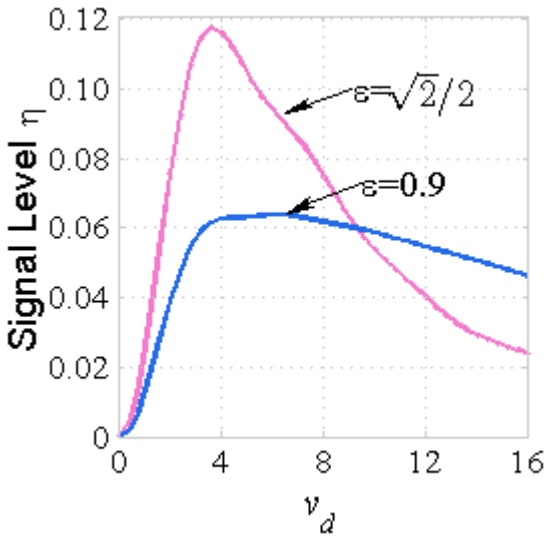

Figure 4.2.9. Signal level from a thin fluorescent sheet η of AFMM with equal area $\varepsilon = \sqrt{2}/2$ and with $\varepsilon = 0.9$ as a function of normalized detector radius v_d.

equal area and with $\varepsilon = 0.9$, respectively. Comparing with AFMM with $\varepsilon = 0.9$, AFMM with equal area has a much larger signal level due to the area match of the annular lens and the circular lens. Therefore, when considering the signal level performance, AFMM with equal area acts better than AFMM with $\varepsilon = 0.9$. For AFMM with equal area, it can be seen that as the detector size increases, the signal level first increases then decreases, leading to a maximum at v_d around 3.8. The probable reason for this phenomenon is that as the detector size increases, the negative value of the IPSF of AFMM

becomes large enough to affect the image formation. Thus in practice, to obtain high transverse resolution with AFMM with equal area, the normalized detector pinhole radius should not exceed 3.8 (1 Airy unit). Besides, if the pinhole radius size is smaller than 3.8, the axial resolution degradation can be negligible according to numerical experiments.

4.2.5 Discussion

In this section, we have proposed a method, named focal modulation microscopy with annular aperture (AFMM), to effectively reject background signal, meanwhile maintain the central symmetry of the transverse resolution. Numerical study shows that compared with confocal microscopy, AFMM can simultaneously improve the transverse resolution and the strength of optical sectioning. Besides, by adjusting the width of the annular objective aperture, AFMM can shift from the highest signal level (when $\varepsilon = \sqrt{2}/2$) to the best spatial resolution (when ε close to 1). The background rejection capability is also much improved, thus better penetration depth can be obtained.

Chapter 5 Conclusions and suggestions for further work

This study has explored tissue optics modeling in biological tissue and cells. The general functions of random non-spherical rough-surfaced particles with axially-symmetric properties were introduced. It was found that with a series of generation functions restricted by the “display window”, the medium can be characterized by a cluster of random non-spherical particles. An important feature of this generation function is that generally all kinds of shapes can be described completely with five parameters. This method can thus greatly reduce the complexity of the calculation and facilitate the process of tissue optics modeling in biological science.

This study also investigated the phase function, which describes the angular distribution of scattered intensity. It was found that the phase functions are insensitive to the dimension-to-length ratios D/L in most of the scattering regions for different kinds of rough cylinder. This agrees with claims that the phase function of a representative shape mixture of non-spherical particles is fairly insensitive to the elementary shapes used to form the mixture [53]. These findings are of crucial importance in terms of characterization of cylindrical particles in tissue optics modeling, since an average parameter can be used instead of considering various D/Ls for every cylindrical particle.

A random non-spherical model combined with the *T*-matrix method was proposed in this study, to model the tissue optics properties in biological science. The strong agreement between theoretical predictions with the non-spherical model and experimental data confirms our hypothesis that the particle's shape is the key contributor to tissue optics modeling. The simulation results exhibit slight differences with the experimental results in the forward scattering region and back scattering region. This may be attributed to the existence of multiple scattering. The phase function for surface-equivalent spheres showed larger discrepancy with experiments, especially in the side-scattering and backscattering regions. This suggests that the scattering properties of non-spherical particles can be significantly different from those of equivalent spheres. Therefore, the random non-spherical model has the power to simulate biological tissue better than the spherical model. This random non-spherical model can thus contribute to the accurate and efficient optical property description for biological science and medical diagnosis.

It is acknowledged that this study did only a preliminary analysis on modeling tissue optics properties with random non-spherical generation functions and the *T*-matrix method. The experimental data are limited to mouse skeletal tissue, mitochondria and rat embryo fibroblast cells. To extrapolate our conclusions to other kinds of tissue, additional laboratory experiments on particular tissue and cells and additional calculations are needed to examine the validity of this random non-spherical model. It is also

recommended that an extension to various biological tissue and cells with different refractive indexes be investigated, since the current computational results pertained to a specific refractive index of typical biological tissue.

It should be pointed out that this random non-spherical model used only a single scattering analysis based on the random non-spherical model. Therefore, for thick tissue where multiple scattering dominates, further work is needed to correlate the simulation to multiple scattering processes, which can be simplified with diffusion theory.

This study also analyzed, based on diffraction theory, the angular gating technique for increasing penetration depth in confocal microscopy of tissue. We investigated confocal systems with D-shaped illumination and detection apertures, a geometry that has been used by several groups, but which, until now, has not been investigated fully using diffraction theory. The three-dimensional coherent transfer function and three-dimensional optical transfer function were described for coherent (reflectance) and incoherent (fluorescence) confocal microscopy, respectively. The axial resolution and transverse resolution were also investigated. It was found that compared with conventional confocal microscopy, both the axial resolution and transverse resolution are degraded for a point detector. This was expected from the reduced size of the pupils. However, we found that the axial resolution can be improved when combined with a finite-size detector, and an optimum normalized width between the two pupils, d, can be derived for a given

finite-sized detector. This is of practical significance: for a given value of the detector radius, an improvement in the axial resolution can be obtained by altering the distance parameter to an optimum value of d_0. To suppress the out-of-focus central bright spot occurring in the confocal system, serrated divided apertures were proposed as a substitute for the D-shaped apertures. Diffraction analysis shows that the serrated apertures maintain the optical sectioning strength while attenuating the background coming from far from the focal plane. In addition, the signal to background ratio is also improved.

Focal modulation microscopy (FMM) is another technique to effectively reject multiply scattered photons in confocal fluorescence microscopy. The first diffraction analysis of the imaging properties of FMM was performed. The three dimensional (3D) intensity image of a point object was investigated. The illuminating pattern was observed to move relative to the focal point, which can be regarded as a soft scanning around the focal point as a function of time. This is different from conventional confocal microscopy, where the illumination pattern is fixed. This scanning ability can be attributed to the relative phase shift between the two beams with different modulated frequencies. This soft scanning property which is not restricted by the speed of the scanning instrument has the potential to overcome instrumental speed limitations and allow a super-fast scanning. Moreover, the conventional scanning instruments always suffer from inertia problems, while this soft scanning technique facilitates the provision of an inertia-free

continuous scanning scheme, which would improve the accuracy and efficiency of the scanning process greatly.

The 3D image intensity of a point object in FMM with a point detector was also theoretically investigated, for different recorded signals: the modulation signal, the in phase-signal, and confocal signal. It was found that the contour in the $v_x = 0$ plane behaves exactly the same for all three signals. This is understandable, because in the *y* direction of the incident pupil space there is no phase change in FMM. The simulation results also indicate that the image for the modulated signal in FMM is narrower in the transverse direction (*x* direction) than for the confocal microscope with D-shaped pupils, but broader than that for the confocal microscope with circular pupils. The in-phase signal, IPFMM, converged to a narrower transverse region than those for either confocal microscopy or the modulation signal in FMM. The half width at half maximum (HWHM) of the IPSF for IPFMM is more than four times narrower, compared with the confocal microscopy claimed by Sheppard [110]. This phenomenon suggests that using the in-phase signal of FMM, an improved spatial resolution can be obtained. This improvement is obtained only in one direction, but could be applied in two directions using two modulation frequencies, with image processing in Fourier space. The IPSF for IPFMM exhibited values that were slightly negative, and these negative values increased for larger pinhole sizes. However, when v_d was less than 2, the IPSF was similar to the point detector case. The resolution improvement of

IPFMM corresponds well with the technique of two-pupil synthesis [106], which is a general method for generating an optical transfer function to increase the relative strength of higher spatial frequencies. This high resolution performance should enable us to visualize a wide range of biological processes, such as molecular expression, cell trafficking, and cell-cell and cell-microenvironment interactions, in natural environment *in vivo*, providing information that cannot be obtained *in vitro* or *ex vivo*. Although the improvement occurs only from an improved response at higher spatial frequencies, rather than an increased spatial frequency bandwidth, we proposed the combination with saturated excitation, to attain true superresolution.

Various detector sizes were also investigated for the FMM system to examine the relationship between the imaging performance and detector size. The intensity point spread function was found to be degraded only slightly as the detector size was increased. This indicates that the increasing of detector size does not deterioate the imaging performance significantly, and that the spatial resolution can be maintained with a relatively large scale of detector size. The important feature of this property is that it allows us to enhance the detection intensity while retaining the spatial resolution with a relatively large detector size, since the larger detector enables a stronger detected signal. For very deep imaging in scattering tissue, this advantage becomes more apparent since significant background is generated at the out-of-focus planes.

The background rejection capability, for a weakly scattering medium, was quantified using the concept of the integrated intensity. The integrated intensity of IPFMM was observed to have a narrower main lobe in the region near the focal plane than that for confocal microscopy. The simulation results suggest that the background of IPFMM decays most quickly with distance from the focal plane, among all the microscopy technologies discussed. This property is of importance since it should help to reduce the cross-talk between in-focus image and out-of-focus images, thus contributing to high spatial resolution and increased imaging penetration depth.

Use of annular, rather than D-shaped, pupils was also investigated. This geometry can give improved axial resolution, or improved transverse resolution with a finite-sized pinhole, according to the relative dimensions. There are many other possibilities for the shapes of the pupils that could be explored.

The superior imaging penetration of FMM can be explained in terms of scattering in the following way. In confocal microscopy, some ballistic photons scattered from the vicinity of the focal plane can still be collected by the detector through the pinhole. However, In the FMM case, only the ballistic photons in the focal region can be detected due to their well-defined phase and polarization. Thus the spatial filtering effect using only a pinhole in confocal microscopy is not as effective as in FMM, where the spatial filtering effect is enhanced by the phase modulator. Moreover, detection of the in-phase signal

in FMM, instead of the modulation signal, gives better spatial resolution and deeper penetration depth, making it promising for *in vivo* imaging. In practice, the use of lock-in amplifier can further enhance the noise rejection by reducing noise components that do not coincide with the modulation frequency.

It is acknowledged that this study did only a preliminary analysis on imaging performance for focal modulation microscopy. It is assumed that a single scattering process dominates in the target tissue, and the extinction process is neglected. These assumptions require that all the ballistic light travels approximately the same optical path-length through the tissue to attain the depth *z*. However, ballistic light is not subject to Beer's Law and does not decay exponentially with increasing *z*. Besides, the more deeply an excitation beam is focused into a turbid medium, fewer ballistic photons arrive at the focal point, where multi-scattering light dominates the detected intensity. Further research is therefore needed to correlate the scattering decay and absorption to the imaging quality with focal modulation microscopy, and to take into account the multiple scattering, which will greatly affect the results in a thick biological tissue. To achieve this, diffusion approximation could be employed to reduce the calculation complexity (but the diffusion approximation is often not valid in the microscope imaging regime), and the Monte Carlo method can be used to simulate the multiple scattering processes with a large number of photons.

It should also be pointed out that our analysis of focal modulation microscopy is under the paraxial approximation. This approximation is largely true when the numerical aperture is less than 0.7. However, it loses its validity as the numerical aperture increases above 1. Therefore, for a system with large numerical aperture, vector diffraction theory should be considered. It is also recommended that the imaging performance of focal modulation microscopy with various polarization conditions should be established and described, which could be greatly different from the unpolarized case.

References

1. H. Zhang, K. Maslov, G. Stoica, and L. Wang, "Functional photoacoustic microscopy for high-resolution and noninvasive in vivo imaging," Nat. Biotechnol. **24**, 848-851 (2006).
2. M. J. Levene, D. A. Dombeck, K. A. Kasischeke, R. P. Molley, and W. W. Webb, "In vivo multiphoton microscopy of deep brain tissue," J. Neurophysiol. **91**, 1908-1912 (2004).
3. M. Yang, P. Jiang, and R. M. Hoffman, "Whole-body subcellular multicolor imaging of tumor-host interaction and drug response in real time," Cancer Res. **67**, 5195-5200 (2007).
4. C. J. R. Sheppard, and R. Kompfner, "Resonant scanning optical microscope," Appl. Opt. 17 **17**, 2879-2882 (1978).
5. M. Gu, *Principles of Three-Dimensional Imaging in Confocal Microscopes* (World Scientific, 1996).
6. X. Deng, and M. Gu, "Penetration depth of single-, two-, and three-photon fluorescence microscopic imaging through human cortex structures: Monte Carlo simulation," Appl. Opt. 42 **42**, 3321-3329 (2003).
7. C. J. R. Sheppard, and M. Gu, "Improvement of axial resolution in confocal microscopy using an annular pupil," Optics Comm. **84**, 7-13 (1991).
8. C. J. Koester, "A scanning mirror microscope with optical sectioning characteristics: Applications in ophthalmology," Appl. Opt. **19**, 1749-1757 (1980).
9. C. J. Koester, "Comparison of optical sectioning methods: The scanning slit confocal microscope," in *Handbook of Confocal Microscopy*, J. Pawley, ed. (Plenum Press, New York, 1990).
10. P. J. Dwyer, and C. A. DiMarzio, "Confocal reflectance theta line scanning microscope for imaging human skin in vivo," Opt. Lett. **31**, 942-944 (2006).
11. P. J. Dwyer, C. A. DiMarzio, and M. Rajadhyaksha, "Confocal theta line-scanning microscope for imaging human tissues," Appl. Opt. **46**, 1843-1851 (2007).
12. C. J. R. Sheppard, W. Gong, and K. Si, "The divided aperture technique for microscopy through scattering media," Opt Express **16**, 17031–17038 (2008).
13. K. Si, W. Gong, and C. J. R. Sheppard, "Three-dimensional coherent transfer function for a confocal microscope with two D-shaped pupils," Appl. Opt. **48**, 810-817 (2009).
14. L. K. Wong, M. J. Mandella, G. S. Kino, and T. D. Wang, "Improved rejection of multiply scattered photons in confocal microscopy using dual-axes architecture," Opt. Lett. **32**, 1674-1676 (2007).
15. J. T. C. Liu, M. J. Mandella, S. Friedland, R. Soetikno, J. H. Crawford, C. H. Contag, G. S. Kino, and T. D. Wang, "Dual-axes confocal reflectance microscope for distinguishing colonic neoplasia," J. Biomed. Opt. **11**, 054019

(2006).
16. N. G. Chen, C. H. Wong, and C. J. R. Sheppard, "Focal modulation microscopy," Opt. Express **16**, 18764-18769 (2008).
17. M. S. Patterson, "Noninvasive measurements of tissue optical properties," Comments Mol. Cell. Biophys. A **8**, 387-417 (1995).
18. G. Tearney, M. E. Brezinsky, B. E. Bouma, S. A. Boppart, C. Pitris, J. F. Southern, and J. G. Fujimoto, "In vivo endoscopic optical biopsy with optical coherence tomography," Science **276**, 2037-2039 (1997).
19. B. Beauvoit, T. Kitai, and B. Chance, "Contribution of the mitochondrial compartment to the optical properties of the rat liver: a theoretical and practical approach," Biophys. J. **67**, 2501-2510 (1994).
20. J. M. Schmitt, and G. Kumar, "Turbulent nature of refractive-index variations in biological tissue," Opt. Lett. **21**, 1310-1312 (1996).
21. A. Dunn, and R. Richards-Kortum, "Three-dimensional computation of light scattering from cells
" IEEE J. Sel. Top. Quantum Electron. **2**, 989-906 (1996).
22. S. Chandrasekhar, *Radiative Transfer* (Oxford University Press, London, 1950).
23. A. Ishimaru, *Wave Propagation and Scattering in Random Media* (Academic Press, New York, 1978).
24. R. K. Wang, "Modelling optical properties of soft tissue by fractal distribution of scatters," J. Mod. Opt **47**, 103-120 (2000).
25. J. M. Schmitt, and G. Kumar, "Optical scattering properties of soft tissue: a discrete particle model," Appl Optics **37**, 2788-2797 (1998).
26. G. Mie, "Beiträge zur optik trüber medien, speziell kolloidaler metallösungen," Ann. Phys. **25**, 377-445 (1908).
27. L. Lorenz, "Lysbevaegelsen i og uden for en haf plane lysbolger belyst kulge," Vidensk. Selk, Skr. **6**, 1-62 (1890).
28. J. W. Nicholson, "Diffraction of short waves by a rigid sphere," Philos. Mag **11**, 193-205 (1906).
29. J. R. Mourant, J. P. Freyer, A. H. Hielscher, A. A. Eick, D. Shen, and T. M. Johnson, "Mechanism of light scattering from biological cells relevant to noninvasive optical-tissue diagnostics," Appl. Opt. **37**, 3586-3593 (1998).
30. P. C. Waterman, "Symmetry, unitarity, and geometry in electromagnetic scattering," Phys. Rev. D **3**, 825-839 (1971).
31. M. I. Mishchenko, L. D. Travis, and A. A. Lacis, *Scattering, Absorption and Emission of light by small particles* (Cambridge, 2002).
32. M. I. Mishchenko, "Multiple scattering, radiative transfer, and weak localization in discrete random media: unified microphysical approach," Rev. Geophys. **48**, doi: 10.1029/2007RG000230 (2008).
33. H. Siedentopf, and R. Zsigmondy, "Uber Sichtbarmachung und Grössenbestimmung ultramikroskopischer Teilchen, mit besonderer Anwendung auf Goldrubingläser," Annalen der Physik **10**, 1-39 (1903).
34. H. Goldman, "Spaltlampenphotographie und -photometrie,"

Ophthalmologica **98**, 257-270 (1940).
35. D. M. Maurice, "Cellular membrane activity in the corneal endothelium of the intact eye," Experientia **15**, 1094-1095 (1968).
36. E. H. K. Stelzer, S. Lindek, S. Albrecht, R. Pick, G. Ritter, N. J. Salmon, and R. Stricker, "A new tool for the observation of embryos and other large specimens - confocal theta-fluorescence microscopy," J. Microsc. **179**, 1-10 (1995).
37. T. D. Wang, M. J. Mandella, C. H. Contag, and G. S. Kino, "Dual-axis confocal microscope for highresolution in vivo imaging," Opt. Lett. **28**, 414-416 (2003).
38. K. Moriya, "Observation of Micro-Defects in as-Grown and Heat-Treated Si Crystals by Infrared-Laser Scattering Tomography," J Cryst Growth **94**, 182-196 (1989).
39. G. Kissinger, J. Vanhellemont, C. Claeys, and H. Richter, "Observation of stacking faults and prismatic punching systems in silicon by light scattering tomography," J Cryst Growth **158**, 191-196 (1996).
40. A. H. Voie, D. H. Burns, and F. A. Spelman, "Orthogonal-plane fluorescence optical sectioning: threedimensional imaging of macroscopic biological specimens," J. Microsc. **170**, 229-236 (1993).
41. J. Huisken, J. Swoger, F. D. Bene, J. Wittbrodt, and E. H. K. Stelzer, "Optical sectioning deep inside live embryos by selective plane illumination microscopy," Science **305**, 1007-1009 (2004).
42. P. Török, C. J. R. Sheppard, and Z. Laczik, "Dark-field and differential phase contrast imaging modes in confocal microscopy using a half-aperture stop," Optik **103**, 101-106 (1996).
43. P. Török, C. J. R. Sheppard, and Z. Laczik, "The effect of half-stop lateral misalignment on imaging of dark-field and stereoscopic confocal microscopes," Appl. Opt. **35**, 6732-6739 (1996).
44. P. Theer, M. T. Hasan, and W. Denk, "Two-photon imaging to a depth of 1000 μm in living brains by use of a Ti:Al2O3 regenerative amplifier," Opt. Lett. **28**, 1022-1024 (2003).
45. J. G. Fujimoto, "Optical coherence tomography for ultrahigh resolution in vivo imaging," Nat. Biotechnol. **21**, 1361-1367 (2003).
46. K. Fujita, M. Kobayashi, S. Kawano, M. Yamanaka, and S. Kawata, "High-resolution confocal microscopy by saturated excitation of fluorescence," Phys. Rev. Lett. **99**, 228105 (2007).
47. M. Yamanaka, S. Kawano, K. Fujita, N. I. Smith, and S. Kawata, "Beyond the diffraction-limit biological imaging by saturated excitation microscopy," J. Biomed. Opt. **13**, 050507 (2008).
48. R. K. Wang, "Modelling optical properties of soft tissue by fractal distribution of scatters," J. Mod. Opt. **47**, 103-120 (2000).
49. M. I. Moscoso, J. B. Keller, and G. Papanicolaou, "Depolarization and blurring of optical images by biological tissue," J. Opt.Soc. Am. A **18**, 948-960 (2001).

50. M. Xu, and R. R. Alfano, "Fractal mechanisms of light scattering in biological tissue and cells," Opt. Lett. **30**, 3051-3053 (2005).
51. M. I. Mishchenko, G. Videen, V. A. Babenko, N. G. Khlebtsov, and Th. Wriedt, "T-matrix theory of electromagnetic scattering by particles and its applications: a comprehensive reference database," J. Quant. Spectrosc. Radiat. Transfer **88**, 357-406 (2004).
52. H. C. V. d. Hulst, *Multiple Light Scattering* (Academic, 1980).
53. M. I. Mishchenko, L. D. Travis, R. A. Kahn, and R. A. West, "Modeling phase functions for dustlike tropospheric aerosols using a shape mixture of randomly oriented polydisperse spheroids," J. Geophys. Res. **102**, 16,831-816,847 (1997).
54. L. Tsang, J. A. Kong, and R. T. Shin, *Theory of Microwave Remote Sensing* (Wiley, 1985).
55. V. D. Tuan, *Biomedical Photonics Handbook* (CRC, 2003).
56. G. I. Ruban, S. M. Kosmacheva, N. V. Goncharova, D. V. Bockstaele, and V. A. Loiko, "Investigation of morphometric parameters for granulocytes and lymphocytes as applied to a solution of direct and inverse light-scattering roblems," J. Biomed. Opt. **12**, 044017 (2007).
57. M. Kerker, *The Scattering of Light and other electromagnetic Radiation* (Academic, 1969).
58. J. M. Schmitt, and G. Kumar, "Optical scattering properties of soft tissue: a discrete particle model," Appl. Opt. **37**, 2788-2797 (1998).
59. Y. S. Fawzy, M. Petek, M. Tercelj, and H. S. Zeng, "In vivo assessment and evaluation of lung tissue morphologic and physiological changes from non-contact endoscopic reflectance spectroscopy for improving lung cancer detection," J. Biomed. Opt. **11**, 044003 (2006).
60. C. J. R. Sheppard, "A fractal model of light scattering in biological tissue and cells," Opt. Lett. **32**, 142-144 (2007).
61. A. Alberts, D. Bray, J. Lewis, M. Raff, K. Roberts, and J. D. Watson, *Molecular Biology of the Cell* (Garland, New York, 1994).
62. G. E. Palade, *An electron microscope study of the mitochondrial structure* (University Park Press, Baltimore, 1972).
63. W. Gong, K. Si, and C. J. R. Sheppard, "Modeling phase functions in biological tissue," Opt. Lett. **33**, 1599-1601 (2008).
64. J. Lenoble, and C. Brogniez, "A comparative review of radiation aerosol models," Beitr. Phys. Atoms. **57**, 1-20 (1984).
65. A. Macke, "Scattering of light by polyhedral ice crystals," Appl. Opt. **32**, 2780-2788 (1993).
66. K. L. K. Muinonen, J. Peltoniemi, and W. M. Irvine, "Light scattering by randomly oriented crystals," Appl. Opt. **28**, 3051-3060 (1989).
67. C. J. R. Sheppard, M. Gu, and X. Q. Mao, "Three-dimensional coherent transfer function in a reflection-mode confocal scanning microscope," Optics Comm. **81**, 281-284 (1991).
68. C. J. R. Sheppard, and K. G. Larkin, "Effect of numerical aperture on

interference fringe spacing," Appl. Opt. **34**, 4731-4734 (1995).
69. C. J. R. Sheppard, and X. Q. Mao, "Three dimensional imaging in a microscope," J. Opt. Soc. Am. A **6**, 1260-1269 (1989).
70. L. Giniunas, R. Juskaitis, and S. V. Shatalin, "Scanning fiber-optic microscope," Electron. Lett. **27**, 724-726 (1991).
71. M. Gu, C. J. R. Sheppard, and X. Gan, "Image formation in a fiber-optical confocal scanning microscope," J. Opt. Soc. Am. A **8**, 1755-1761 (1991).
72. M. Gu, and C. J. R. Sheppard, "Signal level of the fibre optical confocal scanning microscope," J. Mod. Opt. **38**, 1621-1630 (1991).
73. S. Kimura, and T. Wilson, "Confocal scanning optical microscope using single-mode fiber for signal detection," Appl. Opt. **30**, 2143-2150 (1991).
74. T. Dabbs, and M. Glass, "Single-mode fibers used as confocal microscope pinholes," Appl. Opt. **31**, 705-706 (1992).
75. P. Delaney, and M. Harris, "Fiberoptics in confocal microscopy," in *Handbook of biological confocal microscopy, 2nd ed.*, J. Pawley, ed. (Plenum, New York, 1995), pp. 515-523.
76. M. Gu, and C. J. R. Sheppard, "Three-dimensional coherent transfer function in reflection-mode confocal microscopy using annular lenses," J. Mod. Opt. **39**, 783-793 (1992).
77. M. Gu, and C. J. R. Sheppard, "Three-dimensional optical transfer function in the fibre-optical confocal fluorescent microscope using annular lenses," J. Opt. Soc. Am. A **9**, 1991-1999 (1992).
78. M. Gu, and C. J. R. Sheppard, "Signal level of the fibre optical confocal scanning microscope," Journal of Modern Optics **38**, 1621-1630 (1991).
79. M. Born, and E. Wolf, *Principles of Optics* (Pergamon, Oxford, 1959).
80. R. N. Bracewell, *The Fourier Transform and its Applications* (McGraw-Hill, New York, 1965).
81. C. J. R. Sheppard, and T. Wilson, "Depth of field in the scanning microscope," Opt. Lett. **3**, 115-117 (1978).
82. C. J. R. Sheppard, and M. D. Sharma, "Integrated intensity, and imaging through scattering media," J. mod. Opt. **48**, 1517-1525 (2001).
83. X. S. Gan, and C. J. R. Sheppard, "Detectability: A new criterion for evaluation of the confocal microscope," Scanning **15**, 187-192 (1993).
84. C. J. R. Sheppard, X. Gan, M. Gu, and M. Roy, "Noise in confocal microscopes," in *The Handbook of Biological Confocal Microscopy, 2nd ed.*, J. Pawley, ed. (Plenum Press, New York, 1995), pp. 363-370.
85. M. Gu, C. J. R. Sheppard, and H. Zhou, "Optimization of axial resolution in confocal imaging using annular pupils," Optik **93**, 87-90 (1993).
86. W. Gong, K. Si, and C. J. R. Sheppard, "Optimization of axial resolution in confocal microscope with D-shaped apertures," Appl. Opt. **48**, 3998-4002 (2009).
87. W. Gong, K. Si, and C. J. R. Sheppard, "Improvements in confocal microscopy imaging using serrated divided apertures," Opt. Commun. **282**, 3846-3849 (2009).

88. P. M. Delaney, M. R. Harris, and R. G. King, "Fiber-optic laser scanning confocal microscope suitable for fluorescence imaging," Appl. Opt. **33**, 573-577 (1994).
89. R. Kiesslich, J. Burg, M. Vieth, J. Gnaendiger, M. Enders, P. Delaney, A. Polglase, W. McLaren, D. Janell, S. Thomas, B. Nafe, P. R. Galle, and M. F. Neurath, "Confocal laser endoscopy for diagnosing intraepithelial neoplasias and colorectal cancer in vivo," Gastroenterology **127**, 706-713 (2004).
90. M. Gu, and C. J. R. Sheppard, "Three-dimensional imaging in confocal fluorescent microscopy with annular lenses," J. Mod. Opt. **38**, 2247-2263 (1991).
91. S. Hell, and E. H. K. Stelzer, "Properties of a 4Pi confocal fluorescence microscope," J. Opt. Soc. Am. A **9**, 2159-2166 (1992).
92. T. Wilson, "Optical sectioning in confocal fluorescent microscopes," J. Microsc. **154**, 143-156 (1989).
93. M. Gu, T. Tannous, and C. J. R. Sheppard, "Improved axial resolution in confocal fluorescence microscopy using annular pupils," Opt. Commun. **110**, 533-539 (1994).
94. M. Gu, and C. J. R. Sheppard, "Comparison of three-dimensional imaging properties between two-photon and single-photon fluorescence microscopy," J. Microsc. **177**, 128-137 (1995).
95. N. George, and G. M. Morris, "Diffraction by serrated apertures," J. Opt. Soc. Am. **70**, 6-17 (1980).
96. M. M. Beal, and N. George, "Features in the optical transform of a serrated aperture or disk," J. Opt. Soc. Am. A **6**, 1815-1826 (1989).
97. Y. Kim, H. Grebel, and D. L. Jaggard, "Diffraction by fractally serrated apertures," J. Opt. Soc. Am. A **8**, 20-26 (1991).
98. M. Gu, and X. S. Gan, "Fresnel diffraction by circular and serrated apertures illuminated with an ultrashort pulsed-laser beam," J. Opt. Soc. Am. A **13**, 771-778 (1996).
99. T. Wilson, and C. J. R. Sheppard, *Theory and Practice of Scanning Optical Microscopy* (Academic, London, 1984).
100. I. Pavlova, M. Williams, A. El-Naggar, R. Richards-Kortum, and A. Gillenwater, "Understanding the Biological Basis of Autofluorescence Imaging for Oral Cancer Detection: High-Resolution Fluorescence Microscopy in Viable tissue," Clin. Cancer Res. **14**, 2396-2404 (2008).
101. C. Zeng, S. Vangveravong, J. Xu, K. C. Chang, R. S. Hotchkiss, K. T. Wheeler, D. Shen, Z. Zhuang, H. F. Kung, and R. H. Mach, "Subcellular Localization of Sigma-2 Receptors in Breast Cancer Cells Using Two-Photon and Confocal Microscopy," Cancer Res. **67**, 6708-6716 (2007).
102. W. Gong, K. Si, and C. J. R. Sheppard, "Improved spatial resolution in fluorescence focal modulation microscopy," Opt. Lett. **34**, 3508-3510 (2009).
103. K. Si, W. Gong, and C. J. R. Sheppard, "Edge enhancement for in-phase focal modulation microscope," App. Opt. **48**, 6290-6295 (2009).

104. W. Gong, K. Si, N. Chen, and C. J. R. Sheppard, "Focal modulation microscopy with annular apertures: A numerical study," J. Biophoton. **DOI**, 10.1002/jbio.200900110 (2009).
105. S. P. Chong, C. H. Wong, C. J. R. Sheppard, and N. Chen, "Focal modulation microscopy: a theoretical study," Opt. Lett. **35**, 1804-1806 (2010).
106. T. C. Poon, "Method of two-dimensional bipolar incoherent image processing by acousto-optic two pupil synthesis," Opt. Lett. **10**, 197-199 (1985).
107. E. Rittweger, D. Wildanger, and S. W. Hell, "Far-field fluorescence nanoscopy of diamond color centers by ground state depletion," EPL **86**, 14001 (2009).
108. M. G. L. Gustafsson, "Nonlinear Structured-Illumination Microscopy: Wide-Field Fluorescence Imaging with Theoretically Unlimited Resolution," PNAS **102**, 13081-13086 (2005).
109. C. J. R. Sheppard, "Edge-setting criterion in confocal microscopy," Appl. Opt. **31**, 4575-4577 (1992).
110. C. J. R. Sheppard, and T. Wilson, "Image formation in confocal scanning microscopes," Optik **55**, 331-342 (1980).